Jorge Cebola Borbinha

Bachelor of Science

Organ Dose Estimates in Thorax CT: Voxel Phantom Organ Matching With Individual Patient Anatomy

Dissertation submitted in partial fulfillment
of the requirements for the degree of

Master of Science in
Biomedical Engineering

Supervisor: Salvatore Di Maria, PhD, C^{2}TN - IST

Co-supervisors: Pedro Vaz, PhD, C^{2}TN - IST

Ana Paula Madeira, MsC., Radiographer, HSJ - CHLC

FACULDADE DE
CIÊNCIAS E TECNOLOGIA
UNIVERSIDADE NOVA DE LISBOA

September, 2017

Organ Dose Estimates in Thorax CT:
Voxel Phantom Organ Matching With
Individual Patient Anatomy

This document was created using the (pdf)LaTeX processor, based in the "novathesis" template[1], developed at the Dep. Informática of FCT-NOVA [2].
[1] https://github.com/joaomlourenco/novathesis [2] http://www.di.fct.unl.pt

Aos meus avôs,
António Borbinha e Crispim Cebola

Acknowledgements

First of all, a great vote of appreciation goes to my thesis supervisor, Salvatore di Maria. I thank him for the patience, support and thoughtfulness he provided both on a professional and personal level, making the adventure shown in this document possible and worthwhile.

My sincere thankfulness goes to my co-supervisors, Paula Madeira and Pedro Vaz, for their dedication and availability, which made this project possible.

I would like to express my gratitude to FCT-UNL for all the knowledge and experience given, which allowed me to grow both on a professional and personal level, and for the beautiful campus, to which I fell in love at first sight. I would also like to thank C^2TN and HSJ, whose collaboration allowed me to undertake my master's thesis on a subject I love.

To all people whom I shared my workspace with, I am thankful for all the assistance and companionship provided. I thank Rita Monteiro for providing me with company and good advice during the better part of my thesis. A special mention goes to my sincere friend, Débora António, who accompanied me from the very beginning of our course of Biomedical Engineering until now, the very end.

To my father, Manuel, and my mother, Clementina, I would like to say that, if I was able to climb up the ladder, it is because I stood on your shoulders. I express my deepest gratitude to you for providing me every tool I need to have a great future. My heartfelt thankfulness goes to my grandfather, Crispim Cebola, for being the amazing person he is and for his farm's vegetables that gave me the strength needed to finish this thesis.

A great vote of appreciation goes to my dear friend, Bruno Catita, for the strength and motivation he inspires in me. My gratitude to my friend João Calisto, for all the moments, adventures and laughs we shared. I also thank my friend, Filipe Lacerda, who I have known for more time than I can remember. Thank you for the journey of a lifetime, may it go on for many years.

Lastly, my sincere thankfulness to John Ronald Reuel Tolkien, for the countless stories and infinite wisdom he shared, but mainly for teaching me that "all that is gold does not glitter".

"All that is gold does not glitter,
Not all those who wander are lost;
The old that is strong does not wither,
Deep roots are not reached by the frost."
J. R. R. Tolkien

Abstract

Given the continuous usage and spread of computed tomography (CT), the potential harmful effects and the radiation dose to the patient have become high interest topics among the scientific community.

The main objective of this investigation was to modify existing three-dimensional (3D) voxel phantom models to resemble real patients as much as possible, trying to progress the concept of a more personalized patient dosimetry. This work focused essentially in one of the biggest and most radiosensitive organs in the thorax, the lungs. Additionally, the variations of organ doses when a standard phantom is used instead were studied.

During the course of this work a FORTRAN-based program was developed, which is able to semi-automatically modify the volumetric information of organs of interest in a standard voxel phantom (Female ICRP Adult Reference). The voxel resolution was also altered so the phantom's diameters match the patient's ones. Monte Carlo (MC) PENELOPE simulation code was used to mimic CT scan conditions and, therefore, generate 2D projections, used for visual organ matching with clinical patient CT images, and access organ dose in both phantoms (ICRP standard and ICRP modified).

The main results reported that matching the voxel phantom's size and lungs provides organ dose values significantly different from the ones measured in the ICRP reference phantom. Voxel models matched to patients' size and overall anatomy allow increased accuracy in organ dose estimation, which, as reported by this study, can suffer from up to 20% underestimation and 40% overestimation.

This study demonstrates that voxel phantoms developed using single patient data provide a better and more precise organ dose assessment by MC methods than a standard phantom. The presented methodology should be of interest for dose optimization studies and quick enough for routine clinical use.

Keywords: Computed Tomography, Voxel Phantom, Monte Carlo Methods, Organ Dose, FORTRAN (Computer Programming Language)

Resumo

Dado o contínuo uso e expansão da tomografia computorizada (TC), os potenciais efeitos nocivos para a saúde e a dose radiativa para o paciente tornaram-se tópicos de elevado interesse para a comunidade científica. O principal objectivo desta investigação foi modificar fantomas de *voxel* para que se assemelhem a pacientes reais o mais possível, tentando assim desenvolver o conceito de dosimetria específica ao paciente. Este trabalho focou-se essencialmente num dos maiores e mais radiosensíveis órgãos do tórax, os pulmões. Adicionalmente, foram estudadas as variações de dose nos órgãos quando o fantoma de referência e o fantoma adaptado são utilizados.

Ao longo deste trabalho um programa foi desenvolvido em FORTRAN, capaz de modificar semi-automaticamente a informação volumétrica de órgãos de interesse num fantoma de *voxel* (Adulto Feminino de Referência do ICRP). A resolução dos *voxels* foi modificada para que os diâmetros dos fantomas correspondam aos do paciente. O código Monte Carlo (MC) PENELOPE foi utilizado para replicar as condições de um equipamento de TC, de forma a obter projeções em 2D e valores de dose em ambos os fantomas (ICRP referência e ICRP modificado).

Os resultados mostraram que a adaptação do tamanho e dos pulmões de fantomas de *voxel* providencia valores de dose nos órgãos bastante diferentes dos medidos no fantoma de referência. Fantomas de *voxel* com tamanho e pulmões adaptados permitem maior precisão na obtenção de valores de dose nos órgãos, que podem ser subestimados e sobrestimados até 20% e 40%, respetivamente.

A presente dissertação demonstra que a utilização de fantomas de *voxel* adaptados aos dados de pacientes individuais providencia, através de métodos MC, valores de dose nos órgãos mais precisos do que um fantoma de referência. A metodologia apresentada deve ser útil para estudos de otimização de dose, assim como rápida o suficiente para aplicações clínicas de rotina.

Palavras-chave: Tomografia Computorizada, Fantoma de Voxel, Métodos Monte Carlo, Dose nos Órgãos, FORTRAN (Linguagem de Programação)

Contents

List of Figures **xix**

List of Tables **xxi**

Acronyms **xxiii**

1 Introduction **1**
- 1.1 Motivation . . . 1
- 1.2 Objectives . . . 6
- 1.3 Thesis Outline . . . 6

2 Theoretical Fundaments **9**
- 2.1 Interaction of Radiation with Matter . . . 9
- 2.2 Fundaments of Computed Tomography . . . 10
- 2.3 The Radiation Protection International System . . . 12
- 2.4 Fundaments of Dosimetry . . . 13
  - 2.4.1 Radiometric Quantities . . . 13
  - 2.4.2 Dosimetric Quantities . . . 14
  - 2.4.3 Dosimetric Quantities in CT . . . 15

3 Dose Estimates in the Patient **19**
- 3.1 Dose Estimates using Physical Phantoms . . . 20
- 3.2 Dose Estimates using Computational Phantoms . . . 21
  - 3.2.1 Stylized Phantoms . . . 22
  - 3.2.2 Voxel Phantoms . . . 22
  - 3.2.3 BREP Phantoms . . . 24
- 3.3 Patient and Organ Dose Estimates Using MC Methods and Computational Phantoms . . . 24

4 Materials and Methods **29**
- 4.1 CTDI Measurements . . . 29
  - 4.1.1 CT Equipment . . . 30
  - 4.1.2 Ionization Chamber . . . 30
  - 4.1.3 PMMA Phantom . . . 30

4.1.4 Measurement Procedure 30
4.1.5 Results Procedure 32
4.2 The Male and Female ICRP Reference Phantoms 33
4.3 The FORTRAN Programming Language 34
4.4 Visualization and Simulation Files Program 34
4.5 Organ Scaling Program 35
4.6 Patient/Phantom Matching Procedure 39
4.6.1 Description of the Patient CT Images 39
4.6.2 Matching the Phantom Size 40
4.6.3 Matching the Lungs Dimension 40

5 The Monte Carlo Method **43**
5.1 MC Fundaments 43
5.2 PENELOPE 44
5.3 PenEasy 45
5.4 Implementation of CTDI Measurements 47
5.4.1 Geometry and Source Definition 47
5.4.2 Materials Definition 48
5.4.3 Spectrum Definition 48
5.5 Implementation of Scaled Phantoms MC Simulations 49
5.5.1 Geometry, Source and Materials Definition 49
5.5.2 Dose vs Voxel Volume Simulations 50
5.5.3 Scaled Lungs Phantom Simulations 51

6 Results and Discussion **53**
6.1 MC Model Validation 53
6.2 Dose vs Voxel Volume Results 55
6.3 Results from Patient/Phantom Matching Procedure 58
6.3.1 AF Size Measurement 58
6.3.2 Patient and Phantom Size Measurement 58
6.3.3 Results from Matching the Patient Size 60
6.3.4 Results from Matching the Lungs Size 62
6.3.5 Visual Comparison of Patient and Phantom Images 64

7 Conclusions and Future Work **69**

References **73**

A Lists of Materials and Organs Used in Voxel Phantom Simulations **79**

B Tally and 36-Point Interpolation Results from MC Model Validation **81**

C Lung Size Values Before and After Patient/Phantom Matching Procedure **85**

I Tutorial for the ReadPhantom Program **89**

List of Figures

1.1 Trends in the annual frequency of diagnostic x-ray examinations in function of health care level. . . . 2
1.2 Number of CT scans performed per 100 000 inhabitants in several European countries in 2009 and in 2014. . . . 3
1.3 There are several proposed models to explain the dose-response curve between radiation exposure and carcinogenic risk. . . . 4

2.1 Alan MacLeod Cormack and Godfrey Newbold Hounsfield are the co-creators of Computed Tomography. . . . 10
2.2 Set of four figures illustrating the concept of Computed Tomography Dose Index (CTDI). . . . 16

3.1 Depiction of the three computational phantom generations. . . . 21
3.2 Comparison of a stylized adult phantom and the VIP-Man phantom. . . . 23
3.3 Whole body models with Computed Tomography (CT) data appended at the top and bottom of the scanned volume with data from computational phantoms used in the study performed by Kalender et al. . . . 27

4.1 The polymethylmethacrylate (PMMA) phantom used in this work. . . . 31
4.2 The General Electric Company (GE) CT equipment used when performing the measurements. . . . 31
4.3 Representation of the action ReDimLungs takes when scaling a x-array. . . . 38
4.4 Workflow diagram of the patient/phantom matching procedure. . . . 42

5.1 Representation of a cross section of the phantom passing trough the x=0 plane for the situation of the chamber at the center of the phantom. . . . 47
5.2 Graph of the x-ray spectrum used in the MC simulations. . . . 49

6.1 Graph for TRENDXY. . . . 56
6.2 **a)** Graph for TRENDX. **b)** Graph for TRENDY. . . . 57
6.3 Visualization, using the Gnuplot tool, of Adult Female (AF)'s slice 238. . . . 58
6.4 Voxel resolution in x and y (on the left y axis) and voxel volume (on the right y axis) for every considered patient. . . . 61

6.5 Variation of organ dose in relation to the AF phantom for all resolution phantoms. 62
6.6 Variation of organ dose in relation to the AF phantom for the patient phantoms. 63
6.7 **a)** Image of the AF phantom obtained via the tally pixelated imaging detector. **b)** CT image topogram for Patient 1. **c)** Image of AF1 obtained via the tally pixelated imaging detector. 65
6.8 **a)** CT image topogram for Patient 2. **b)** Image of AF2 obtained via the tally pixelated imaging detector. 66
6.9 **a)** CT image topogram for Patient 3. **b)** Image of AF3 obtained via the tally pixelated imaging detector. 66
6.10 **a)** CT image topogram for Patient 4. **b)** Image of AF4 obtained via the tally pixelated imaging detector. 66
6.11 **a)** CT image topogram for Patient 5. **b)** Image of AF5 obtained via the tally pixelated imaging detector. 67
6.12 **a)** CT image topogram for Patient 6. **b)** Image of AF6 obtained via the tally pixelated imaging detector. 67

B.1 Example of graph of 36-interpolation of the tally values, for the Ionization Chamber (IC) at 0º position. 83

List of Tables

2.1 Recommended tissue weighing factors for various organs and tissues. 15

4.1 Main characteristics of the International Commission on Radiation Protection (ICRP) male and female reference phantoms. 34

5.1 Material list present at the PENELOPE section of the PenEasy input file. . . . 48

6.1 Dose, $CTDI_{100}$ and $CTDI_W$ values measured for the ionization chamber inserted in each orifice of the PMMA phantom. 54

6.2 Dose, respective uncertainty and CTDI_{100} and CTDI_W simulated values, as well as the relative difference between measured and simulated values, for every ionization chamber location. 54

6.3 L and AP diameters measured in the patients' CT images and in the simulated images of the resolution phantoms and relative difference between them. . . 60

A.1 List of the organs present in the organ list of the AF phantom. 79

A.2 List of the materials defined in the PENELOPE section of the PenEasy input file. 80

B.1 Tally and interpolation results for the IC in-air position. 81

B.2 Tally and interpolation results for the IC at center position. 82

B.3 Tally and interpolation results for the IC at 0º position. 82

B.4 Tally and interpolation results for the IC at 90º position. 82

C.1 Left lung size in x, y and z measured in the patients' CT images and in the patient phantoms and relative difference between them. 86

C.2 Right lung size in x, y and z measured in the patients' CT images and the patient phantoms and relative difference between them. 87

Acronyms

2D	Two-Dimensional.
3D	Three-Dimensional.
AAPM	American Association of Physicists in Medicine.
AF	Adult Female.
ALARA	As Low As Reasonably Achievable.
AP	Anterior-Posterior Diameter.
ASCII	American Standard Code for Information Interchange.
BREP	Boundary Representation.
BSS	Basic Safety Standards.
CAD	Computer Aided Diagnosis.
CF	Conversion Factor.
CSG	Constructive Solid Geometry.
CT	Computed Tomography.
CTDI	Computed Tomography Dose Index.
$CTDI_{vol}$	Volume Computed Tomography Dose Index.

$CTDI_W$	Weighted Computed Tomography Dose Index.
DLP	Dose-Length Product.
EMI	Electric and Musical Industries.
EURATOM	European Atomic Energy Community.
FDA	Food and Drug Administration.
FOV	Field of View.
GE	General Electric Company.
HNBR	High Natural Background Radiation.
HSJ-CHLC	*Hospital São José – Centro Hospitalar Lisboa Central*.
IAEA	International Atomic Energy Agency.
IC	Ionization Chamber.
ICRP	International Commission on Radiation Protection.
ICRU	International Commission on Radiation Units and Measurements.
ID	Identification Number.
IEC	International Electrotechnical Commission.
Kerma	Kinetic Energy Released to Matter.
L	Lateral Diameter.
LDR	Low Dose Radiation.
LNT	Linear Non-threshold.

MC	Monte Carlo.
MF	Magnification Factor.
MRI	Magnetic Resonance Imaging.
MSAD	Multiple Slice Dose Average.
MSCT	Multi-slice Computed Tomography.
ORNL	Oak Ridge National Laboratory.
PET	Positron-Emission Tomography.
PMMA	polymethylmethacrylate.
POSDE	Patient and Organ Specific Dose Estimate.
SI	International System of Units.
SSDE	Size-Specific Dose Estimate.
UF	University of Florida.
UNSCEAR	United Nations Scientific Committee on the Effects of Ionizing Radiation.
VOIs	Volumes of Interest.

CHAPTER 1

INTRODUCTION

1.1 Motivation

The application of engineering techniques to a wide variety of fields in the clinical realm has allowed tremendous scientific and technological advances in diagnosis and treatment of various pathologies. CT is a highly informative medical imaging method that allows for better and more efficient patient diagnosis. This is possible through the use of ionizing radiation to visualize internal anatomical structures with minimal intrusion [1].

Over the last 20 years, a high level of constant innovation by the CT equipment manufacturers allowed faster and easier image acquisition, better diagnostic capabilities and the introduction of new techniques. These factors encouraged high frequency usage of the technique, as well as the consequent increase in population exposure to ionizing radiation [1], [2].

The increased radiation exposure, parallel to the scientific and technological advent felt in the last decades, fomented the development of various techniques, which intended to provide better quality diagnostic and risk evaluation in medical imaging. One of such techniques is Computer Aided Diagnosis (CAD). The concept of CAD means using the computer output as a 'second opinion', equally accounting for the roles of physicians and computers, thus complementing their performances [3], [4]. Several observer performance studies have verified CAD's value by concluding that physicians' and radiologists' diagnostic accuracy improved significantly when using computed output in their interpretations of radiographs [5], [3]. Through computational solutions, CAD aims to improve the quality and productivity of the image interpretation performed by physicians and radiologists, by raising diagnostic accuracy and reducing image reading time, respectively [5]. Since the compromise patient dose/image quality is a fundamental principle in

the field of diagnostic radiology, more accurate dose calculation methodologies improve imaging department professionals' information regarding patient and organ dose. Consequently, physicians and radiologists will be able to make more informed decisions on the scan's performance, imaging protocol and even whether to perform the exam or not.

According to United Nations Scientific Committee on the Effects of Ionizing Radiation (UNSCEAR) data, there are approximately 3.6 billion diagnostic radiology X-ray examinations undertaken annually in the world. Additionally, approximately two thirds of these exams are performed on the 24% of the population living in health care level I countries (Figure 1.1). About 11% of CT examinations are performed in a pediatric population [1].

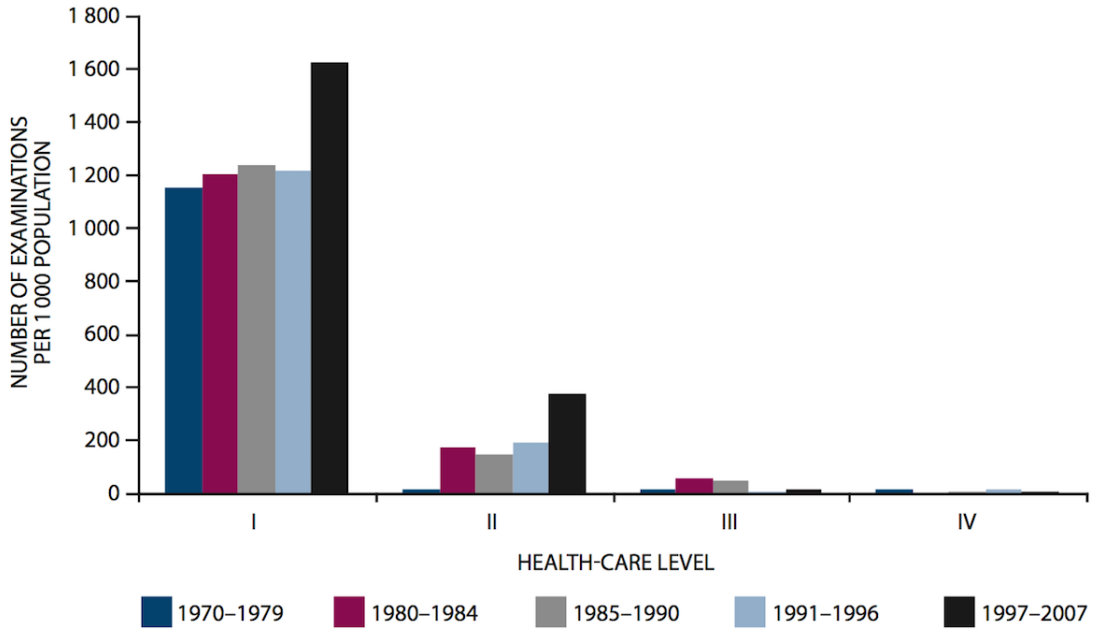

Figure 1.1: Trends in the annual frequency of diagnostic x-ray examinations in function of health care level [1].

In the United States, the number of CT scans increased from about 3 million in the 1980s to 67 million in 2006 [6], [7]. According to Eurostat, between 2009 and 2014, both the number of CT scanners and exams relative to population size increased in almost all the European countries, as illustrated in Figure 1.2. Portugal is the seventh European country with more CT scans relative to population size, with more than 15 000 CT scans per 100 000 inhabitants performed in 2014 [8]. Only in 2014, over one and a half million CT exams were performed in Portugal, corresponding to more than five times the number of Magnetic Resonance and Positron-Emission Tomography (PET) scans done in the same timeline. In addition, 228 CT scanners were counted in Portugal in 2014 [8].

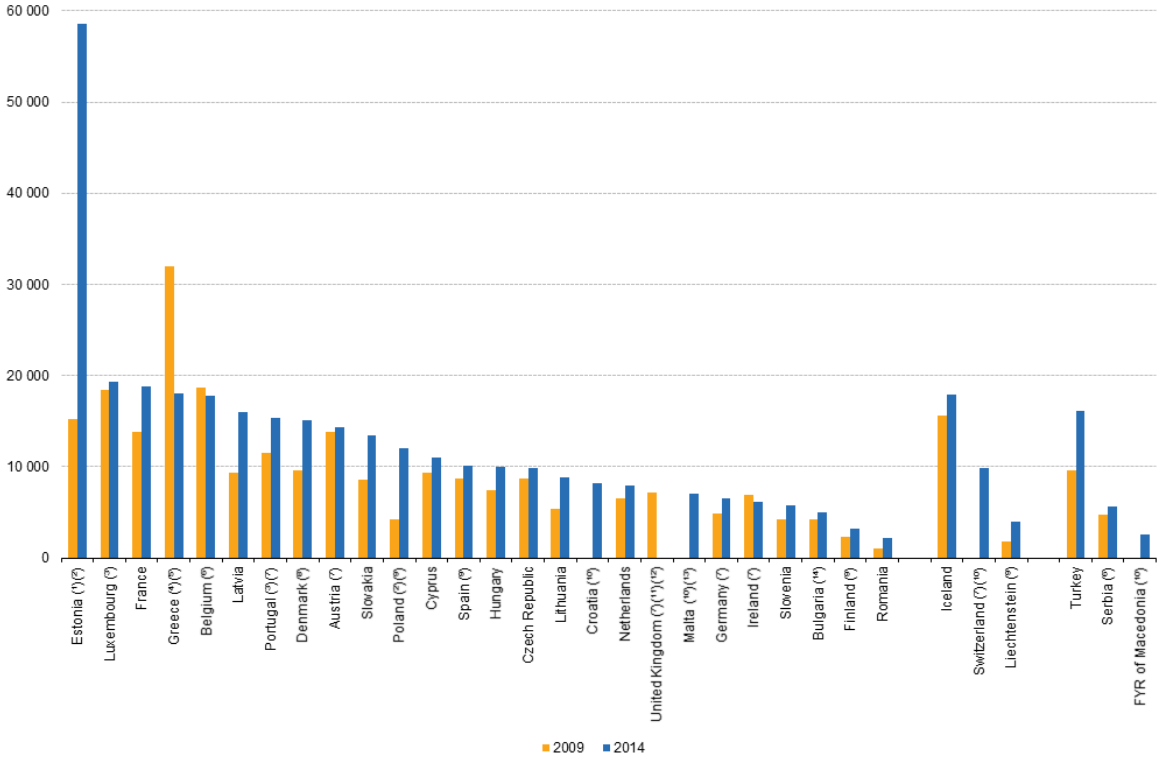

Figure 1.2: Number of CT scans performed per 100 000 inhabitants in several European countries in 2009 and in 2014. Adapted from [8].

Despite CT's high quality of disease diagnosis, examinations are generally associated with significantly higher doses of ionizing radiation than conventional radiology. Therefore, CT has become the main source of ionizing radiation used in the medical diagnosis field. Though it only represents 5-10% of imaging procedures, as much as 40-70% of the collective dose associated with medical examinations is attributed to CT [1], [2].

Whether there is a cumulative damaging effect or carcinogenic risk after repeated CT examinations, as well as its underlying biological basis, have become quite controversial subjects in the scientific community. The Fukushima Nuclear Power Station leak in 2011 raised the question of whether human health might be damaged by environmental high-level radiation. This has caused widespread concern and revitalized the debate of the beneficial and injurious effects of Low Dose Radiation (LDR) [2].

The damaging effects of LDR are mainly supported by the Linear Non-threshold (LNT) hypothesis (Figure 1.3). This hypothesis defends the linear relationship between cancer risk and radiation dose, i.e., any dose of radiation can lead to cancer. The ICRP established that a radiation dose of 10 mSv would result in a $\frac{1}{1000}$ to $\frac{1}{2000}$ cancer incidence [2]. Though the radiation doses from CT are classified as LDR, repeated scans may lead to cumulative dose values. For example, a mean responsive dose for all organs of 12mSv may imply a cumulative dose greater than 100 mSv upon 10 times of CT usage [9]. Another

investigation by Bernier et al. compiled three studies accessing carcinogenic risk related to CT examinations on children and young adults. Two studies performed in Australia and the United Kingdom perceived an excess risk of cancer and leukemia associated with CT exposure in childhood [10], [11], [12]. An increased risk, though non-significant, was also the result of a smaller Taiwanese study performed by Huang et al. [10], [13]. The existence of radiation hypersensitivity, suffered by 5-10% of individuals, also supports this side of the argument [14].

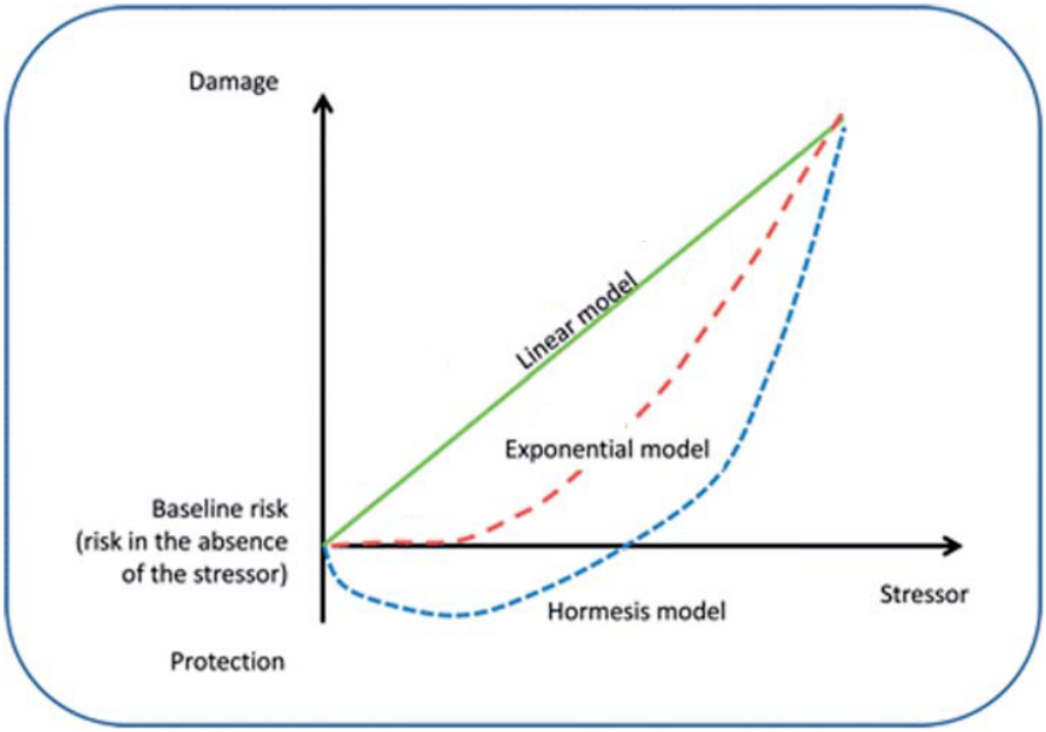

Figure 1.3: There are several proposed models to explain the dose-response curve between radiation exposure and carcinogenic risk. The LNT hypothesis states that the cancer risk is directly proportional to the dose level of ionizing radiation. In the case of the exponential model, the risk of cancer increases exponentially with the dose level of ionizing radiation. The hormesis model defends that LDR actually possesses protective effects, though higher doses are damaging to human health. Adapted from [2].

On the other side, the observation of hormesis (Figure 1.3) and adaptive response supports the beneficial effects of LDR. The concept of hormesis is based on some positive effects of LDR, such as enhanced immunity or increased lymphocyte transformation rate. Adaptive response refers to a protective mechanism, stating that a previous exposure to LDR may attenuate the damage caused by following high dose radiation. An investigation was carried out by Liu et al. among the High Natural Background Radiation (HNBR) population in China. Conclusions stated that lymphocyte percentage and transformation rates were higher in the group exposed to HNBR than in the control group. Additionally, a 36-year follow up study observed a reduction on the frequency of cancer in the exposed group [2]. In another investigation, the interventional cardiologists who were most likely

to come into contact with radiation in hospital were considered (with median exposure of 4mSv/year). The authors found that LDR may enhance the antioxidant defence system and increase apoptosis susceptibility (to remove damaged cells efficiently) after 2Gy of irradiation [15].

Nowadays Computed Tomography examinations suffer from five main problems, which are listed as follows.

1. The first issue is the high frequency usage of CT scans. Brenner et al. state more than one third of CT scans are either unnecessary or could easily be replaced by other imaging techniques, such as magnetic resonance imaging [16].

2. The patients' exposure to ionizing radiation is now higher than ever before. Radiation and cumulative doses in the patient have increased greatly, mainly due to the technological advancements of Multi-slice Computed Tomography (MSCT) and helical CT [17].

3. Proper attention to radiation sensitive groups is also very important, since children are about four times more sensitive to radiation than adults [18].

4. Given that different organs in the human body suffer from different radiosensitivities, CT radiation may vary significantly according to different parameters and scanning areas. Dose assessment in radiosensitive organs, such as the thyroid, is of uttermost importance [2].

5. The last issue refers to poor understanding of carcinogenic risks by both patients and professionals. A study, performed in the Emergency Department of an American academic medical center, revealed that only 7% of patients reported having been informed on benefits and risks before performing a CT scan. Additionally, 47% of radiologists and 9% of imaging department physicians did not believe CT would increase cancer risk [19].

Dose in CT is a subject that has received appropriate attention since CT's introduction in the diagnostic realm in the 1970s. Efforts addressed both scanner characteristics and patient dose aspects. As the investigation on dose metrics evolved, the CTDI was defined. This parameter, measured in PMMA cylindrical phantoms, is largely used and acknowledged worldwide [20].

In the 1990s, the growing computational power allowed for the dissemination of Monte Carlo (MC) techniques, computational algorithms that rely on repeated random sampling to obtain results. Several radiation physics MC codes were developed, being able to accurately simulate radiation transport, as well as sources, detectors and other bodies. Some examples of these codes are PENELOPE, GEANT, MCNP/MCNPX, etc. [21]. Given the clear difficulties in measuring absorbed dose in patients, the subject of dose estimates in CT became increasingly grounded in MC calculations, coupled with anthropomorphic computational phantoms [20]. More recent approaches to this issue include

the Size-Specific Dose Estimate (SSDE), which is still grounded on the use of PMMA phantoms [22]. Nowadays, the use of computational phantoms has greatly evolved. This subject will be further explored and reviewed in Chapter 3.

With all the aforementioned factors in consideration, the reduction of CT radiation exposure to the population is urgent, as well as the improvement of population awareness, in order to avoid high cancer incidence down the line. The development of better and more precise methods for patient and organ dose calculation is essential to provide better quality medical diagnostic with minimal risk to the patient and, consequently, improve public health.

1.2 Objectives

The main aim of this investigation was to modify existing Three-Dimensional (3D) voxel phantom models, so to adapt average models to single patient anatomies, trying to ideally approximate to a more personalized patient dosimetry. To accomplish this, a program needed to be developed. The FORTRAN program here developed is able to create a voxel phantom adjusted to a specific patient, by changing the overall size of the patient, as well as modifying the voxel phantom's organ dimensions. This work focused essentially in one of the biggest and most radiosensitive organs in the thorax, the lungs. Organ doses in several body organs were also calculated using the PENELOPE software, in order to compare organ doses between the standard voxel phantom and the patient adapted voxel phantom.

1.3 Thesis Outline

The present dissertation is distributed over seven chapters. **Chapter 1** presents a broad description of the Computed Tomography's current status as an area of research, illustrated by some significant statistics. The dissertation's aims are also described here. This chapter ends with a description of the thesis outline.

In **Chapter 2** information on the subject of interaction of radiation with matter is presented, followed by a brief review of the main historical landmarks of CT, as well as its constitution and functioning. In addition, an overview of basic theoretical concepts of dosimetry, as well as of several CT dosimetry parameters, is presented.

Chapter 3 contains the actual state of the art of this dissertation. In this chapter, several methods to determine patient dose in CT are presented and reviewed. First are presented the dose estimates in CT using physical phantoms, followed by the evolution and characteristics of the usage of computational anthropomorphic phantoms. Finally, some techniques using computational phantoms to provide organ dose estimates are presented.

Chapter 4 includes the materials and methods applied in this dissertation. It starts with a description of the hardware used to perform measurements. The measurement

procedure is also explained. Additionally, thorough description and functioning with the ICRP Reference Phantoms are presented. As to the software developed during the thesis, a detailed overview of its purpose and functioning are depicted. Also, in this chapter, the patient/phantom body and lung matching procedures are presented.

In **Chapter 5** the Monte Carlo methods are briefly described and the PENELOPE and PenEasy MC codes are succinctly explained, followed by an explanation of the PenEasy input file. Additionally, the MC implementation of CTDI measurements, as well as of the standard ICRP and modified voxel phantoms, is thoroughly described.

Chapter 6 presents the results and discussion. Finally, in **Chapter 7** the general conclusions are presented, as well as a discussion of possible future work.

Chapter 2

Theoretical Fundaments

This chapter begins with an introduction to the field of interaction of radiation with matter, followed by a brief review of the main historical landmarks of CT, as well as its constitution and functioning. Additionally, an overview of basic theoretical concepts of dosimetry, as well as of several CT dosimetry parameters, is presented.

2.1 Interaction of Radiation with Matter

Radiation can be classified into two main categories: non-ionizing and ionizing, depending on its ability to ionize matter. The ionization potential of atoms, i.e., the minimum energy required for ionizing an atom, ranges from a few electron volts to 24.6 eV. Ionization potentials of all other atoms are between the two extremes.

Ionizing radiation may be classified in directly ionizing radiation and indirectly ionizing radiation. Directly ionizing radiation corresponds to charged particles, such as protons, electrons, alpha particles and heavy ions. These particles deposit their energy in the absorber through Coulomb interactions with the nucleus and electronic cloud of the absorber's atoms. Indirectly ionizing radiation relates to particles with neutral charge, such as photons and neutrons. This type of radiation deposits its energy in the absorber material through a two step process. On a first step, the neutral particles interact with the nucleus and/or orbital electrons of the absorber, originating charged particles in the process. In the second step, the charged particles will deposit their energy directly on the absorber's atoms through the aforementioned process [23].

When a photon beam transverses a material, one of two events might occur to a given photon: either the photon does not interact with the material and keeps its trajectory or the photon interacts with the material. In this way, unlike directly ionizing radiation, photons do not lose energy steadily as they penetrate matter, being able to travel some

distance before interacting with a nucleus or electronic cloud of the absorber's atoms [24]. There are essentially five types of interactions photons may have with matter: photoelectric effect, compton (incoherent) effect; rayleigh (coherent) effect, pair production and photonuclear reaction. Depending on the photon energy and the absorber's atomic number, some interaction processes may occur with higher probability than others, contributing more to the attenuation of the photon beam [23]. Considering that diagnosis radiological imaging usually uses energies between 15 and 150 keV, it is possible to infer what are the most relevant processes. The energy range used in diagnostic medical imaging promotes photoelectric effect, Compton effect and Rayleigh Effect [25].

2.2 Fundaments of Computed Tomography

X-ray CT triggered a revolution in the field of medical imaging. The two people generally credited with the invention of Computed Tomography, Allan Cormack and Godfrey Hounsfield (depicted in Figure 2.1), were awarded the Nobel Prize for Physiology or Medicine in 1979. After the publication of Cormack's theoretical idea, the work of Hounsfield at the Central Research Laboratories of Electric and Musical Industries (EMI) Ltd. allowed the construction of the first CT scanner [26]. At the time, EMI was the record company of the Beatles. It has been claimed that only due to the band's massive success EMI was able to fund Hounsfield's research, making development of CT a direct result of the Beatles' sucess [27].

Figure 2.1: Alan MacLeod Cormack (left) and Godfrey Newbold Hounsfield (right) are the co-creators of Computed Tomography [26].

In late 1973, the first commercial CT scanner, the EMI CT 1000 was on the market. Comparing the first scanners available in the market with today's successors, it is astonishing how much progress has been made in their design and manufacture in only a few decades. The EMI CT 1000's scan took about 4.5 minutes and presented an 80x80 pixels image matrix, while contemporary CT scanners can scan in few hundred milliseconds and reconstruct an image of 2048x2048 pixels [26]. Nowadays, CT is a 3D whole body imaging procedure suitable for a broad range of applications, including cardiology, angiography, interventional radiology, oncology and radiotherapy planning [28].

CT is an imaging method that allows the acquisition of Two-Dimensional (2D) images from 3D anatomy using a mathematical technique known as reconstruction. When an x-ray beam travels through a patient, it is attenuated differently by different body structures (with different densities). Therefore, CT is an exam only sensitive to density differences, representing images on a gray scale [27]. In one acquisition, the x-ray tube and detector array (which are diametrically opposed) rotate 360º in the slip ring around the patient, acquiring different images (called projections) and measuring the attenuation of x-rays with constant spacing. When a rotation is completed, the calculated attenuation values are used by a reconstruction algorithm to obtain a 2D image in the axial plane, also known as slice. Several image sets are obtained by 'slicing' the patient's body several times at different coordinates along the longitudinal axis of the patient. The resulting images are reconstructed in the sagittal and coronal planes. CT can then be understood as an extension to conventional planar X-rays [29].

Though there have been differences in design through different generations of scanners, the main components in a CT equipment are:

- The **gantry** is a circular support into which the patient is moved during the scan. This component allows the X-ray source and the detector array to rotate diametrically opposed and synchronously in the slip ring;
- The **slip ring** is a structure located within the gantry that passes electrical power to the rotating components of the CT, such as the x-ray tube and the detector array, allowing them to rotate continuously around the patient;
- The **X-ray tube/source** is the source of the X-rays that pass through the body within the gantry and transmit the information about the body's structure to the detectors. This information is in the form of a series of projections;
- The **detector array** receives several radiation intensities from X-ray beams that have passed the examined body and converts them to electrical quantities; which are then used in image reconstruction;
- The **table** is where the patient is positioned during the scan. Its position can be easily controlled, allowing the operator to position the patient according to the protocol and the part of the body being examined [26].

Nowadays, CT scans available on the market are accompanied by software that allows utilization and control of CT equipment. Through these softwares, radiologists can access several dosimetric parameters, many times even before the exam (the parameters presented before the exam are calculated using PMMA phantoms) [20], [22]. The availability and technological advent of CT encourage a high frequency use of the technique and raise the dose to the patient in each exam, respectively. Given the possible harmful effects of ionizing radiation to public health, the use of ionizing radiation in any field of study should be scrutinized and regulated.

2.3 The Radiation Protection International System

Ionizing radiation has been used in the fields of medicine, industry, power generation, waste management and weapon production. Ionizing radiation has the potential to greatly benefit people's quality of life, but only if it is used safely. Potential risks must be accessed and controlled [23], [30].

The Radiation Protection International System rests on the protection of individuals and environment from the hazardous effects of ionizing radiation. Specific radiation protection rules and standards, such as the ones recommended by ICRP and International Commission on Radiation Units and Measurements (ICRU), are traditionally applied to the "peaceful use of atomic energy". Different criteria might be used for applications such as space exploration or military purposes [24]. Around the world there are other agencies that also contribute to regulate radiation usage and establish several dosimetric quantities and units, which allow easier and more accurate dose assessment. UNSCEAR compiles and examines scientific knowledge published around the world and materializes it in its reports. The International Atomic Energy Agency (IAEA) establishes scientific and technical international cooperation in the nuclear field, as well as Basic Safety Standards (BSS). BSS stipulate security regulations in all ionizing radiation related sectors. In the European Union, the European Atomic Energy Community (EURATOM) works closely with ICRP and IAEA. This agency establishes general principles for radiological security and protection, as well as the correct usage of ionizing radiation [28], [30], [31].

The Radiation Protection International System articulates around three fundamental principles. These principles, established by the ICRP and published in the ICRP-60 publication in 1990, are defined as follows:

- The principle of **Justification** rests on the concept that every exposure altering decision should be subject to scrutiny, weighing its benefits and risks. Considering medical applications, this principle translates into the assumption that any medical procedure should only be performed when the clinical benefits exceed the procedural risks (including radiation risk).
- The principle of **Optimization of Protection** relates to the As Low As Reasonably Achievable (ALARA) principle. The probability of radiation exposure, the number

of people exposed and the magnitude of individual doses should all be maintained as low as reasonably achievable. Medically, this principle states that any radiation that is clinically unnecessary or unproductive needs to be avoided. Patient dose values are optimized when imaging is achieved with the minimal amount of radiation necessary.

- The principle of **Application of Dose Limits** advocates that the dose values to any individual originated in regulated sources in planned exposure situations cannot surpass the limits indicated by the ICRP. Nevertheless, this principle does not apply to medical radiation exposures to patients, because it has to be outweighed with the clinical benefits of the exposure [32].

2.4 Fundaments of Dosimetry

Dosimetry is a physics field that studies the determination of energy imparted to matter by radiation. The radiation delivered to biological tissue is responsible for physical, chemical and biological alterations, in this order. Several quantities and units may be used to quantify and characterize radiation doses [25].

2.4.1 Radiometric Quantities

The **particle number**, dN, corresponds to the number of particles that are emitted, transferred or received.

The **radiant energy**, dR, is the energy (rest energy excluded) of the particles emitted, transferred or received.

The **fluence**, Φ, results from the quotient between the number of particles, dN, reaching a sphere with cross sectional area, dA. Fluence's International System of Units (SI) unit is m^2.

$$\Phi = \frac{dN}{dA} \quad [m^{-2}] \tag{2.1}$$

Considering the radiant energy of the incident particle (or the sum of the energies of all particles, in case of a radiation beam), dR, and the cross sectional area of a sphere, dA, the **energy fluence**, Ψ, can be defined as the quotient between the two. Energy fluence is expressed in Jm^{-2} [33].

$$\Psi = \frac{dR}{dA} \quad [Jm^{-2}] \tag{2.2}$$

2.4.2 Dosimetric Quantities

Kinetic Energy Released to Matter (Kerma) is defined for uncharged particles, such as photons. As previously stated, indirectly ionizing radiation deposits energy in matter through two phases. In the first phase, the photon's energy is transferred to secondary charged (directly ionizing) particles, which will deposit their energy in matter by Coulomb interactions in the second phase. Kerma represents the mean sum of the initial kinetic energies of all the charged particles released by the uncharged ionizing particles, dE_{tr}, in a material of mass dm. The SI unit is the Gray ($1\text{Gy} = 1\text{Jkg}^{-1}$).

$$K = \frac{dE_{tr}}{dm} \quad [\text{Gy}] \tag{2.3}$$

The energy transferred from uncharged to charged particles may be spent in two ways: collisions that result in ionizations or conversion to photons. Therefore, Kerma may be divided in two parts: the collision kerma (K_{col}) and the radiative kerma (K_{rad}):

$$K = K_{col} + K_{rad} \quad [\text{Gy}] \tag{2.4}$$

The collision kerma translates into the portion of the kinetic energy of the secondary charged particles spent in collisions, resulting in ionization and excitation of atoms in matter. The radiative kerma relates to the part of the initial kinetic energy of the charged particles that is converted in photon energy, in phenomena such as *bremsstrahlung*. The average portion related to radiative kerma is generally the bremsstrahlung fraction, $\overline{g}$. The relation between total kerma and collision kerma may then be expressed as:

$$K_{col} = K(1 - \overline{g}) \tag{2.5}$$

Kerma is only defined when referring to the material where the energy conversion is happening. For example, if the material is air, the denomination is air kerma [28], [33].

Exposure, X, is related to the ability of photons to ionize air. It is the quotient between the total charge of ions of one sign, dq, produced by the interactions of incident photons in air of mass dm, when all the secondary electrons and positrons are completely stopped in air. Its unit, Röntgen (R) is defined as a charge of $2.58\text{x}10^{-4}$ C produced per kilogram of air. The SI unit for exposure is Ckg^{-1} [23], [33].

$$X = \frac{dq}{dm} \quad [\text{Ckg}^{-1}] \tag{2.6}$$

The mean energy imparted, $\overline{\varepsilon}$, to matter in a given volume depends on R_{in} and R_{out}, the mean radiant energy that all charged and uncharged ionizing particles that enter or leave the volume, respectively. The sum of all changes of the rest energy of nuclei and elementary particles that happen inside the volume, $\sum Q$, also affects the mean energy imparted.

$$\overline{\varepsilon} = R_{in} - R_{out} + \sum Q \quad [\text{J}] \tag{2.7}$$

The **absorbed dose**, D, is the quotient of the mean energy imparted by ionizing radiation, $d\bar{\varepsilon}$, to matter of mass dm [33].

$$D = \frac{d\bar{\varepsilon}}{dm} \quad [\text{Gy}] \tag{2.8}$$

Since the concept of absorbed dose cannot correlate the different types of radiation and its different biological effects, the necessity arose for quantities such as equivalent dose and effective dose.

The **equivalent dose**, H_T, due to radiation of type R, corresponds to the sum of all absorbed doses in the volume of a specified organ or tissue T, taking into account the correspondent radiation weighing factor, W_R. The SI unit for equivalent dose is the Sievert ($1\text{Sv} = 1\text{Jkg}^{-1}$). When considering photons, the radiation weighing factor is equal to 1.

$$H_T = \sum_R D_T W_R \quad [\text{Sv}] \tag{2.9}$$

The **effective dose**, E, is defined as the weighted sum of tissue equivalent doses, where W_T is the tissue weighing factor. The tissue weighing factors recommended by the ICRP for several organs and tissues are presented in Table 2.1. The sum of all tissue weighing factors from all the tissues in the body is 1. The SI unit for effective dose is the Sievert [34].

$$E = \sum_T H_T W_T = \sum_T W_T \sum_R D_T W_R \quad [\text{Sv}] \tag{2.10}$$

Table 2.1: Recommended tissue weighing factors for various organs and tissues. Adapted from [34].

Tissue	W_T	$\sum W_T$
Stomach, lung, colon, bone marrow, breast, remainder tissues	0.12	0.72
Gonads	0.08	0.08
Liver, thyroid, esophagus, bladder	0.04	0.16
Brain, salivary glands, skin, bone surface	0.01	0.4
Total		1

2.4.3 Dosimetric Quantities in CT

Since Computed Tomography's discovery there have been several efforts regarding the creation and optimization of specific dosimetric parameters, so that dose estimates may be as precise as possible. CTDI is globally the most employed parameter as a measurement of dose in a CT scan.

When performing a CT scan, each slice of tissue is exposed to radiation not only when it's being scanned, but also when adjacent slices are scanned. The exact value of additional

dose received by one slice through the examination of adjacent slices depends on several aspects, such as the equipment's geometry, collimation, spacing between slices and slice position. The medium cumulative dose value in a series of slices with constant spacing is denominated **Multiple Slice Dose Average (MSAD)**. MSAD may vary between 1.25 and 1.4 times the dose value in a single slice, depending on the aforementioned factors. Although an IC measurement can easily determine the dose that the adjacent slices receive from one slice, the dose that the one slice receives from its adjacent slices is the one that really matters. This value corresponds to the CTDI, which can be defined as the integral dose value in a slice [35]. The concept of CTDI is explained in Figure 2.2.

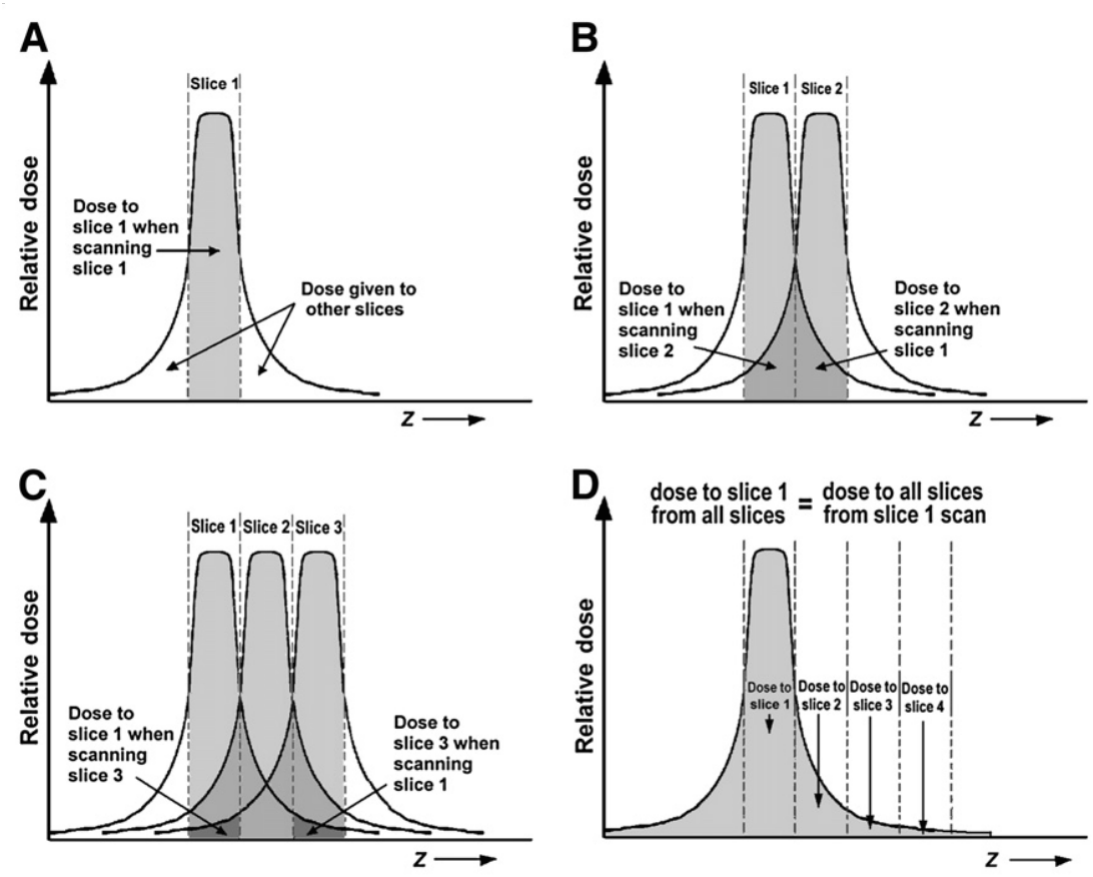

Figure 2.2: Set of four figures illustrating the concept of CTDI. **A:** Dose received by slice 1 from the scan of slice 1. **B:** The dose received from slice 1 from the scan of slice 2 is equal to the dose received by slice 2 from the scan of slice 1. **C:** The dose received from slice 1 from the scan of slice 3 is equal to the dose received by slice 3 from the scan of slice 1. **D:** The dose received by slice 1 from the scan of all slices is equal to the dose received by all slices from the scan of slice 1. This dose value corresponds to the CTDI [35].

The concept and measurement of the CTDI were proposed and established by the Food and Drug Administration (FDA) in the United States of America. [Shope 1981] The CTDI is measured in standard, cylindrical phantoms, constituted by PMMA. The phantoms are typically 15cm long and 16 or 32cm in diameter for head and body phantoms, respectively. When measuring dose values in the phantoms, an IC, typically 100mm long, is inserted

in each of the phantom's orifices. CTDI may then be calculated as is shown in the next equation, where $D(z)$ is the dose distribution along the z axis and x refers to the phantom orifice in which the dose is measured [20], [36].

$$CTDI_{100,x} = \int_{-50mm}^{+50mm} D(z)dz \quad [\text{Gy}] \tag{2.11}$$

Since CTDI value may vary significantly in the range of the phantom's diameter (dose values would be higher in the periphery than in the center), necessity arose for the Weighted Computed Tomography Dose Index (CTDI_W). This value is calculated using IC measured values from the phantom's center (c) and periphery (p) [35].

$$CTDI_W = \frac{2}{3}CTDI_p + \frac{1}{3}CTDI_c \tag{2.12}$$

In the early 2000s the concept of CTDI was questioned, due to the introduction of wider CT detectors. The new collimation widths were near or exceeded the length of the standard CT IC, 100mm. In this situation, primary radiation would not be considered completely and the scattered radiation would contribute only partially [20]. In 2007, Boone et al. showed that CTDI values measured with a standard IC (10cm long) on a PMMA phantom (15cm long) are underestimated, when compared to those measured on a phantom of infinite length. The ratio of CTDI_{100} to the limit value for infinite phantom length was found to be approximately constant up to 40mm collimation, though it greatly declines for wider collimation [37]. Another investigation, performed by Perisinakis et al., discovered that the CTDI_W measured using a 100mm IC on the standard head and body phantoms were 15% and 27% lower, respectively, than CTDI_W values measured in a 45cm long phantom. This study also stated that the minimum length of the IC and PMMA phantoms for an accurate determination of CTDI_W is 50cm [38].

Two solutions were proposed for wide collimations. The American Association of Physicists in Medicine (AAPM) considered the use of extended phantoms, either one single 50cm long phantom or three phantoms in a row, with 30cm each. Measurements could be made using a standard IC and table translation [39]. The other solution is to increase the length of the IC. In 2010, the International Electrotechnical Commission (IEC) confirmed the existing CTDI principles for collimation widths not wider than 40mm, introducing a correction factor (measured with a 300mm IC) to the CTDI definition for wider collimations [20]. The dosimetric parameters previously presented assume an exam with contiguous slices, where slice spacing I equals slice thickness, T. For helical CT, the quantity analogous to slice spacing is the pitch, P. The pitch corresponds to the quotient between the table movement per 360º gantry rotation, I, and nominal slice thickness, NT.

$$P = \frac{I}{NT} \tag{2.13}$$

Helical CT scans usually use pitch values greater than 1 (wider spacing for x-ray beams from consecutive rotations), while multislice exams use pitches lower than 1 (narrower

spacing provoking overlap between x-ray beams from adjacent rotations). To account for the effect of pitch in a helical exam dose and, for axial scans, to account for when when slice spacing I differs from slice thickness T, the quantity Volume Computed Tomography Dose Index ($CTDI_{vol}$) was introduced:

$$CTDI_{vol} = \frac{CTDI_W}{P} \tag{2.14}$$

The value of $CTDI_{vol}$ is required for each CT scan, and it should be provided by the manufacturer and presented on the scanner console. The problem with $CTDI_{vol}$ is that it neither takes patient size and cross section into consideration, nor the length of the irradiated volume. One indicator that is proportional to the length of the irradiated volume is the Dose-Length Product (DLP), represented in the next equation, where L is the total z-direction length of the scan.

$$DLP = CTDI_{vol}L \tag{2.15}$$

Though the DLP is a parameter proportional to the total deposited energy in the patient, it is not an adequate risk indicator, due to not accounting for the radiosensitivity of the irradiated tissues. For that purpose, the parameter effective dose, E, should be used [35]. Effective dose can be calculated by multiplying DLP by k-factors, which are conversion coefficients specific to each type of organ and tissue (more information in section 3.3) [35], [20].

The CTDI and DLP concepts have greatly dominated CT dosimetry, being standard quantities for various tasks, such as acceptance and quality testing of CT apparatus and comparisons between CT scanners and protocols. Still, both CTDI, $CTDI_{vol}$ and DLP can only offer rough estimates of the patient dose levels involved. Since they are determined for cylindrical PMMA phantoms, they cannot match the patient situation well. Patient-specific dose estimates taking into account patient dimensions, cross section and anatomy, would be preferable [20].

Chapter 3

Dose Estimates in the Patient

In diagnostic radiology, the radiation dose to the healthy tissues could be a burden and should always be minimized. Therefore, the radiological protection scientific community has shown continuous interest in finding more practical and accurate methods to estimate dose. Over the last 50 years the use of models of human anatomy to calculate radiation dose has grown exponentially. Accurate radiation dosimetry in the human body is inherently challenging due to several reasons:

- Exposure scenarios vary and may include complex geometrical relationships between the source and the human body;
- An exposure can involve multiple radiation types, each traversing the human body and interacting with tissues differently;
- The human body consists of various heterogeneous anatomical structures, with varying density, size, shape and radiosensitivities. Additionally, these anatomical structures are subject to organ motion.

In radiation dosimetry anatomical models are of vital importance because dose inside a living person cannot usually be directly measured. A phantom can be defined as a physical or computational device that mimics human anatomy. It has been established that dose inside the body can be calculated using either a physical or computational phantom. The accuracy of any estimate always greatly depends on the anatomical models representing the specific geometry and radiation attenuation characteristics of each individual [40].

Several methods to determine patient dose in CT are presented and reviewed. First, the existing dose estimating methods in CT using physical phantoms are described. The evolution and characteristics of the usage of computational anthropomorphic phantoms

is also reported. Finally, some techniques using computational phantoms to provide organ dose estimates are presented.

3.1 Dose Estimates using Physical Phantoms

Physical phantoms are constituted of solid materials that, from a radiological point of view, are equivalent to human tissues. The human body consists mainly of water, so materials such as water or perspex (PMMA) are common constituents of physical phantoms. These phantoms are standardized, have simple designs and are helpful for routine quality assurance measurements and comparing CT scans radiation output levels [40].

The AAPM report 204 proposed SSDE, a method to estimate patient dose to account for patient size, grounded on the principle that the CTDI_{vol} value presented by the CT scanner is not accurate and can vary according to patient diameter. For example, when CTDI_{vol} is measured in a phantom with 32 cm in diameter, then dose would be higher for patients whose diameters are smaller than 32cm and lower for patients whose diameters are bigger than 32cm. Though this trend is predictable, the calculation of numerical correction values is quite complex [20], [22]. Therefore, since in pediatric examinations the CTDI_{vol} provided by the scanner can be about four times smaller than the real dose value, the investigation and determination of correction factors is very important [41].

The AAPM report includes several tables of conversion factors, f, for the 16 and 32cm standard PMMA phantoms, depending on four possible anthropomorphic parameters based on patient diameter: Lateral Diameter (L), Anterior-Posterior Diameter (AP), L+AP and effective diameter. The formula to estimate patient dose for a specific patient size is:

$$SSDE = CTDI_{vol} \mathrm{x}\, f \tag{3.1}$$

The extensive tabulations in the AAPM report are based on a compilation of concordant data coming from different sources: (1) physical measurements using anthropomorphic phantoms; (2) physical measurements using cylindrical PMMA phantoms; (3) Monte Carlo measurements using voxilized phantoms; (4) Monte Carlo measurements using several cylindrical phantoms [22]. Nevertheless, measuring patient diameter is not a trivial task. The main drawback of this method is the difficulty with the consistent measurement of patient diameters, which may vary according to its anatomical variability [20].

Anthropomorphic physical phantoms better resemble the anatomy of the human body and can represent the entire body or only part of it. They are usually comprised by several tissue-equivalent materials shaped to resemble body organs or bones. The anthropomorphic phantoms for external radiation dosimetry applications have cavities in locations that match with organs of interest. This way, tiny dosimeters can be inserted in different locations of the phantom to measure radiation doses from external sources [40], [42]. The

main examples for this type of phantom are the RANDO phantom by the Phantom Laboratory and the ATOM phantom developed by CIRS, Inc. One of the primary downsides to this type of phantoms is the limited number of body sizes that cannot entirely reflect the human population variability [40].

3.2 Dose Estimates using Computational Phantoms

The determination of organ doses via computational phantoms and calculations became feasible with the advent of first-generation computers and simulations using MC methods. These phantoms were extensively detailed, containing information about exterior and interior features of the human body, such as shape, density, volume and chemical composition of various organs and tissues. In the 1980s, due to the advent of personal computers and the possibility to visualize anatomy in 3D through medical imaging, computational phantoms became common and widely used by the radiological community.

There are three different computational phantom generations that can be clearly distinguished: **(1)** Stylized phantoms (1960s to 2000s); **(2)** Voxel phantoms (1980s to present); **(3)** Boundary Representation (BREP) phantoms (2000s to present). Figure 3.1 contrasts these three computational phantom generations [40].

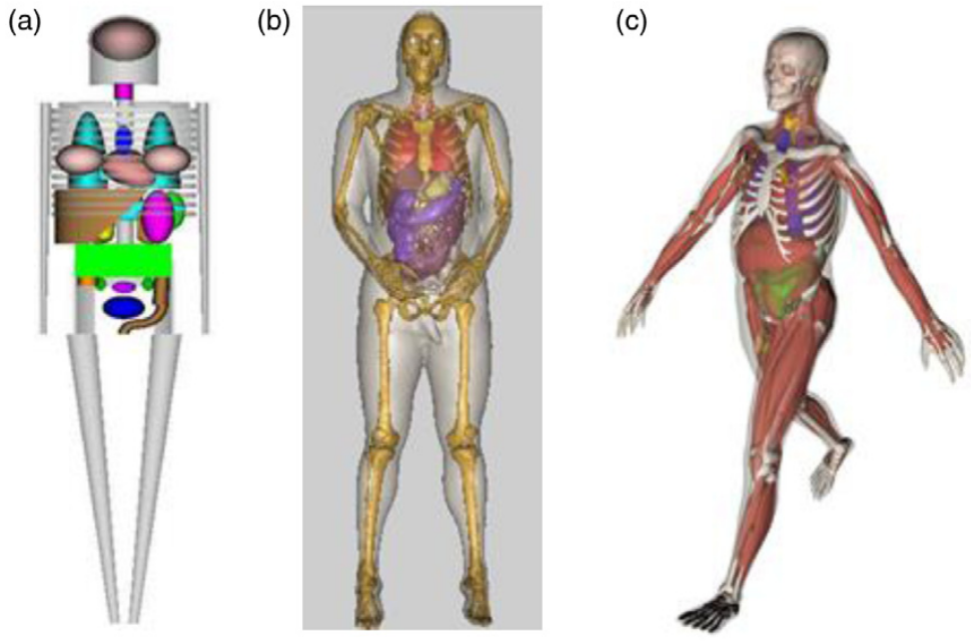

Figure 3.1: Depiction of the three computational phantom generations: **(a)** Stylized phantom; **(b)** Voxel phantom (displayed in smooth surfaces); **(c)** BREP phantom. It is possible to observe that anatomical accuracy improves from the oldest generation to the newest [40].

3.2.1 Stylized Phantoms

The first generation of computational phantoms arose with the purpose of providing better dose estimates from internally deposited radioactive materials for workers and patients [40].

The first phantom in this generation originated in the 1960s with the work of Fisher and Snyder at the Oak Ridge National Laboratory (ORNL) [43]. This phantom, called Fisher and Snyder adult phantom, was developed through the use of Constructive Solid Geometry (CSG) techniques, which were the base of development for all of the phantoms in this generation. The CSG method uses boolean operators to combine various primitive shapes such as spheres, cones, prisms or cuboids, which can be described by cuboid equations, to create a model of human anatomy. The phantom was assumed to be constituted homogenously by tissue [40]. Although the original purpose of the phantom was to work with internal dosimetry, a study used the phantom to determine dose distributions from external sources of gamma rays [43]. In 1969, the first heterogeneous phantom, the MIRD-5 (Medical Internal Radiation Dosimetry) phantom, was published. The phantom was comprised of three types of tissue: lung, skeletal and the rest was homogenous soft tissue. The MIRD-5 intended to represent the 'reference man', a healthy male with average dimension that had been defined by the ICRP publication nº 23 [40], [44]. Some attempts were also made by Fisher and Snyder to develop stylized pediatric phantoms of various ages, referred to as 'similitude' children phantoms.

The first generation of computational phantoms provided crude and anatomically inaccurate phantoms because organ shape and location is quite complex and cannot be accurately described by a limited set of surface equations. By the end of the 1980s substantial efforts were directed to the development more anatomically realistic phantoms [40].

3.2.2 Voxel Phantoms

The creation and evolution of medical imaging techniques, such as CT and Magnetic Resonance Imaging (MRI) allowed for the 3D visualization of anatomical internal structures and paved the way for the development of voxel (also known as tomographic) phantoms. Voxel phantoms, which could more accurately describe human anatomy, were essentially based on three types of anatomical images: CT and MRI images of live subjects, and cross sectional images of cadavers. Voxel phantoms are models of the human anatomy consisting of several voxels (3D pixels) grouped together to model several anatomical structures. Since a voxel is a cuboid, tomographic phantoms are also based on CSG methods [40].

It is widely believed the first image-based phantom for radiation dosimetry was developed by Gibbs et al. to assess patient dose during dental radiological procedures [45]. In the late 1980s a research team in Germany used 3D CT imaging to create the GSF

(National Research Center for Environment and Health, Institute of Radiation Protection) family, a family of 12 voxel phantoms composed by an adult male, an adult female, pediatric and pregnant woman phantoms [40]. Posteriorly, two of the adult phantoms belonging to the family previously mentioned, GOLEM and LAURA, suffered several modifications to become the REX and REGINA phantoms. The ICRP male and female reference phantoms have the same anatomy as REX and REGINA, but updated elemental tissue composition. The anatomical data of both phantoms was adjusted to the ICRP data with high precision. The number of organs and tissues identified in each phantom was 140, which could be assigned to 53 different materials [46]. The ICRP reference phantoms helped the standardization of phantom-based radiation dosimetry with realistic voxel phantoms, which was a real need in the radiation dosimetry field at the time. However, due to relatively large slice thicknesses (8mm in the reference male and 4.84mm in the reference female) [40], [46], there were some issues with the anatomical accuracy of the phantoms, such as the unrealistic definition of smaller organs and the skin and walled organs were reported to contain small holes [40].

The first phantom based on cross sectional color images of a cadaver, assembled by more than 4.7 billion voxels, was the VIP-Man (Visible-Photographic Man), whose cross sectional image is compared to one from a stylized phantom in Figure 3.2 [40]. Since this generation of computational phantoms had few pediatric phantoms to help with dose assessment during pediatric diagnostic and therapy examinations, researchers at the University of Florida (UF) constructed a set of pediatric voxel phantoms, divided in two series: Series A and Series B [47].

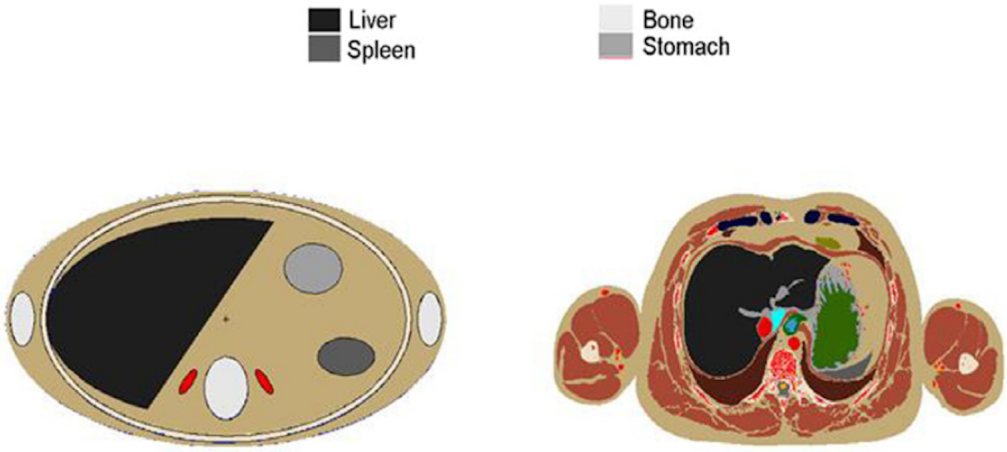

Figure 3.2: Comparison of a stylized adult phantom and the VIP-Man phantom, first phantom based on cross sectional color images of a cadaver. The anatomical features are clearly much more realistic and accurate on the VIP-Man than on the stylized phantom. Anatomical rigor is a factor that was believed to improve the accuracy of dose estimates [40].

The shift from the first to the second generation of computational phantoms was initially boosted by the voxel phantoms' improved anatomical realism. By 2014 a total of 85 different voxel phantoms had been developed all over the world. Nevertheless, there were some issues related to the development and usage of voxel phantoms. The voxel size is a very important one. While some authors seem to think that a voxel resolution in x,y and z of 2x2x2mm can represent human anatomy fairly accurately, it is not small enough to delineate some minor and very radiosensitive organs, such the bone marrow [40]. However, while a smaller voxel allows better anatomical fidelity, it also boosts the number of voxels in the phantom, which increases the computational effort during MC simulations. Therefore, there has to be a compromise between anatomical fidelity and the number of voxels.

3.2.3 BREP Phantoms

A BREP phantom is created using a tomographic image set, by acquiring the surface contours of the organs and tissues and later assembling them into a whole body model. Instead of voxels, the organ surfaces are defined by NURBS (Non-Uniform Rational Basis Spline) or polygon mesh surfaces. The main advantages of BREP are its ability to model complex anatomical details and surface deformation, which makes it ideal for tasks such as adjusting organ size, modeling organ motion and simulating the interactions of humans to the environment by varying the phantom posture [40].

Hybrid phantoms (combining voxel and BREP geometries) are thought of as the future, given their ability to represent some structures using BREP techniques and other structures, in which boundary representation is too heavy, can be modeled using voxels, this way taking the best of each generation. Since the 2000s the world has seen the interest in hybrid phantoms greatly increasing, existing nowadays a variety of hybrid phantoms families [40], [48].

3.3 Patient and Organ Dose Estimates Using MC Methods and Computational Phantoms

Modern MC method codes are able to model the CT scanner's geometry, as well as the interactions of radiation with matter. When coupled with standard phantoms, such as the ones provided by ORNL, ICRP or UF, MC dose estimation methods are considered very accurate [49].

In the 1990s, the European Commission directed significant efforts to the estimation of patient dose in CT. The primary approach intended to calculate effective dose, by using the DLP and CTDI_{in-air} values for calibration purposes. The DLP would be multiplied by conversion coefficients specific to each body part, known as k-factors [20]. This concept, only used in standard phantoms, is extensively used in the scientific community, with widely available conversion coefficients covering both genders, as well as a variety of

ages, such as adults, children and newborns [20], [50]. This technique suffers from some drawbacks, such as the ambiguous choice of body region and the broad use of the same k-factors in all CT scanners. Additionally, effective dose values are only rough estimates, being specific to the phantom and not the patient because CTDI only represents the scanner output [20]. Moreover, this method does not allow the assessment of organ dose values, one of the main quantities of interest for risk evaluation [49].

The necessity for organ dose estimates led to the development of several programs, such as ImPact and CT Imaging. This type of software relies on computational phantoms, coupled with input parameters of the CT scan and pre-calculated tables of dose contribution to each organ, to provide effective and organ dose estimates [20]. The pre-calculated tables of organ dose conversion coefficients exist for various phantoms, such as the ICRP male and female reference phantoms, and are age and gender specific [51], [52]. Though this technique is phantom specific, it can be quite useful for studying the influence of certain parameter settings on the CT scanner on patient dose [49]. It is necessary to point out that the anthropomorphic models of the aforementioned techniques rely on the ages and sizes of average individuals, not taking patient size and anatomy into account. This issue may lead to substantial errors in the assessment of organ and effective dose [49].

In 1992, Veit et al. studied the influence of patient size on organ doses in diagnostic radiology. The voxel size of the BABY phantom from the GSF family was modified in one or more dimensions and organ dose conversion factors were calculated. The study concluded that only the dimension in the direction of the irradiation has a relevant effect on the organ dose conversion factors and that the effect can be very different for various organs [53]. Caon et al. scaled the voxel model ADELAIDE in size by ±5%. Results showed that effective dose to the chest, abdomen and whole torso values tend to drop for phantoms with higher voxel volume [54]. Thus, using this approach a voxel model can be scaled to more accurately represent individual patients [55].

In 2009, Segars et al. attempted what is believed to have been the first attempt to create patient specific phantoms. The method used a deformation algorithm to transform a NCAT (NURBS-based Cardiac-torso) adult phantom, which uses BREP type surfaces, into a child model [56]. Similar methods were later used and adapted by other authors to generate whole body models of adult and pediatric patients [57], [58]. Although this type of approach has showed some promising results, it requires demanding manual labor and is very heavy computationally [49]. A study performed by Bueno et al. performed geometrical deformations on a tomographic phantom by aligning the pelvic and thoracic portions of the phantom with the geometries of patient CT images [59]. The phantom considered was MAX, a voxel phantom developed by Kramer et al. [60].

A relatively new approach to estimate individual patient and organ specific dose using MC methods was published in two studies by Kalender et al. This approach, named Patient and Organ Specific Dose Estimate (POSDE), was based on the following steps:

1. The patient CT data is used to acquire information on patient and organ size and shape in the scanned region.

2. The best fitting computational phantom is chosen by comparing lateral, anterior-posterior and effective diameters. The patient CT data are then appended at the top and bottom of the scanned volume with the rest of the corresponding phantom to construct a whole body phantom.

3. 3D dose distributions are calculated for the whole body models.

4. Organ dose is calculated inside Volumes of Interest (VOIs), defined as ellipsoid or half-ellipsoid shapes that overlap with the organs, by adding the dose values to all voxels in organ VOIs [20], [49].

During these studies, the AP and L diameters of the patients did not always match the ones of the best-fitting computational phantom, so the phantoms could be scaled or wrapped in fat-equivalent tissue layers to create slim or overweight models. Within the scope of these studies, it is important to mention that the use of whole body models instead of only the scanned range model is of primary importance when calculating dose values (represented in Figure 3.3), in order to account for: (1) scattered radiation to organs located outside the scanned region, which may still receive a significant amount of radiation; (2) backscattered radiation originated in the neighboring areas, which raises dose in the scanned region. Moreover, Kalender et al. stated that lung dose during a lung scan accounts for 10% to 50% of the total dose in the imaged volume, which makes the lungs a primary organ of concern when considering CT dose.

The use of VOIs to assess organ dose is justified by three assumptions made by the authors:

1. Organ dose values depend more on patient size and organ cross-section and chemical composition than on organ shape;

2. Dose distributions are relatively homogenous and organ dose values are not critically dependent on covering the complete organ;

3. Accurate segmentation of organ contours is a distinct and non trivial issue, particularly for routine clinical applications, though there have been developed some working solutions for larger organs, such as the lungs or liver [49].

However, this approach has some drawbacks, it is possible that not accounting for the whole volume of a given organ does not provide accurate dose measurements. Moreover, given the lack of contrast between some soft tissues in a CT image, the use of existing widely used reference phantoms with the adaptation of only some interest organs to the patient's anatomy could provide more accurate organ dose values. Since this kind of approach may be too demanding for routine clinical use, the development of a technique,

simpler at a computational level that also provides accurate organ dose values, may be of use to the radiation protection field.

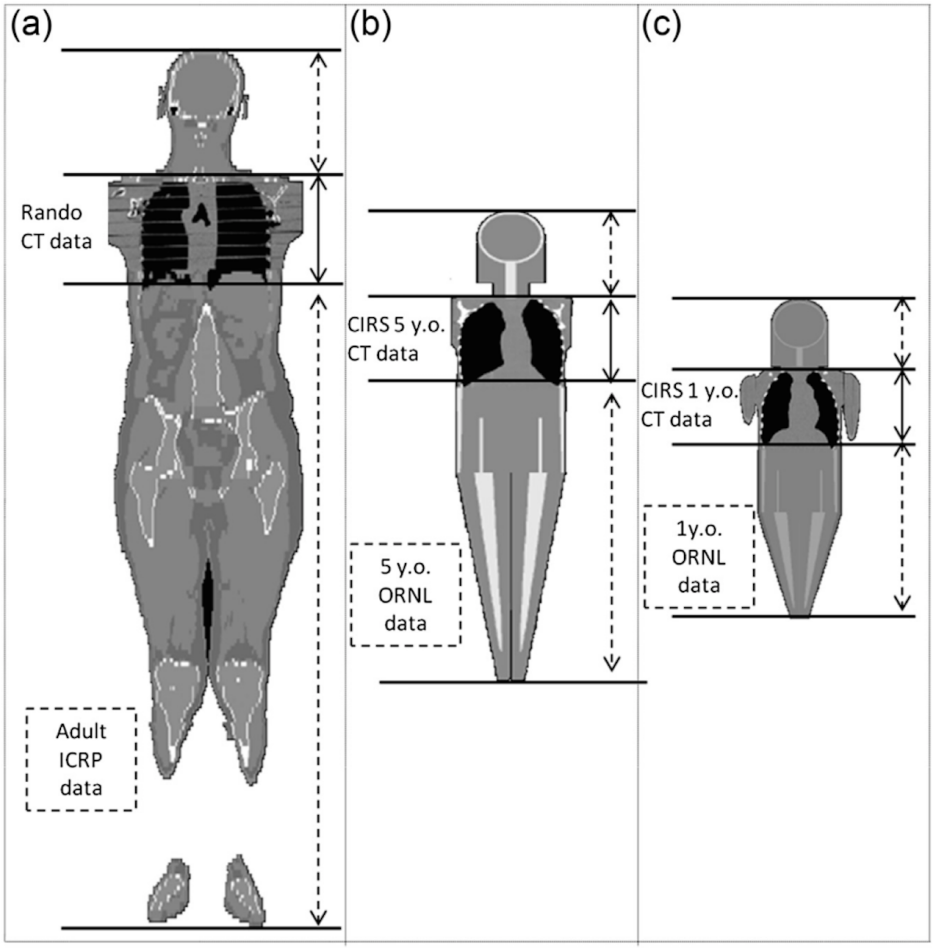

Figure 3.3: Whole body models with CT data appended at the top and bottom of the scanned volume with data from computational phantoms used in the study performed by Kalender et al. **(a)** Using the tomographic ICRP male adult reference phantom; **(b)** Using the 5 year old pediatric phantom from the ORNL family; **(c)** Using the 1 year old pediatric phantom from the ORNL family [49].

Chapter 4

Materials and Methods

Chapter 4 consists of the materials used and methods applied in this dissertation. It starts with a description of the hardware used to perform the CTDI validation measurements: the CT scanner, the IC and the PMMA phantom. The measurement procedure is also described. The characteristics and operation of the male and female ICRP reference phantoms, used during the course of this work, are also present. The elaboration of this dissertation required familiarization and learning of the FORTRAN programming language to develop two programs. So a brief history and description of the FORTRAN language is also provided in this chapter.

As to the software developed during the thesis, a detailed overview of its purpose and functioning are depicted. Two FORTRAN programs were developed during this thesis: ReadPhantom, to create the files necessary to visualize and simulate with the voxel phantoms, and ReDimLugs, with the objective of scaling the lung dimensions of a phantom. Also, in this chapter, the patient/phantom body and lung matching procedures are presented.

4.1 CTDI Measurements

Usually there is the need to validate MC calculations by measuring with physical phantoms. Therefore, a simplified MC model of the CT scan and physical phantom used in this work was developed (description of the model available in section 5.4). Good agreement between measured and simulated values (available in section 6.1) allows for the successful validation of the MC implemented model, yielding accurate and viable assessment of patient dosimetry.

4.1.1 CT Equipment

The CT scan used in this work is a LightSpeed VCT model manufactured by GE located in *Hospital São José – Centro Hospitalar Lisboa Central* (HSJ-CHLC). It is a 16 slice model and has a maximum voltage of 140kV and a maximum intensity of 380mAs.

4.1.2 Ionization Chamber

Radiation dose in radiotherapy and diagnostic radiology can be determined through the use of radiation detectors. An IC is a type of radiation detector, whose size and shape may vary according to its application. The basic functioning of an IC rests on a sensitive volume filled with gas inside the chamber. The sensitive volume is located between two electrodes connected to high voltage supply. When ionizing radiation transverses the gas volume, ion pairs are created. Consequently, the electrodes attract the positive and negative charge carriers, creating a current that can be measured. The IC usually used in CT is the standard 100mm length pencil chamber [61].

In this work a pencil IC manufactured by RaySafe was used, whose volume is in the order of $3cm^3$ [62]. The chamber has an associated uncertainty of 5% [63].

4.1.3 PMMA Phantom

The phantom used in the measurements, represented in Figure 4.1, was a Gammex CTDI phantom composed of PMMA, which has a density of $1.19g/cm^3$, with a thickness of 14.5cm. The phantom consists of three nested cylindrical modules, allowing three different configurations, which correspond to an adult body, adult head/pediatric body, and pediatric head, with a diameter of 32, 16 and 10cm, respectively. Each of the configurations has a center orifice on the central axis of the phantom and four orifices on the periphery (1cm deep) in 90 degrees intervals. The orifices have the same length as the phantom and a diameter equal to 1.31cm. Included in phantom there are PMMA rods to insert in the phantom orifices that are not being used by the IC [64].

4.1.4 Measurement Procedure

To perform the measurements the three modules of the phantom were used, materializing the adult body phantom. Before each measurement the IC was inserted in a phantom orifice, with the help of a PMMA adaptor to keep the chamber steady and perpendicular to the gantry. Then, PMMA rods were inserted in each of the empty orifices of the phantom, to maintain it homogenous. When the phantom is scanned by the CT equipment, the IC measures the dose value. This procedure was repeated three times for each of the phantom's orifices (center, 0^o, 90^o, 180^o and 270^o). The Kerma_{in-air} value was also measured for calibration purposes (considering the same distance scanner-isocenter used in PMMA measurements), with a setup shown in Figure 4.2.

Figure 4.1: The PMMA phantom used in this work [65].

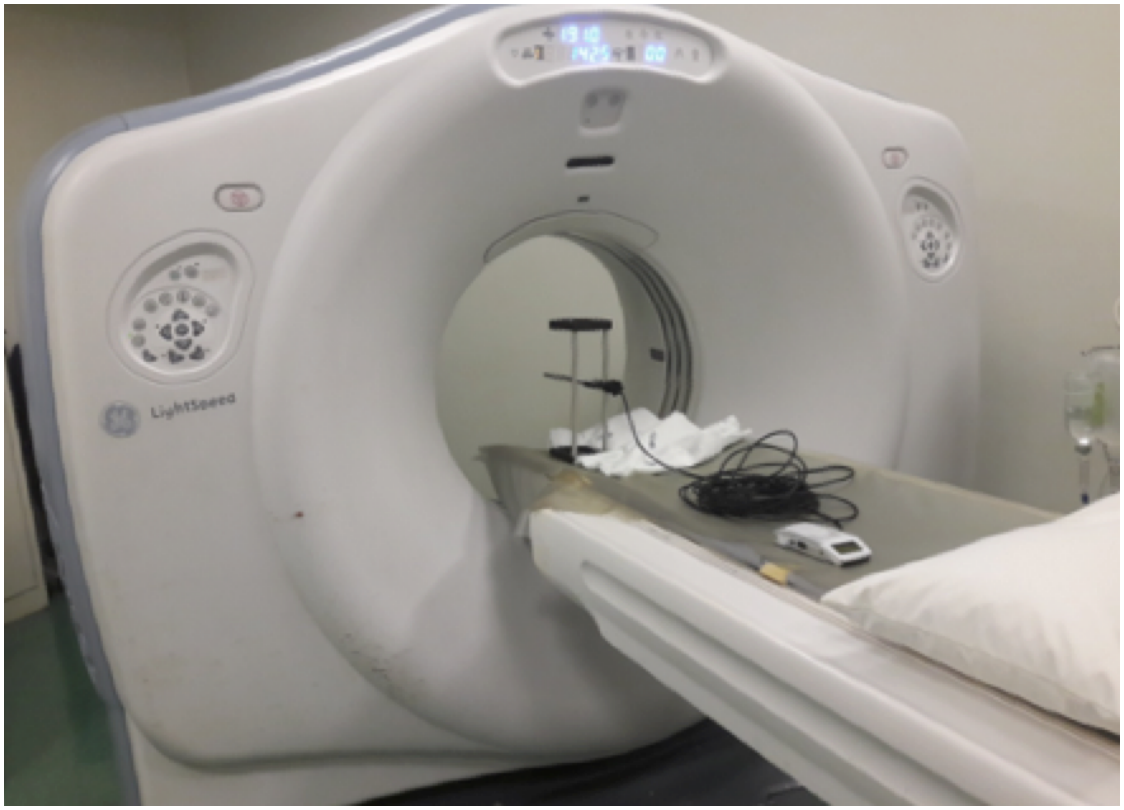

Figure 4.2: The GE CT equipment used when performing the measurements. The IC is assembled in the experimental setting to measure Kerma_{in-air}.

4.1.5 Results Procedure

The CTDI measurements for the IC inside every orifice in the PMMA phantom were performed. Three dose measurements were performed for each orifice and their average value and standard deviation, s, were calculated. The value of s was obtained using equation 4.1, in which $\overline{x}$ represents the average value for one orifice, x the value for each measurement for one orifice and n the number of measurements.

$$s = \sqrt{\frac{\sum_{i=1}^{n} (x_i - \overline{x})^2}{n-1}} \tag{4.1}$$

The $CTDI_{100}$ and $CTDI_W$ values were calculated using equation 4.2, in which D represents the measured value, 100 is the chamber length and $N \text{ x } T$ corresponds to beam thickness, and 2.12, respectively.

$$CTDI_{100} = \frac{D(\text{mGy}) \text{ x } 100\text{mm}}{N \text{ x } T(\text{mm})} \quad [\text{mGy}] \tag{4.2}$$

For calibration purposes IC measurements free-in-air were also performed, measuring 1.556 mGy for an exposure of 100 mAs. Then equation 4.2 was used to convert the IC reading into CTDI_{100} value.

Using PenEasy, MC calculations were performed on the IC free-in-air and in the phantom at the center, 0º and 90º positions. For every IC location, different source angles were simulated to describe an entire rotation, ranging from 0º to 360º in 90º intervals and for each position considered the deposited energy values were calculated. To better resemble a complete gantry rotation, a 36-point interpolation was applied to the values of deposited energy for every ionization chamber location using the statistical analysis software Origin. The MC tally and interpolation results for the IC in-air and at the center, 0º and 90º, as well graph of the 36-point interpolation performed for the chamber in the phantom at 0º are present in Appendix B. The total IC deposited energy value was obtained as the sum of the deposited energies from all source positions. The uncertainty for every IC location was calculated as the average uncertainty for every simulated source position.

The dose values were then obtained by dividing the sum of the energy deposited values for every IC position (in eV/hist units), by the mass of the IC's sensitive volume, $3.61392 \text{ x } 10^{-3}$g.

In order to obtain the total absorbed dose for a complete CT rotation, the method described by Figueira et al. [78] was used. In particular, a Conversion Factor (CF), defined in equation 4.3, was calculated.

$$CF = \frac{CTDI_{in-air,\, measured}}{CTDI_{in-air,\, simulated\ per\ particle} \text{ x } 100\text{mAs}} \quad \left[\frac{mGy\ hist\ g}{eV\ mAs}\right] \tag{4.3}$$

The simulated absorbed dose for the IC can then be calculated according to equation 4.4.

$$CTDI_{100,\,simulated} = Dose \,\mathrm{x}\, CF \,\mathrm{x}\, 100\mathrm{mAs} \quad [\mathrm{mGy}] \tag{4.4}$$

The relative difference between the measured and simulated results for the CTDI_{100} and CTDI_{W} was calculated using equation 4.5.

$$Relative\,Difference = \frac{value_{simulated} - value_{measured}}{value_{measured}} \,\mathrm{x}\, 100 \quad [\%] \tag{4.5}$$

4.2 The Male and Female ICRP Reference Phantoms

Computationally, the male and female reference phantoms are defined in a three-dimensional array of voxels, available in the form of an American Standard Code for Information Interchange (ASCII) text file. The 3D voxel array is organized in columns, rows and slices, corresponding to the coordinates in the x, y and z axis, respectively. The voxels are listed slice by slice, within each slice row by row and within each row column by column, i.e., the column index changes fastest, then the row index, then the slice index. The phantoms are constructed with the column numbers increasing from right to left, the row numbers increasing from front to back and the slices numbers increasing from the toes to the vertex of the body [66].

The ICRP male and female reference phantoms have 141 organ Identification Number (ID)s, representing the same number of delineated organs and tissues, composed by 53 different materials, each having its own density and chemical composition. The main characteristics of the male and female ICRP reference phantoms are presented in Table 4.1. The slices in both phantoms are several millimeters thick, and, therefore, represent not only skin, but also other structures present in the head and feet, such as bone, muscle and adipose tissue. The organ ID number 141 (denominated “skin at top and bottom”) represents the voxels in those slices, which are not included in the reference phantoms height and mass values. These voxels can be neglected by assigning air instead of skin to those voxels. It was decided that these voxels would not be used due to, since the main focus of this study was thorax CT, the dose value in those voxels not being of interest. In addition, when considering these voxels to be air, the phantom is simplified and, consequently, the computational effort is diminished [46].

Only the female ICRP reference phantom was used in this work and it will be henceforth referred as AF.

Table 4.1: Main characteristics of the ICRP male and female reference phantoms. Adapted from [66].

Property	**Male**	**Female**
Height (m)	1.76	1.63
Mass (kg)	73	60
Slice Thickness (voxel resolution in z) (mm)	8.00	4.84
Voxel in-plane Resolution (mm)	2.137	1.775
Voxel Volume (mm)	36.54	15.25
Number of Columns	254	299
Number of Rows	127	137
Number of Slices	222	348
Number of Tissue Voxels	1 947 375	3 886 020
Total Number of Voxels	7 886 020	14 255 124

4.3 The FORTRAN Programming Language

FORTRAN, acronym for "formula translation", is a general purpose programming language particularly useful for numeric computation and scientific programming. FORTRAN, the first programming language to be standardized, originated in 1954 during a project performed at IBM (International Business Machines Corporation). By the late 1960s, FORTRAN had grown considerably and many computer vendors implemented a FORTRAN compiler.

FORTRAN has been updated several times. Although several versions have existed throughout the years, such as FORTRAN66, FORTRAN77, FORTRAN90, FORTRAN95 and FORTRAN2003, FORTRAN is still the premier language for scientific and engineering computing applications [67].

4.4 Visualization and Simulation Files Program

The initial part of this thesis demanded the conversion of the original files containing three-dimensional arrays, which could be in either binary or ASCII format, to files that allowed visualization and simulation of the phantoms. The necessary files were the following:

- A simulation file with the .vox extension used as an input for the voxel geometry in the MC PenEasy code package [68];
- Files ct-den-matXY.dat, ct-den-matXZ.dat, ct-den-matYZ.dat, which allowed the visualization of the phantom in the axial, coronal and sagittal planes through the use of Gnuplot [69], a command-line driven graphic utility.

There were several existing FORTRAN programs available for this finality: (1) read4sim.f, which created the simulation file; (2) read4view.f, which created an intermediary file with

the .ct extension; (3) readctXY.f/readctXZ.f/readctYZ.f, to read the .ct file and create the ct-den-mat visualization files; (4) and also a file to convert ASCII phantom files to binary format, since the previously mentioned files only read phantom files in binary format. However, these files were phantom specific and the user had to temper with the code, compromising its integrity, to modify the program every time a new phantom was used.

With the objective of making this process more efficient and user friendly, the FORTRAN program ReadPhantom was developed as an integrant part of this work. ReadPhantom is a FORTRAN program that reads any phantom file, whether it is in ASCII or binary format, and creates all the necessary files for simulation and visualization in one execution. The program's user interface runs through the command line and is simple and user friendly. Additionally, a tutorial (available in Annex I) was also written as part of this work explaining the use of ReadPhantom.

This program was tested with success in both of the ICRP reference phantoms, which come in ASCII format, and in the phantoms GOLEM, DONNA, and LAURA (from GSF) and the Series B of pediatric phantoms from UF, which come in binary format. So, in general, this program is able to work with any voxel phantom file, provided that the file is coded either in ASCII or binary format.

4.5 Organ Scaling Program

The FORTRAN program ReDimLungs was created as a method to use during this thesis, with the objective of modifying the lung dimensions of a voxel phantom without significantly altering the general shape of the lungs. ReDimLungs was developed specifically for lung scaling, but the code can be easily modified so it applies to other organs, as long as they are defined in the voxel phantom. However, ReDimLungs will not work well with distributed organs, such as skin, skeleton and red bone marrow. The program operates in voxel layers and would greatly increase a distributed organ's size. The program works best with bigger organs with a simple shape, such as the lungs, stomach or liver. Additionally, ReDimLungs was developed to work specifically with AF, though it can deal with most voxel phantoms. Although the program runs in the command line, its operation occurs via input and output files, such as:

- **ct-den-matXY.dat:** ReDimLungs reads the phantom from a ct-den-mat type file (this file can be obtained via the ReadPantom program) and writes the scaled phantom to another one.

- **ReDimLungs.in:** The input file is necessary to run the program. In this file the user inputs some parameters necessary to run the program, such as the organ to scale or the names of the input files.

- **ReDimLungs.out:** The output file of the program reports in detail the program's execution.

- **tasks.dat:** The user must write in this file the tasks the program needs to perform. Each task corresponds to a line. In each line there should be three characters, corresponding to the direction in which the scaling should be performed, whether the program should add or delete layers and if the layer should be altered on the positive or the negative side of the axis. The following list presents the characters that can be written in this file:
  - **x:** the x axis direction;
  - **y:** the y axis direction;
  - **z:** the z axis direction;
  - **a:** add layer;
  - **d:** delete layer;
  - **p:** on the positive side of the axis;
  - **n:** on the negative side of the axis.
- **Organlist.dat:** This file contains the organ list of the used voxel phantom. In the case of AF, it contains 142 lines, corresponding to 141 segmented organs and tissues and air. Each line should have three values: the organ ID and the corresponding material ID and density.

Basically, the program ReDimLungs is able to store the voxel phantom information in a three-dimensional array and scan it in the form of x-vectors, y-vectors and z-vectors. AF has 299 voxels in the x direction, with the voxel coordinates ranging from 1 to 299. In an analogous way, the phantom has 137 and 348 voxels in the y and z directions, with the voxel coordinates ranging from 1 to 137 and from 1 to 348, respectively. A x-array is then a set of 299 organ IDs covering the phantom from x=0 to x=299 with constant y and z coordinate values. Similarly, a y-array and a z-array are sets of 137 and 348 organ IDs with constant x and z coordinate values and x and y coordinate values, respectively. The functioning of ReDimLungs when performing a lung in a voxel phantom can be summarized in ten steps:

1. Read the phantom from the ct-den-matXY.dat file and store the organ IDs it in a three-dimensional array.
2. Detect the slices in which the lung ID is present and cut the corresponding phantom portion, plus some slices of tolerance to allow flexibility when scaling the lung. From this point on ReDimLungs will work only on the separated portion.
3. Detect the organ dimensions in the x axis direction and store the information. The program scans the portion analyzing all the x-arrays present in the portion. If the lung ID is found in one x-array, then detect and store the minimum (named the negative side of the axis) and maximum (named the positive side of the axis)

x values that have the lung ID. The lung size in the x-array can be calculated by subtracting the minimum x value to the maximum x value. The information is stored in a file.

4. Detect the organ dimensions in the y axis and z directions and store the information in files by repeating step 3 for all y-arrays and z-arrays. The lung overall size in every dimension is reported to the output file.

5. Read a line from the tasks file. The program will perform one scaling task. If the scaling is to happen on the x direction, then the x-arrays information is retrieved. For each x-array containing lung voxels, the following procedure is repeated (this procedure, described in Figure 4.3, is analogous for the y and z directions):

    a. If a layer is to be added to the lung on the negative or positive side of the axis, then the voxel immediately adjacent to the minimum or maximum lung x value will be set to lung ID. If the adjacent voxel has stored the organ ID of the other lung or any kind of bone, then the program does nothing;

    b. If a layer is to be deleted to the lung on the negative or positive side of the axis, then the voxel corresponding to the minimum or maximum lung x value will be set to the organ ID of the voxel immediately adjacent to it. If the adjacent voxel has stored the organ ID of the other lung, air or of any kind of bone, then the voxel corresponding to the minimum or maximum lung x value will be set to blood organ ID.

6. Detect the organ dimensions in all axis directions again. The lung overall size in every dimension is reported to the output file.

7. Repeat steps 5 and 6 for every task (line) in the tasks file.

8. Verify if there are any lung blood voxels outside the lung. If there are, replace them with organ ID 88 (heart blood).

9. Append the retrieved phantom portion back into the whole voxel phantom array. Detect the total number of voxels in both lungs, as well as in some organs of interest and write the result to the output file.

10. Write the new phantom to a new ct-den-matXY.dat type file for visualization and to a .vox type file for simulation.

ReDimLungs also has some limitations to its functioning. Since the program works in voxel layers, in order to preserve the general shape of the organ during its execution, scaling in one dimension may affect the other dimensions if a big enough number of tasks is performed. In addition, while performing the scaling, the minimum and maximum organ size values in a particular axis may not change. That happens because the particular

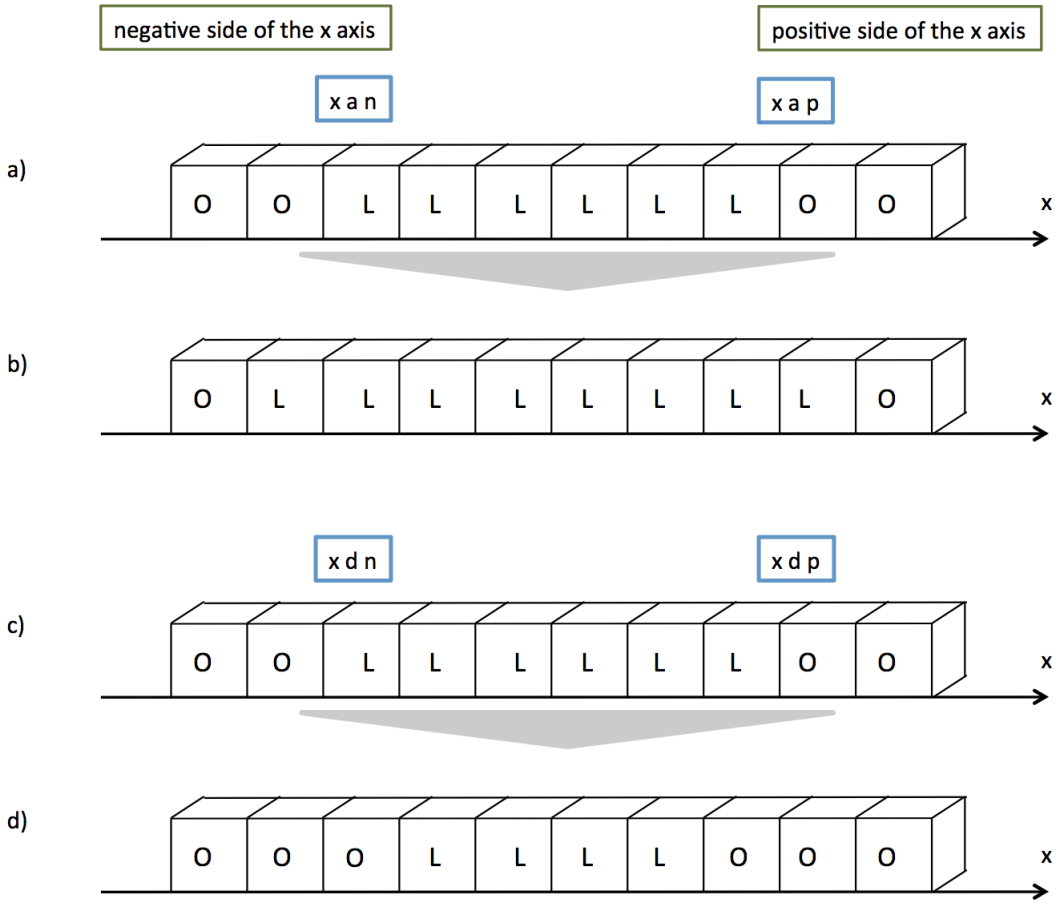

Figure 4.3: Representation of the action ReDimLungs takes when scaling a x-array: **a)** before adding a layer on the positive/negative side of the axis; **b)** after adding a layer on the positive/negative side of the axis; **c)** before deleting a layer on the positive/negative side of the axis; **d)** after deleting a layer on the positive/negative side of the axis. The cubes marked with L and O represent voxels with lung ID and other organ ID, respectively. The commands inside the boxes delineated in blue in a) and c) represent the commands that need to be placed in the tasks file for the lung scaling to happen from a) to b) and from c) to d). The boxes delineated in green represent the negative and positive side of the x axis, i.e., the maximum and minimum x coordinates of the voxels that have lung organ ID in each x-array.

organ to which the adjacent voxel belongs is not affected by the scaling (more information on step 5). For example, in the x direction, for a single task, the organ size will not be scaled in that particular x-array, although the other x-arrays are scaled as usual.

4.6 Patient/Phantom Matching Procedure

One of the main objectives of this work was to modify existing voxel phantoms to resemble the anatomy of individual patients. This section describes the procedure developed and implemented during the course of this work, to convert a voxel phantom to a patient phantom, with adapted voxel resolution and scaled lung dimensions.

4.6.1 Description of the Patient CT Images

The information on the patients' anatomy was retrieved from sets of CT images provided by HSJ-CHLC. The DICOM (Digital Imaging and Communications in Medicine) images represented the CT scans of six adult female patients. All the images were obtained using the same protocol, the 5.1. Routine Thorax, a protocol generally used to allow the visualization of the whole or some part of a patient's thorax, whose most relevant characteristics in the context of this work are listed:

- Spectrum: 120kV peak voltage;
- Distance source-patient: 541mm;
- Distance source-detector: 949.147mm;
- Distance patient-detector: 408.147mm.

When a CT scan is performed using this protocol, usually two low-dose scout images, also known as topograms, are performed, one with the source at 0º and one with the source at 90º). For each exam, the topograms represent a Field of View (FOV) that has a reference point corresponding to the sternal furcula for thorax examinations. The sternal furcula is an anatomical structure that corresponds to the depth that can be felt at the top of the manubrium (top section of sternum), located between the anterior tips of the clavicles. The FOV is then usually visualized approximately 60mm upwards and 300mm downwards from the sternal furcula (reference point). This is what happens in most thorax examinations. However, depending on the patient's dimensions and the purpose of the scan, the radiologist or physician may decide to change the FOV, which means there will exist different dimensions upwards and downwards from the sternal furcula. The size of the topogram images is then 530x360.55mm and 888x661pixels. By dividing the image size by the number of pixels in each dimension it is possible to determine the pixel size, which is approximately 0.5968x0.5454mm.

4.6.2 Matching the Phantom Size

The objective definition of the diameters of individual patients is not a trivial matter, due to the diameters varying strongly with the anatomical level of the patient and within the examined range [20]. One of the main concerns when measuring patient diameters was to consistently measure in approximately in the same axial plane. To overcome this issue, the location of the sternal furcula was used as a reference point. Thereby, it was decided that the patient's L and AP diameters would be measured 23cm below the location of the sternal furcula, given that this location would almost always match with the part of the thorax containing the end of the lungs.

Firstly, using the image analysis platform ImageJ [70], the anterior-posterior and lateral diameters were measured for each patient in each topogram image approximately 23cm downward from the patient's sternal furcula. Since the images obtained were all from adult female patients, the AF was used to model them. AF was also measured about 23cm below the sternal furcula. AF's AP and L diameters were compared with the patient's AP and L diameters and the new phantom's resolution in x and y, respectively, was calculated though direct proportionality. AF's resolution in z was not modified, given that it was not possible to access patient height values and AF, being the ICRP reference phantom, represents quite well the average female.

4.6.3 Matching the Lungs Dimension

After adapting AF's voxel resolution and, consequently, overall size to the patient, the phantom underwent a procedure to modify its lung dimensions. Firstly, the platform ImageJ was used to measure the maximum dimensions of the lungs in the topograms for each patient in the x, y and z direction. Given that the right and left lungs are different organs and have different organ IDs, ReDimLungs needs to be run separately for each lung. The procedure, performed using the ReDimLungs program, was replicated twelve times, for each lung in all six patients. AF's lung dimensions will be referred as AFx, AFy and AFz. In any direction (x, y or z), the phantom's lung size was considered to be a satisfactory approximation if the phantom's lung size approximates the patient's lung with an error smaller or equal to 0.5cm. This error value seemed to provide a good compromise between accuracy of the lung approximation and the good practice of not adding or deleting too many layers in any direction with ReDimLungs.

Using ReDimLungs, this procedure should be performed separately for each dimension and, for this reason, it was decided that the first dimension to be analyzed would be z, followed by x and the last one would be y.

Firstly, for the z dimension, the lung sizes in z for the phantom (AFz) and for the patient (Pz) are compared:

- If $|Pz–AFz| \leq 0.5$, then proceed to the next dimension;
- If $|Pz–AFz| > 0.5$, then the lung needs to be scaled and two situations may occur:

  - If Pz > AFz, then voxel layers need to be added to the lung;
  - If Pz < AFz, then voxel layers need to be deleted from the lung.

The number of layers to add/delete can usually be roughly calculated by dividing the difference between the patient's and the phantom's lung size in z by the voxel resolution in z. However, this is not always the case. The number of layers to add/delete depends on many aspects and, thus, the user should perform a trial and error method, which is schematically presented in Figure 4.4. The user should add one line to the tasks file at a time, run ReDimLungs and check the program's output for lung size in z. Two situations may occur:

- If |Pz–AFz| $\leq$ 0.5, then the lung scaling is finished in the z dimension;
- If |Pz–AFz| > 0.5, then another line should be added to the tasks file, run ReDimLungs and check the program's output for lung size in z again.

Lines should be added to the tasks file adding/deleting layers of voxel alternating between the positive and negative side of the z axis (as is illustrated in Figure 4.4). The concepts of positive side and the negative side of the axis are clarified in Figure 4.3.

The process for the next dimensions to consider (x and y) is analogous to the one described for the z dimension. However, since the scaling of the organ in one dimension may affect the other dimensions, the last organ dimensions reported by ReDimLungs are the new values for AFx, AFy and AFz.

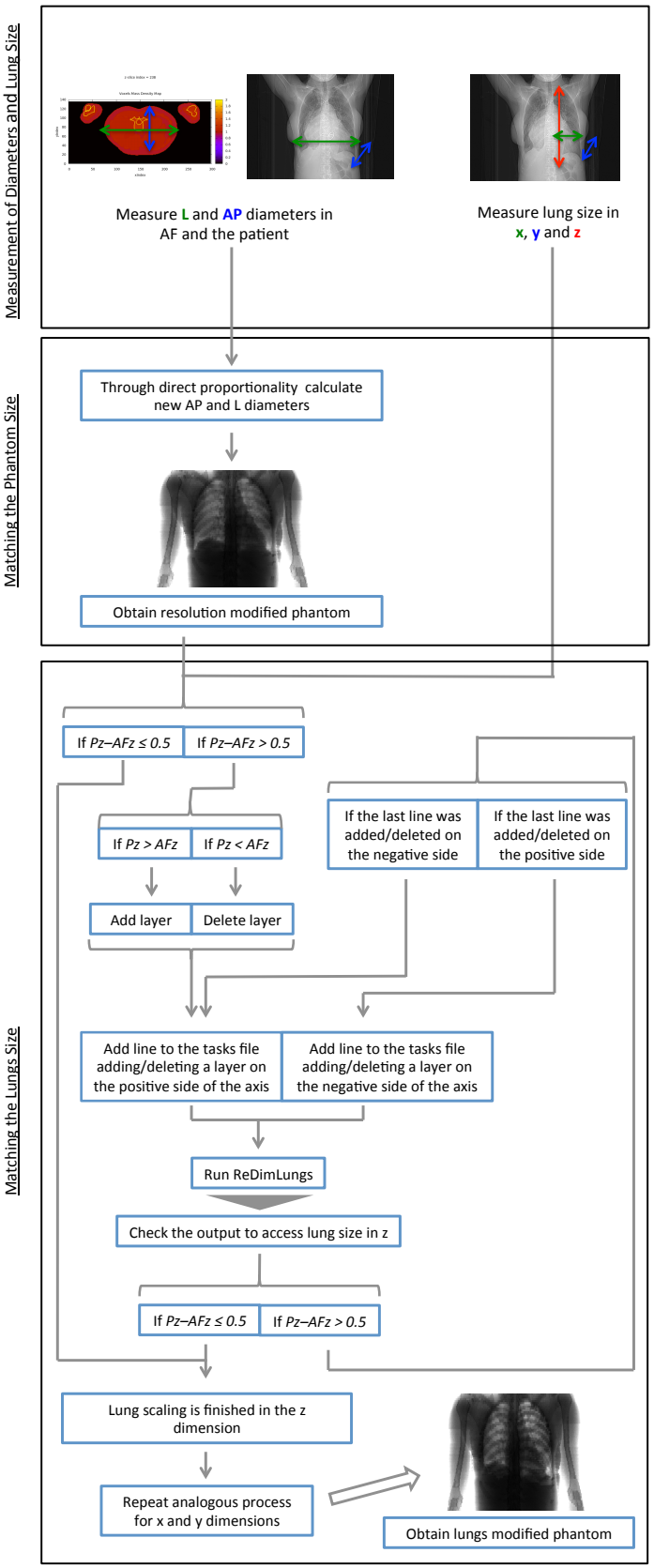

Figure 4.4: Workflow diagram of the patient/phantom matching procedure. In this diagram, AFz and Pz correspond to AF's and the patient's lung dimension along the z axis, respectively.

Chapter 5

The Monte Carlo Method

Since Monte Carlo methods represent a significant component of this thesis, Chapter 5 is dedicated to the use of this calculation technique. Firstly, the basic concepts of MC calculations are described, along with a brief history of the methods. The MC simulation packages PENELOPE and PenEasy are described next, followed by a brief explanation of the PenEasy input file, as well as the tallies specifically used in this thesis. A thorough description of the geometry, source, materials and spectrum MC implementation of CTDI measurements is also presented, aiming to access the deposited energy in the IC. Finally in section 5.5, the methodology of implementation of MC simulations in the original and modified voxel phantoms is described.

5.1 MC Fundaments

Monte Carlo methods can be defined as a broad class of computational methods that perform repeated random sampling to obtain numerical results. Monte Carlo has become a tool widely used in fields such as mathematics, finance, physics, etc. [71]. MC methods, as well as the associated software, were first applied to radiation transport physics during nuclear weapons research at the Los Alamos National Laboratory during World War II. Nowadays, Monte Carlo techniques are commonly used in physics to model the interactions between ionizing radiation and matter. When coupled with computational phantoms, MC methods allow for the user to reproduce and better understand the behavior of several particles (i.e., photons, electrons, neutrons, etc.) inside the human body. This application is especially useful in health physics [40].

The MC technique generates random input numbers, which are then applied to probability functions reflecting particle interactions with the crossing medium, in order to

predict the particle's track. The track (or history) of a particle is then just a random sequence of free flights separated by interaction events, each having a specific probability function. When an interaction event occurs, the particle may loose energy, change its direction or be absorbed and produce secondary particles. Each history is considered terminated when a particle either is absorbed in an interaction event or its energy declines to a value beneath a pre-defined threshold [71].

MC's inherent statistical uncertainties can be controlled to be very low, at the expense of the simulation of a higher number of histories and greater computational effort. Over the last decades the advent in computational power and the improvement in computer affordability allowed straightforward everyday and widespread application of MC methods. Several major Monte Carlo packages were then developed by universities, national laboratories and the user community. Some of the MC packages widely used for radiation physics purposes are PENELOPE [71], FLUKA [72], GEANT4 [73], MCNP [74] and EGSnrc [75]. Despite the wide use and implementation of MC methods, measuring with physical phantoms is usually still needed to validate the MC model. In this dissertation MC methods were implemented using the PENELOPE code package.

5.2 PENELOPE

PENELOPE (PENetration and Energy Loss of Positrons and Electrons) is a free and open source MC simulation package largely written in FORTRAN 77. PENELOPE performs MC calculations of radiation transport in complex geometries, which may consist of a wide variety of materials, for electrons, photons and positrons ranging from 50eV to 1GeV. PENELOPE is a subroutine package, which means that PENELOPE cannot run by itself, but instead operates using a set of sub-routines and a steering main program, provided by the user, to control the geometry and the evolution of tracks. PENELOPE provides some main programs, such as pencyl, which deals with multi-layered cylindrical geometries, and penmain, for generic quadratic geometries. The PENELOPE code package is organized in six files containing subroutines:

- penelope.f: consists on subroutines for simulation of radiation transport in homogenous materials;
- pengeom.f: contains subroutines for tracking particles between modular quadratic geometries;
- penvared.f: contains subroutines that apply basic variance-reduction methods;
- rita.f: contains subroutines for sampling of random numbers;
- material.f: program for creating material files;
- timer.f: program for measurement of simulation time [71].

5.3 PenEasy

PenEasy (version 2015-05-30 compatible with PENELOPE 2014) is a general-purpose PENELOPE main program package mainly coded in FORTRAN 95, which uses some of the PENELOPE subroutines and adds a few of its own, organized in several files, such as:

- penEeasy.F: the source code;
- penaux.F: includes various subroutines that help running penEasy;
- penvox.F: geometry package that handles particle transport in a geometry that combines quadratic surfaces and voxels;
- penvr.F: implements variance-reduction techniques for PenEasy;
- timing.F: contains subroutines associated with simulated time updated to FORTRAN 95;
- tally*.F: several files that contain the subroutines necessary to implement each PenEasy tally.

PenEasy was chosen due to its ability to overlap quadratic and voxel geometries and it has specific tallies for energy deposition in each material and for simulated image creation. The operation of PenEasy is based on an input file and an output file. The PenEasy input file is where the user inputs several quantities related to the simulation and calls files, such as the quadratic and voxels geometry files, and consists of several sections. The sections used in this work are described in the following list:

- **SECTION CONFIG:** This section defines the general settings of the simulation, such as the number of histories to simulate or the available time for the simulation.
- **SECTION SOURCE BOX ISOTROPIC GAUSS SPECTRUM:** This section deals with the definition of the particle beam. PenEasy uses a fairly flexible source model, allowing the definition of the type of particle, the box center coordinates and box sides in x, y and z, direction and shape of the particle beam and spectral energy.
- **SECTION PENGEOM+PENVOX:** As aforementioned, PenEasy deals with quadratic geometries, voxelized geometries or a combination of the two. The quadratic geometry is defined in a *.geo file in the form of various surfaces delimiting homogenous bodies. The voxelized geometry is usually described in a file with the *.vox extension, which contains information about the material and density of each voxel.
- **SECTION PENELOPE:** Through the PENELOPE file material.f, the user creates material files that are listed and identified by number in this section. Each line corresponds to one defined material file (with the *.mat extension) and contains a set of transport parameters characterizing particle transport in the material:

  - **EABS(e-), EABS(ph) and EABS(e+):** Cutoff energy for electrons, photons and positrons, respectively. When the energy of a particle reaches this value, it is considered absorbed (the program no longer tracks its history);
  - **C1 and C2:** parameters related to elastic scattering;
  - **WCC and WCR:** cutoff energy for inelastic collisions of charged particles and for *bremsstrahlung* emission, respectively;
  - **DSMAX:** maximum allowed flight length for electrons and positrons.

- **TALLY SECTIONS:** The PenEasy input file provides the possibility to use various tally sections.

The PenEasy output file provides a report of the entire simulation, containing information about how PenEasy read the input file and about the simulation itself, such as the number of simulated particles and simulation speed. For each tally the results are presented in a separate file with the tally name and the *.dat extension. The PenEasy tallies used during the elaboration of this dissertation were:

Energy Deposition Tally:

The Energy Deposition tally reports the energy deposited in each material defined in SECTION PENELOPE, along with its uncertainty, which corresponds to two standard deviations. The tally results are presented in units of electron-volt per history ($eVhist^{-1}$). Since absorbed dose values in CT are usually reported in mGy, it is necessary to convert the tally units. An electron volt is defined as the amount of energy an electron gains (or looses) when moving through a potential difference of 1 volt and corresponds to $1.602\,\mathrm{x}\,10^{-19}$J. The definition of Gray was presented in section 2.4.2. Consequently, the tally value can be converted to absorbed dose in mGy through the next equation, where M_{mat} and N are the mass in a given material in kilograms and the number of particles simulated, respectively:

$$D(absorbed\,dose) = \frac{tally\,value\ \mathrm{x}\ 1.602\,\mathrm{x}\,10^{-19}}{M_{mat}}\,\mathrm{x}\,N\,\mathrm{x}\,10^{-3} \quad [\mathrm{mGy}] \tag{5.1}$$

Pixelated Imaging Detector Tally:

The Pixelated Imaging Detector Tally creates an image of the simulated geometry. For the proper implementation of this tally some parameters need to be set in the correspondent tally section. Firstly, the body number of the detector defined in the geometry file needs to be defined, such as the geometry and material of the detector, detection mode (i.e. energy integrating, photon counting) and the type of radiation to be detected (i.e. only primary phantoms, scattered phantoms, etc.) [68].

5.4 Implementation of CTDI Measurements

In order to validate the MC model, the measurements carried out in the CT equipment were implemented using the PenEasy code package and MC absorbed dose calculations in the active IC volume were performed.

5.4.1 Geometry and Source Definition

The implemented IC and phantom were the ones described in sections 4.1.2. and 4.1.3., respectively. In order to reduce computational time, the geometry was simplified. The phantom was modeled as a cylinder with 16cm base radius and 14.5cm long. For the IC, only the sensitive volume was simulated, which was modeled as a cylinder with a base radius equal to 0.309cm and 10cm long. The geometrical setup is displayed in Figure 5.1. The patient table was not included in the geometry, due to the difficulty in obtaining information about it. An outer sphere with 4.5m radius was defined around the phantom to represent an outer system for the simulation to run in.

Given the symmetrical irradiation setup, the chamber was only simulated in the center, 0º and 90º orifices, with the dose value with the IC at 180º and 270º orifices being considered equal to the value with the IC at 0º and 90º, respectively.

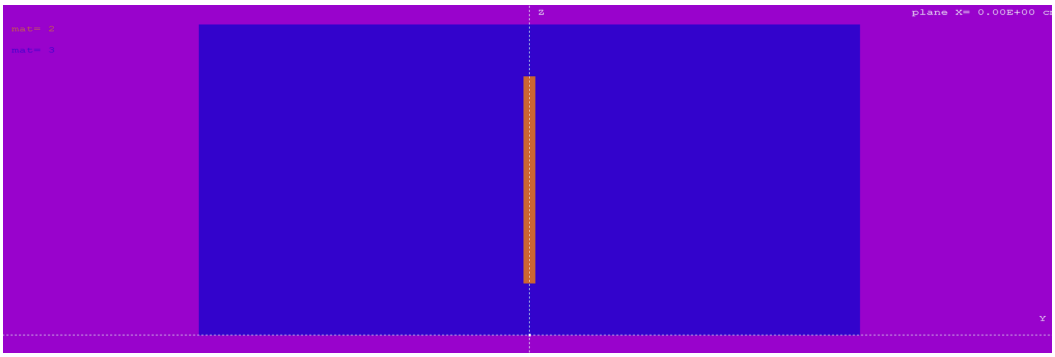

Figure 5.1: Representation, using the quadratic geometry viewing program gview2d [71], of a cross section of the phantom passing trough the x=0 plane for the situation of the chamber at the center of the phantom. The IC's sensitive volume, the phantom and the outer sphere are represented in orange, blue and purple, respectively.

The beam used by the CT scan was a rectangular beam 5mm thick. Since PenEasy does not allow the simple definition of a rectangular beam, the beam was modeled using a box source (instead of punctual source), composed by several very thin cone beams. Using ImageJ, the image profile of the simulated beam (which resembled a Gaussian curve) was obtained and a 5mm thickness was achieved through full width at half maximum (FWHM) estimation.

In order to model a 360º rotation of the gantry during a CT examination, simulations should be performed for various angles ranging from 0º to 360º. Nevertheless, in order to minimize simulation time, simulations were only performed for source angles ranging

from 0º to 360º in 90º intervals (0º, 90º, 180º and 270º) for every considered chamber position inside the phantom. A 36-point interpolation was then applied to the values of deposited energy for every simulated source position using the statistical analysis software Origin [76].

5.4.2 Materials Definition

The material files necessary to run the MC simulations were obtained using the PENELOPE package material database, through the material.f program. Table 5.1. describes all the materials listed in the PENELOPE section of the input file.

Table 5.1: Material list present at the PENELOPE section of the PenEasy input file.

Material #	**Material Name**	**Density** ($g\ cm^{-3}$)	**Geometry Component**
1	Air	0.120479×10^{-3}	Outer Sphere
2	Air	0.120479×10^{-3}	IC's Sensitive Volume
3	PMMA	1.19	PMMA Phantom

The tally energy deposition allows the calculation of the energy deposited in each material defined in the PENELOPE section of the input file. Thus, to prevent the misinterpretation of the results, a different material file needs to be created for every geometry component whose deposited energy value is of interest.

5.4.3 Spectrum Definition

The photon energy spectrum was created by a program developed at the Institute of Physics and Engineering in Medicine, using a catalog of diagnostic x-ray spectra [77]. The spectrum, represented in Figure 5.2, was generated using the following parameters:

- Peak voltage: 120kV;
- Anode material: Tungsten;
- Anode angle: 12º;
- Filter material and thickness: Aluminium, 2.5cm;
- Distance isocenter-source: 54.1cm.

The peak voltage and distance value was the same used when performing the measurements in the hospital. However, given the difficulty in accessing the other parameters for the CT scan in question, the values were the same used in previous work [78], [79].

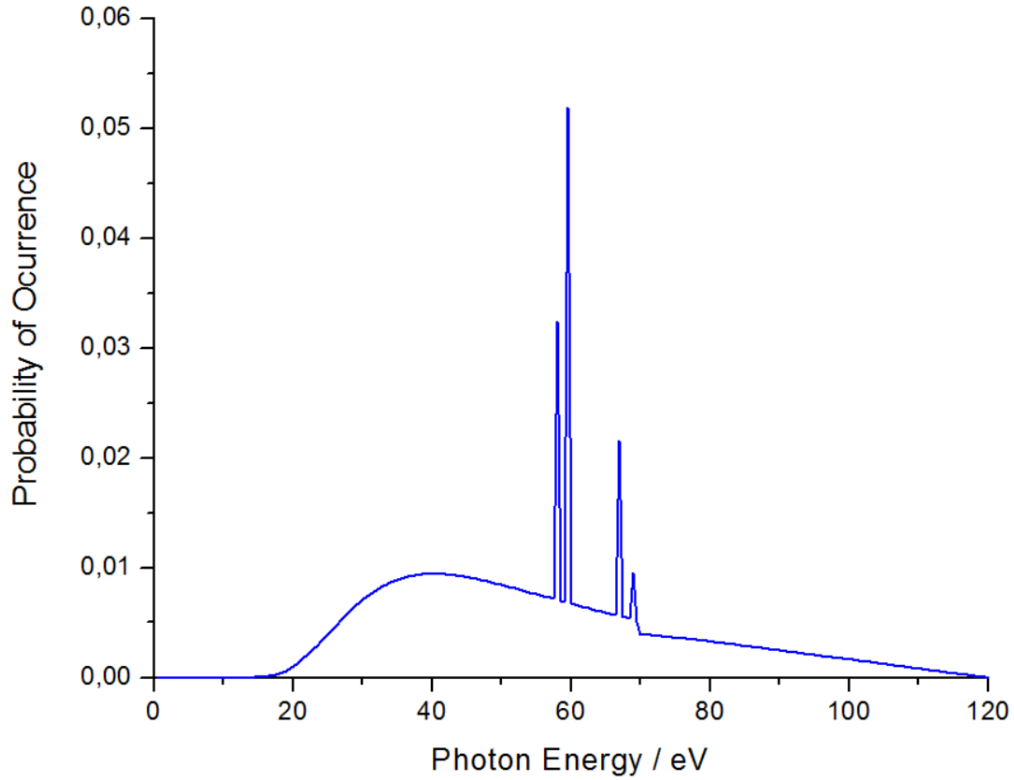

Figure 5.2: Graph of the x-ray spectrum used in the MC simulations.

5.5 Implementation of Scaled Phantoms MC Simulations

Using the PenEasy code package, MC simulations were performed on the original AF phantom, phantoms with the voxel x and y resolution scaled and lungs scaled with the ReDimLungs program for each patient image. The resolution in z was not modified.

5.5.1 Geometry, Source and Materials Definition

The definition of the geometry and the source was implemented analogously to the conditions of the CT scans represented in the available patient images. Since the phantoms used all had different sizes, the geometry and source definition were always performed regarding the geometrical center for all phantoms, defined as the geometrical center of the slice at the sternal furcula height (138.908cm). In the quadratic geometry, only the 4.5m radius outer sphere and the detector were modeled. The detector was constructed as a cuboid (in PenEasy through the definition of 6 planes) and was only used on simulations run to obtain the phantom's image. The patient images include some parameters associated with the used protocol, also used to build the MC model, such as:

- Spectrum: 120kV peak voltage;
- Distance Source-patient (mm): 541;
- Distance Source-detector (mm): 949.147;

- Distance Patient/Phantom-detector (mm): 408.14;
- Image/Detector Size (mm): 530x360.55;
- Image/Detector Size (pixels): 888x661;
- Detector Thickness (mm): 2.5.

Despite the CT scanner using a beam with a rectangular shape, the radiation source was modeled as punctual with cone beam shape at the initial position, without accounting for the rotation of the gantry. This work aimed to access deposited energy values, as well as the detector image, and no absolute dose values were reported (dose values were always reported relative to the AF phantom).

The source was located at the front of the phantom, at the phantom's geometrical center in x and at the approximate height of the sternal furcula in z. The y coordinate varied according to the characteristics of the simulation performed. If the simulation was performed using the tally energy deposited to calculate dose values, the source's y coordinate would be 54.1cm away from the phantom's geometrical center to better replicate the original CT scan characteristics. If the simulation was performed using the tally pixelated image detector to obtain the phantom's image, through a trial and error process, 254.1cm was found to be a source-phantom distance that allowed satisfactory visualization of the phantom's region of interest. The source was represented by a complete cone beam with azimuthal angle varying from 0º to 360º. Regarding the polar angle, the minimum angle necessary to cover the entire region of interest was estimated through a trial and error method to minimize simulation time. The polar angle was set from 0º to 25º for the dose simulations 0º to 8º for the image simulations.

The spectrum used was the one described in section 5.4.3., since the peak voltage was the same as the one present in the patient CT images.

The material density and chemical information necessary to run the MC simulations using AF were acquired from ICRP Publication 110 [46]. Since all materials in which deposited energy is of interest need to be listed in the input file, the organ list provided with AF was modified and the program ReadPhantom was run using the updated list to render the simulation file. Lists of the materials and of AF's organs that needed to be modified in order to perform the simulations are presented in Appendix A: Lists of Materials and Organs Used in Voxel Phantom Simulations.

5.5.2 Dose vs Voxel Volume Simulations

With the objective of analyzing the variation of organ dose values when AF's voxel resolution is modified, a set of simulations was performed to obtain three trend graphics. For the first trend, designed as TRENDXY, MC simulations to access deposited energy value were performed in eleven phantoms, including the original AF, with both x and y voxel resolution ranging from 0.1275 to 0.2275cm in intervals of 0.01cm. The second

and third trends, TRENDX and TRENDY, were performed similarly to the first trend. In TRENDX only the x resolution was modified (y resolution constant) and in TRENDY only the y resolution was modified (x resolution constant).

Deposited energy values were retrieved for all simulations via the tally energy deposited for the right lung and left lung, given that the lungs were the focus organ of this work. The deposited energy was also calculated for two other organs, the stomach and the esophagous, since they are situated in the thorax area and are prone to developing mutations from exposition to environmental factors, such as ionizing radiation [80]. The deposited energy values were then converted to dose values and the quotient between organ dose to the modified phantom and to the original AF phantom was calculated for all eleven phantoms in every trend. The trends were performed essentially with two objectives:

- Establish a correlation between voxel volume and organ dose;
- Analyze the argument that only scaling the voxel resolution in the direction of the irradiation has a relevant effect on organ dose [53].

5.5.3 Scaled Lungs Phantom Simulations

Using the PenEasy code package, MC simulations were performed on:

- The original AF phantom;
- Six phantoms with the voxel x and y resolution scaled to each patient L and AP diameters, henceforth referred to as the resolution phantoms: AF1res, AF2res, AF3res, AF4res, AF5res and AF6res;
- Six phantoms with the voxel x and y resolution scaled to each patient L and AP diameters and lungs scaled with the ReDimLungs program for each patient lung sizes, henceforth referred to as the patient phantoms: AF1, AF2, AF3, AF4, AF5 and AF6.

Overall, three MC simulations were performed for each of thirteen phantoms. In particular, one simulation was performed to obtain the energy deposited in organs and two simulations were performed to generate the images, one in AP position and another in L position.

Organ dose values, calculated from energy deposited values, were accessed for six organs of interest: right lung, left lung, right lung blood, left lung blood, stomach and esophagous. For each interest organ of interest the following ratios were calculated:

- Organ dose of the resolution phantoms over the AF ones;
- Organ dose of the patient phantoms over the AF ones.

Chapter 6

Results and Discussion

This chapter is intended to report the most relevant results obtained during the course of this work. First, the CTDI validation measurements are presented, followed by the computational results. The results, as well as a discussion, of the trends performed by varying the voxel resolution of the female ICRP reference phantom are also present. The results related with the patient/phantom matching procedure are also reported here, as well as an analysis on the variation of organ doses in the modified phantoms and a visual comparison between the patient/phantom images for cross-checking purposes.

6.1 MC Model Validation

The CTDI measurements for the IC inside every orifice in the PMMA phantom are presented in table 6.1. The standard deviation value, calculated using equation 4.1, was 0.0335 or lower for all orifices.

In Table 6.1 the measured CTDI values are reported. As expected, the 180º periphery dose value in the phantom used was smaller than the other periphery values due to patient table attenuation, and in average the periphery results were about two times the center value. The IC free-in-air measurement was converted into $CTDI_{100}$ value using equation 4.2, yielding a 31.12 mGy.

Table 6.2 represents the tally dose, $CTDI_{100}$ and $CTDI_W$ values simulated, as well as the relative difference between measured and simulated results. The $CTDI_{100,measured}$ values for 180º and 360º were not simulated due to symmetry setup (they were considered equal to the values at 0º and 90º, respectively).

Table 6.1: Dose, $CTDI_{100}$ and $CTDI_W$ values measured for the ionization chamber inserted in each orifice of the PMMA phantom.

Orifice (mGy)	**Dose** (mGy)	**Dose Average** (mGy)	**CTDI$_{100}$** (mGy)	**CTDI$_W$** (mGy)
center	0.3426 0.3427 0.3456	0.3436	6.8727	
0º	0.7372 0.7464 0.7994	0.7611	15.2220	
90º	0.7527 0.7486 0.7569	0.7527	15.0547	11.7693
180º	0.6220 0.6105 0.6077	0.6134	12.2680	
270º	0.7123 0.7140 0.7226	0.7163	14.3260	

Table 6.2: Dose, respective uncertainty and CTDI$_{100}$ and CTDI$_W$ simulated values, as well as the relative difference, represented as RD, between measured and simulated values, for every ionization chamber location. Due to symmetry setup, Dose results for 180º and 270º were not simulated, and so are marked as NS.

Orifice	**Dose** (eV(hist g)$^{-1}$)	**Uncert.** (%)	**CTDI$_{100}$ simul.** (mGy)	**CTDI$_{100}$ RD** (%)	**CTDI$_W$** (mGy)	**CTDI$_W$ RD** (%)
center	36.1989	3.4	4.1699	39.33		
0º	135.3191	4.0	15.5878	2.40		
90º	129.9313	4.2	14.9672	0.58	11.5749	1.65
180º	NS	NS	15.5878	27.06		
270º	NS	NS	14.9672	4.48		

In general, the measured results agree with the simulated ones rather well, particularly the periphery values of the phantom and the $CTDI_W$, all having relative differences of about 4.5% or lower. The relative differences for the chamber located at the center and at 180º are about 39% and 27%, respectively. However, a significant uncertainty can arise from the lack of MC implementation of certain elements present in the CT equipment, such as the patient table (for the case of the chamber location at 180º) and bowtie filter, between others. In addition, the simulated beam shape was based on an approximation and so the collimator was not implemented. The implementation of bowtie filters, collimators and the patient table can be complex and time-consuming. Moreover, detailed information about these elements can be quite difficult to obtain from manufacturers [78].

Since the $CTDI_W$ relative difference is approximately 1.6%, it is possible to conclude that the implemented computational model is a fairly reliable reproduction of the clinical CT equipment.

6.2 Dose vs Voxel Volume Results

The trend MC simulations were implemented to study the variation of organ dose values when AF's voxel resolution is modified, with two main objectives:

- Establish a correlation between voxel volume and organ dose;
- Analyze the argument that only scaling the voxel resolution in the direction of the irradiation has a relevant effect on organ dose [53].

In the three trends, the energy deposited values were retrieved for each simulation for four organs: right lung, left lung, stomach and esophagous. The calculation of organ dose for any organ was performed using the following procedure:

1. Assume the dose in an organ in the original AF phantom is 5mGy;
2. Convert the dose to number of particles using equation 5.1. The organ mass used is the AF original. Since we want to study the dose variation in two anthropomorphic phantoms, the same tube current needs to be used, which translates into the same number of particles. The number of particles is then used again in equation 5.1 to calculate dose. The organ mass used is of the modified phantom.
3. The voxel mass can be calculated by multiplying voxel volume by the material density. The organ mass is determined as the number of voxels in the organ multiplied by voxel mass. The quotients between organ dose to the modified phantom and to the original AF phantom, calculated for all eleven phantoms in every trend, are displayed on Figures 6.1 and 6.2.

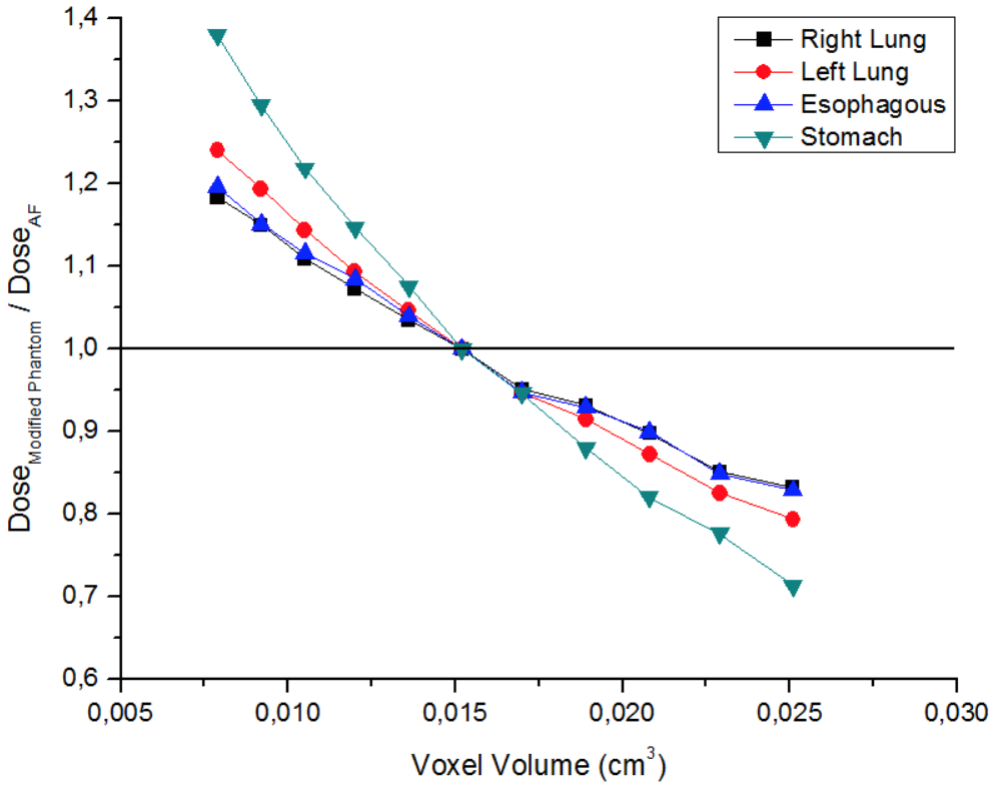

Figure 6.1: Graph for TRENDXY. Ratio between organ dose in the modified phantom and in the AF phantom for the right lung, left lung, esophagous and stomach for the phantoms considered. The horizontal black line at 1.0 represents the case of the dose being equal to the AF. The statistical uncertainty was lower than 1% for all organ dose values.

In Figures 6.1 and 6.2, it is possible to observe that organ dose varies significantly with voxel volume, showing a clear tendency for the organ dose to drop as voxel volume grows. Since the organ mass grows with the total organ volume, lowering absorbed dose, this tendency was expected. This tendency was also observed in other works, such as the work performed by Caon et al. [54]. In TRENDXY (Figure 6.1), modifying the voxel size in x and y the effect in organ dose is quite significant, varying from about 0.7 to 1.4 times the dose in AF. The graph from TRENDX (Figure 6.2a) shows a small organ dose variation (only ranging from approximately 0.9 to 1.06 times the dose in AF) when changing the voxel size in the x dimension. However, TRENDY (Figure 6.2b), in which the voxel size was only modified in y (the direction of the irradiation) shows a behavior very similar to TRENDXY, also ranging from about 0.7 to 1.4 times dose in the AF phantom. It is then possible to conclude that only modifying the voxel dimension in the direction of the irradiation has a significant effect on organ dose, result also reported by Veit et al. [53].

It is also important to point out that in TRENDX, when altering the voxel size only in the x dimension, the organ dose grows with voxel volume. This happens for the right lung, left lung and esophagous, in contrast to the behavior of these organs in the other

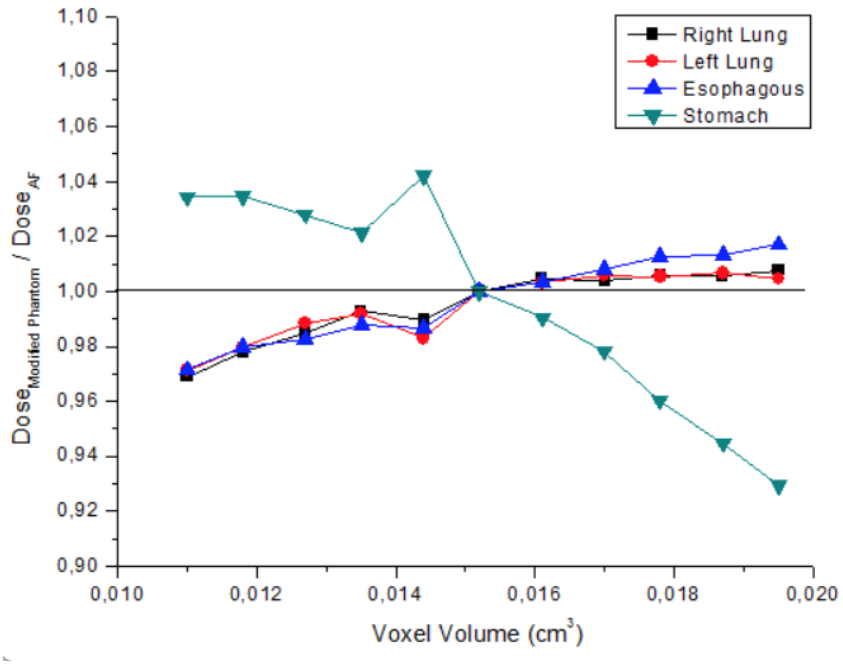

a)

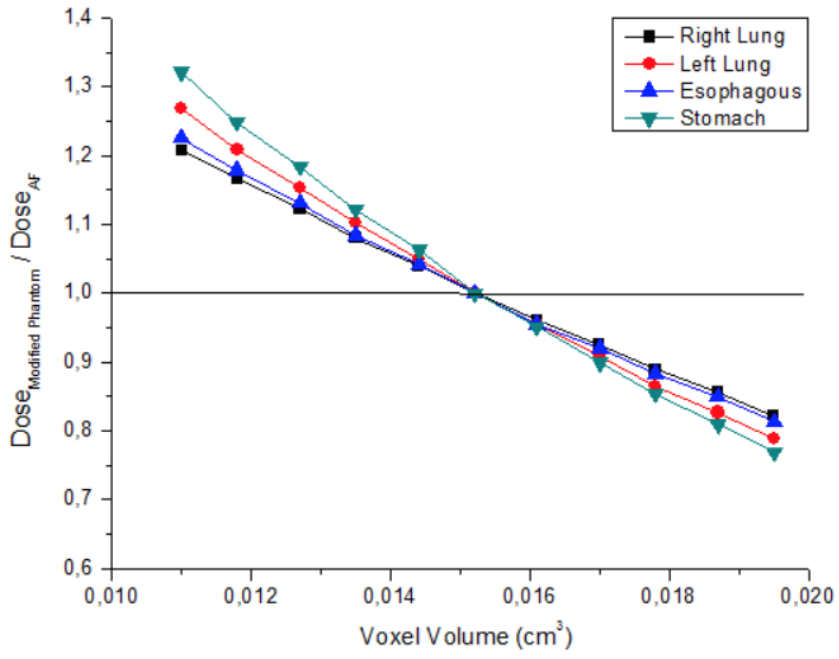

b)

Figure 6.2: **a)** Graph for TRENDX. Ratio between organ dose in the modified phantom and in the AF phantom for the right lung, left lung, esophagous and stomach for the phantoms considered. The uncertainty was controlled do be lower than 1% for all organ dose values. **b)** Graph for TRENDY. Ratio between organ dose in the modified phantom and in the AF phantom for the right lung, left lung, esophagous and stomach for the phantoms considered. The statistical uncertainty was lower than 1% for all organ dose values.

trends. This behavior in TRENDX may be explained by the phantom's size being modified only in the x direction and, consequently, more surface anatomy is irradiated. Hence, the deposited energy value will grow, along with the dose value. The lungs and esophagous are organs located relatively closer to the surface with respect to the stomach, in which the organ dose drops as voxel volume grows.

Considering all three trends, is also possible to perceive that the effect of voxel volume on dose can be different for different organs, also reported by Veit et al. [53], as exemplified by the stomach trends. The stomach lines may stand farther away from the other lines (Figure 6.1 and 6.2b) or even depict a different behavior than the rest of the organs considered (Figure 6.2a).

6.3 Results from Patient/Phantom Matching Procedure

6.3.1 AF Size Measurement

Using the Gnuplot tool, AF was visualized and its L and AP diameters were measured 23cm below the sternal furcula, at slice 238, represented in Figure 6.3. The values acquired for the L and AP diameters were 154 and 109 voxels, values that can be multiplied by the resolution in x and y, to yield 27.335cm and 19.3475cm, respectively.

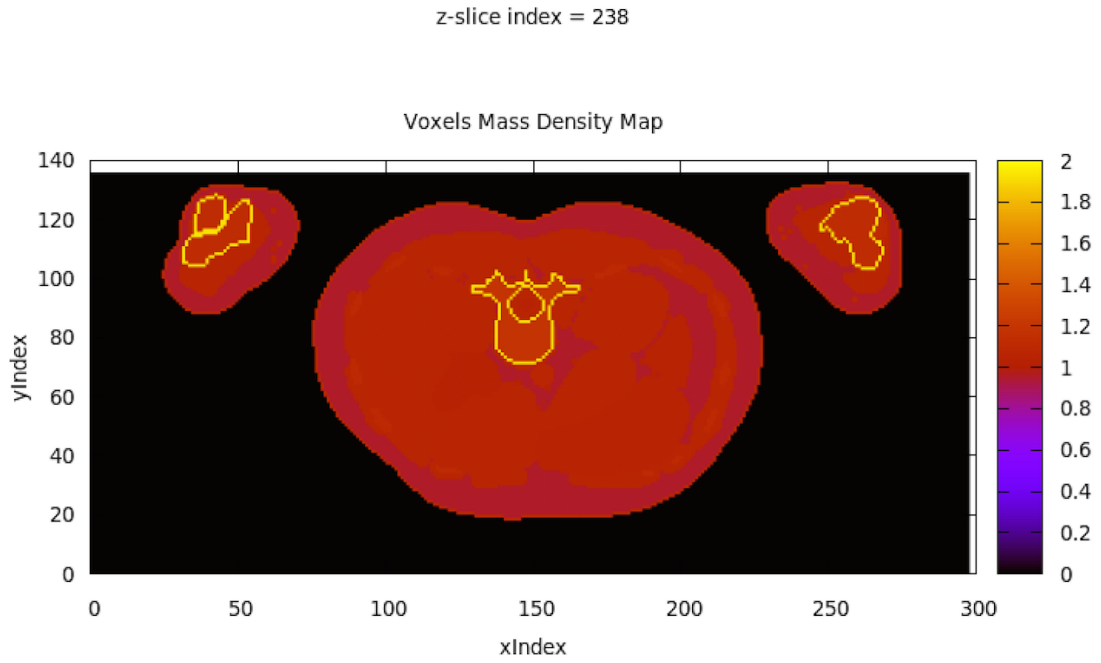

Figure 6.3: Visualization, using the Gnuplot tool, of AF's slice 238.

6.3.2 Patient and Phantom Size Measurement

This section presents the results associated with the measurements performed on the patient and phantom images described in section 4.6.

The L and AP diameters were measured using ImageJ in the patient CT images, which were then compared with the ones measured in the simulated images of the resolution phantoms. Simulations were performed on the resolution phantoms to access phantom image with the source at 0º and 90º. However, the phantoms were magnified in images obtained through the tally pixelated imaging detector. So the Magnification Factor (MF) was calculated as the quotient between the measured diameter (in Gnuplot) of AF and the simulated diameter of AF (equations 6.1 and 6.2).

$$MF_x = \frac{L_{AF,\,measured}}{L_{AF,\,simulated}} = 0.876 \tag{6.1}$$

$$MF_y = \frac{AP_{AF,\,measured}}{AP_{AF,\,simulated}} = 0.802 \tag{6.2}$$

The diameters measured in the simulated images were multiplied by MF in x and y to render the L and AP diameters of the resolution phantoms. The relative differences between L and AP diameters measured in the patient CT images and simulated for all resolution phantoms were calculated. Table 6.3 shows the results from the L and AP diameter measurements, as well as average values for the diameters. The average patient L and AP diameters were approximately 28.2 and 21.9cm, which, when compared with AF's diameters, represent a relative difference of 3.1% and 2.6%, respectively. These results show that the AF phantom diameters are fairly close to the average of the patient sample considered in this work.

The measurements were performed in number of pixels. Since the pixel size was the same for the patient CT images and for the simulated images, the uncertainty of the diameter measurements for all images was 0.05968cm, which corresponds to an uncertainty under about 0.5% for all images. Nevertheless, the simulated images also suffered from MC statistical uncertainty, which was under 5% for all images, totaling an uncertainty of approximately 5.5% for measurements on the simulated images.

The resolution phantoms, as well as the patient phantoms, were organized from 1 to 6 with ascending voxel volume.

The patient's lungs were measured in the patients CT images in the x, y and z direction. The right lung was particularly difficult to measure in x, due to its superposition with the left lung on its left extremity, so the right lung's size in x is underestimated in all patient CT image measurements. The lung dimensions of the resolution phantoms were derived from the ICRP Publication 110's listings of the rectangular prism (box) containing each organ (minimum/maximum columns, rows, and slices occupied by each organ/tissue). The procedure described in section 4.6.3. was performed to scale the lungs, providing the patient phantom's sizes in x, y and z used for each lung. The relative differences between lung sizes in the patient CT images and in the patient phantoms were calculated. The results are presented in Appendix C.

Table 6.3: L and AP diameters measured in the patients' CT images and in the simulated images of the resolution phantoms (after multiplying by MF), as well as the relative difference between them. The average values were calculated using patient 1 through 6 values, not accounting for AF values. The presented Simulated Diameters for AF were used in the calculation of the MF.

Patient #	**CT Image Diam.** (cm)		**Simulated Diam.** (cm)		**Diameters RD** (%)	
	L	AP	L	AP	L	AP
AF	27.335	19.347	31.213	24.111	-	-
1	24.640	18.282	24.721	18.246	0.20	0.33
2	25.938	20.619	25.924	20.544	0.36	0.06
3	27.940	20.940	27.387	21.071	0.63	1.98
4	29.201	21.858	29.268	22.029	0.78	0.23
5	31.119	23.759	31.098	23.945	0.78	0.07
6	30.279	26.477	30.314	26.818	1.29	0.11
Average	28.186	21.989	28.1190	22.1091	0.46	0.67

The average patient lung sizes in x, y and z for the left and right lung were approximately 10.6, 17.6 and 21.8cm and 11.12, 17.75 and 21.83cm, respectively. When compared with AF's phantom lung sizes, these values represent a relative difference of 3.9%, 27.2% and 0.2%, and 44.6%, 25% and 7.4% in x, y and z for the left and right lung, respectively. These results show the great variability that can exist in the lung sizes of different individuals and illustrate how the AF phantom does not accurately represent individual patients.

As previously mentioned, the measurements were performed to the pixel in the patient CT images, so the uncertainty of the lung measurements for all images was 0.05968cm, which corresponds to an uncertainty under about 0.6% for all lung sizes measured in the CT images.

6.3.3 Results from Matching the Patient Size

The patient's size was matched with the phantom by modifying the voxel resolution in x and y (Figure 6.4). The resolution phantoms, as well as the patient phantoms, were organized from AF1res to AF6res with ascending voxel volume.

The average relative differences between L and AP diameters measured in the patient CT images and simulated for all AF#res phantoms were 0.67% and 0.46%, respectively.

MC simulations were performed on the resolution phantoms. Dose values for the interest organs in each phantom were calculated through the process described in section 6.2. The ratios between dose in each of the modified phantom's organs and in the original AF phantom are presented in Figure 6.5.

In Figure 6.5, as expected, the organ dose values drop for higher voxel volumes. It is

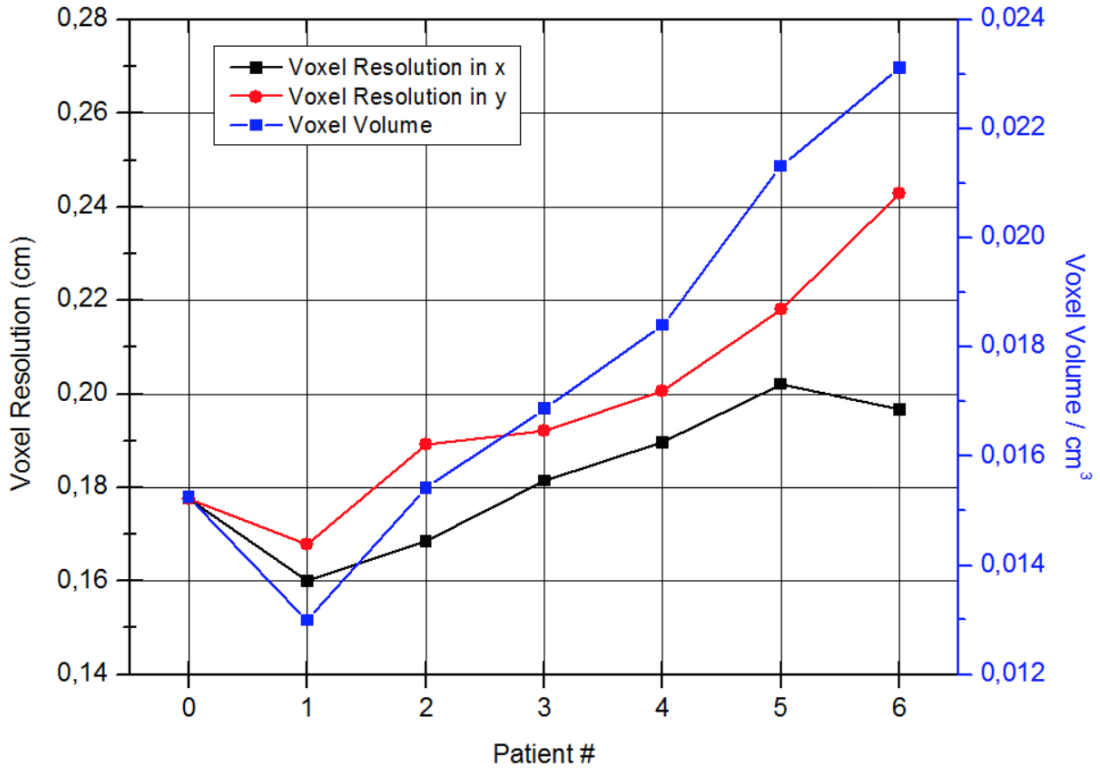

Figure 6.4: Voxel resolution in x and y (on the left y axis) and voxel volume (on the right y axis) for every considered patient. The Patient 0 tag corresponds to the AF phantom.

also possible to observe that, for higher voxel volumes, organ dose values for the same phantom have a tendency to differentiate between each of them (i.e. the right and left lung in patient #6).

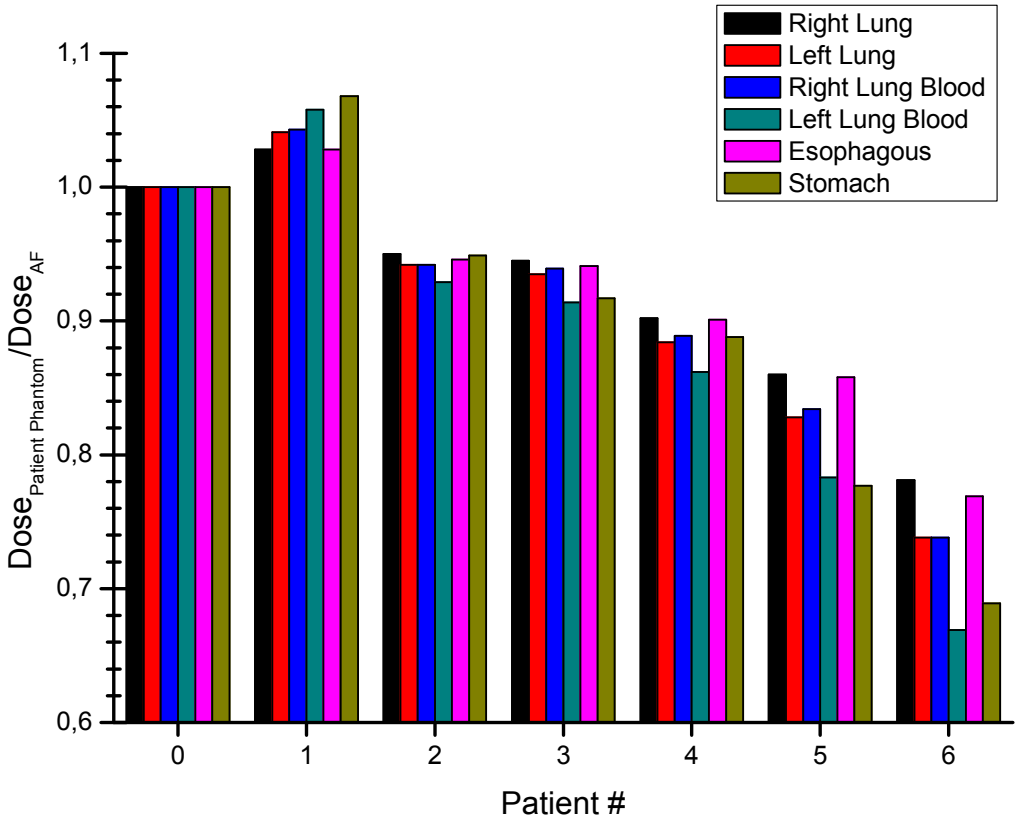

Figure 6.5: Variation of organ dose in relation to the AF phantom for all resolution phantoms. The Patient 0 tag corresponds to the AF phantom. The statistical uncertainty was lower than 1% for all organ dose values.

6.3.4 Results from Matching the Lungs Size

MC simulations were performed on the patient phantoms, where the AF phantom was respectively adapted to each of the 6 CT patient images, according to the L and AP diameters (following the methodology described in 4.6.2) and lungs (following the methodology described in 4.6.3) matching procedures. Dose values for each organ considered in each phantom were calculated through the process described in section 6.2. The ratios between dose in each of the modified phantom's organs and in the original AF phantom are presented in Figure 6.6. The average relative difference between the patients lung sizes retrieved from the CT images and the lung sizes of the patient phantoms was 2.14% and 3.37% for the left and right lungs, respectively.

In figure 6.6, the previously mentioned trend, establishing lower organ dose values for higher voxel volumes, is still present, although it is less evident.

The results depict a fairly significant variance in organ dose for the patient adapted phantoms (from about 0.6 to 1.2 times the original dose). When accessing organ dose values using the AF phantom, the dose is clearly being overestimated for patients bigger

than the reference phantom and underestimated for patients smaller than the reference phantom. Pronounced differences in organ dose can also be noted when comparing Figures 6.5 and 6.6. The modification of the phantoms with the ReDimLungs program has produced greater discrepancy between the organ values in the same phantom, showing that the patient phantoms are more differentiated from AF than the resolution phantoms.

As expected, the right and left lungs, the organs that suffered most modifications during the matching procedure, showed the biggest dose variations from the trend depicted in Figure 6.5 and between patients.

It is noteworthy to remark that the scaling of the lungs can also influence dose in other organs, such as he stomach and the esophagous (which may have been modified during lung scaling). It is then possible to conclude that the scaling of certain organs, such as the lung, can have a significant effect on the radiation dose imparted to an individual during a CT examination.

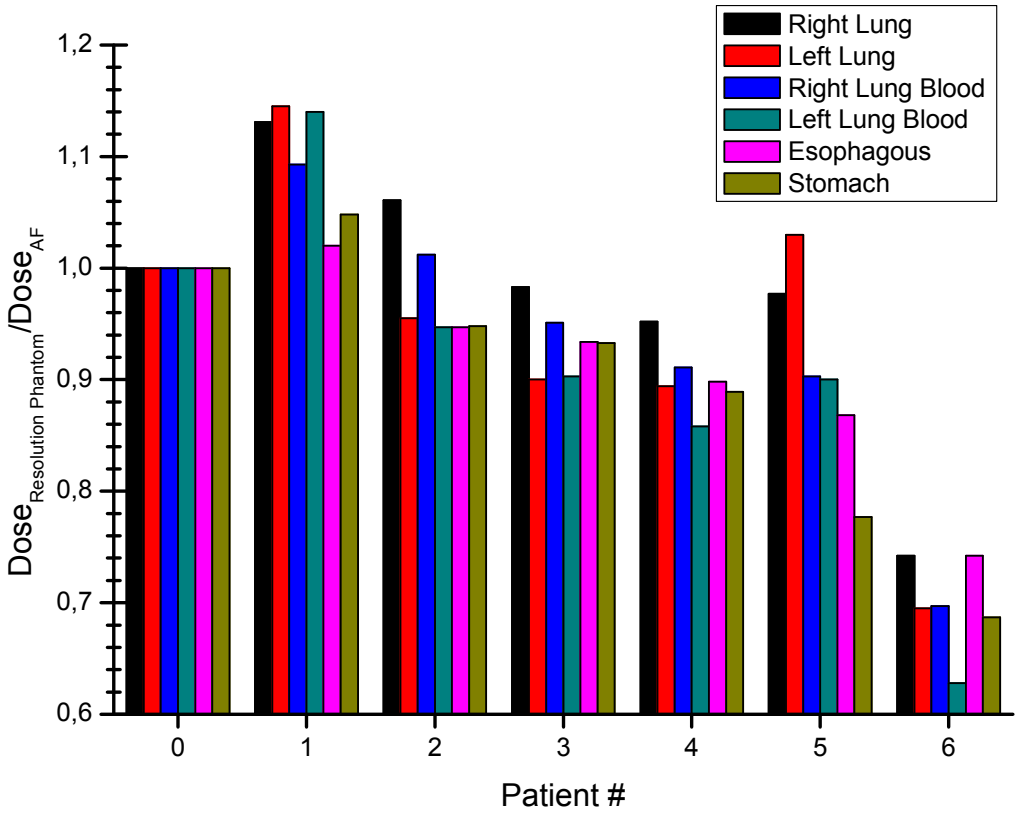

Figure 6.6: Variation of organ dose in relation to the AF phantom for the patient phantoms. The Patient 0 tag corresponds to the AF phantom. The statistical uncertainty was lower than 1% for all organ dose values.

6.3.5 Visual Comparison of Patient and Phantom Images

A visual comparison, represented in Figures 6.7-6.12, was performed for validation purposes between the original CT patient and patient phantoms images. Figure 6.7a shows a MC image of the AF phantom, that was used as phantom model in order to obtain all the modified voxel phantoms showed in Figure 6.7c-6.12b.

When comparing the image of the original AF phantom with the images of the patient phantoms, it is possible to observe variations in the L diameters of the phantoms and also on the size of the lungs.

In general, by comparing the patient CT images with the simulated images, it is possible to perceive that the size and shape of the lungs is similar to the ones depicted in the CT images, particularly for the case of Patient 1, which is an exceptionally small patient with exceptionally large lungs.

It should be stressed that this type of comparison is constrained by the lack of details in the lungs boundaries and the many times difficult distinction between the lungs tissue and other soft tissue, particularly in the tally images.

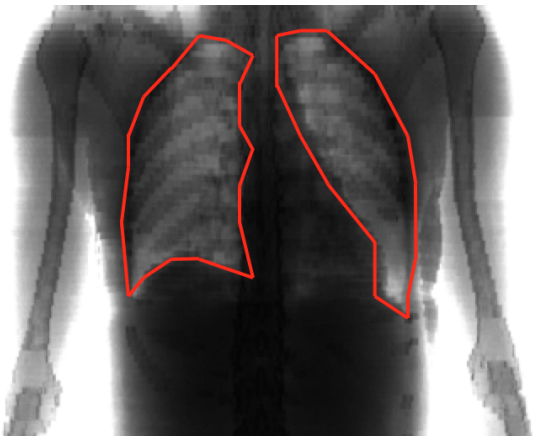

a)

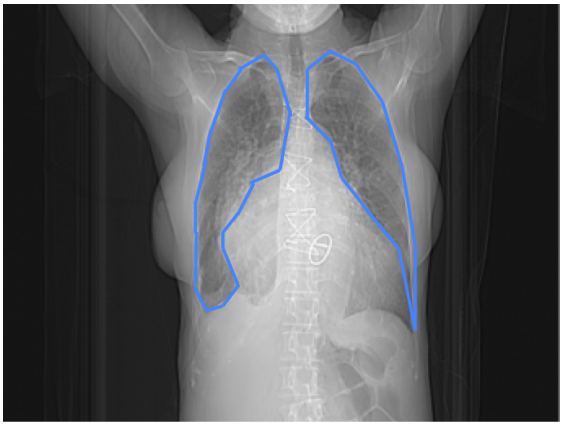

b)

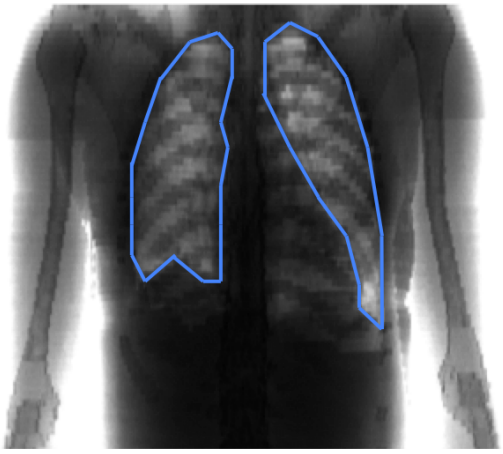

c)

Figure 6.7: **a)** Image of the AF phantom obtained via the tally pixelated imaging detector. Statistical uncertainty: 2%. **b)** CT image topogram for Patient 1. **c)** Image of AF1 obtained via the tally pixelated imaging detector. Statistical uncertainty: 3%. An approximate segmentation was performed using red lines in the AF phantom (before the patient/phantom matching procedure) and using blue lines in the Patient 1 topogram and AF1 image (after the patient/phantom matching procedure). This segmentation meant to emphasize the modification of the size of the lungs by the ReDimLungs program.

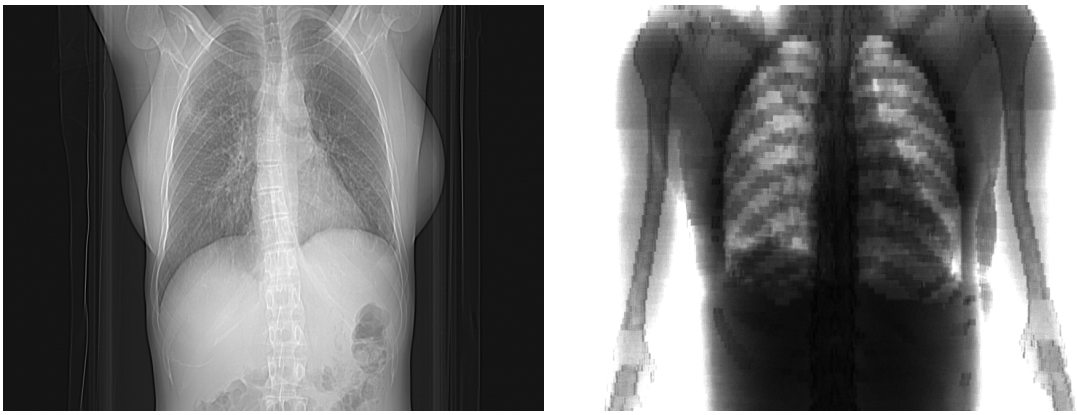

a) b)

Figure 6.8: **a)** CT image topogram for Patient 2. **b)** Image of AF2 obtained via the tally pixelated imaging detector. Statistical uncertainty: 1.9%.

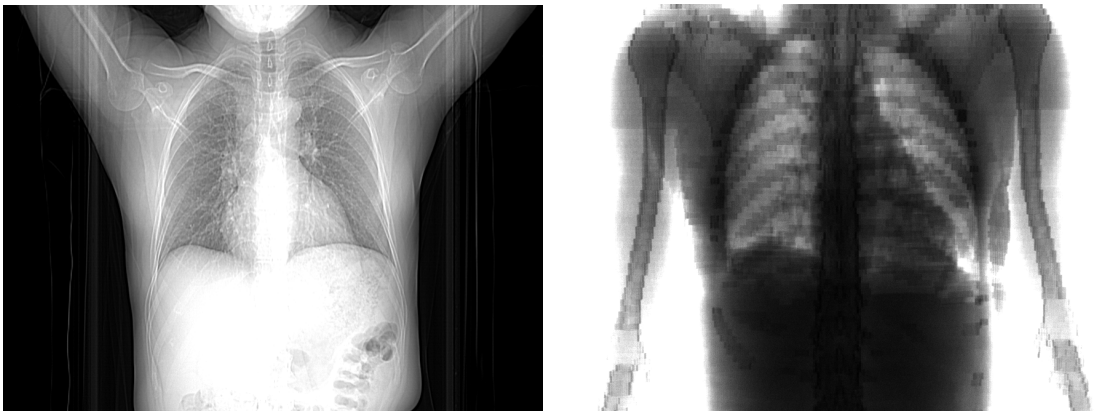

a) b)

Figure 6.9: **a)** CT image topogram for Patient 3. **b)** Image of AF3 obtained via the tally pixelated imaging detector. Statistical uncertainty: 1.9%.

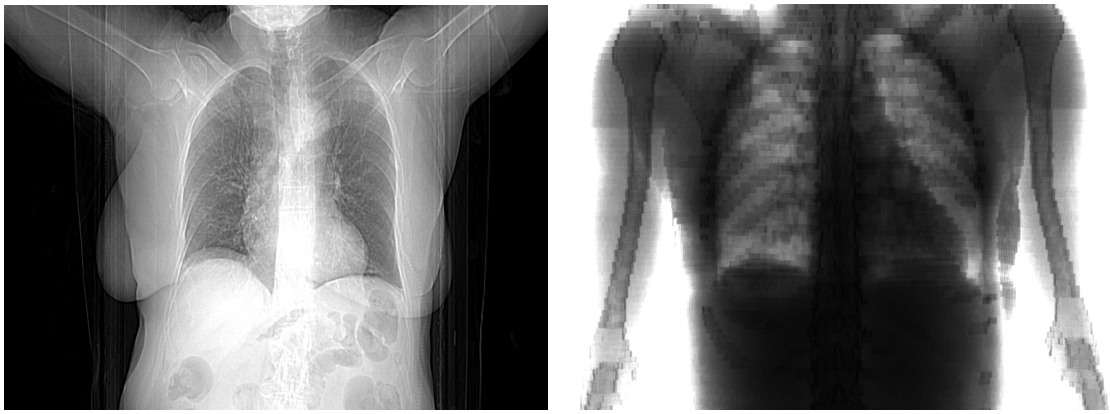

a) b)

Figure 6.10: **a)** CT image topogram for Patient 4. **b)** Image of AF4 obtained via the tally pixelated imaging detector. Statistical uncertainty: 1.9%.

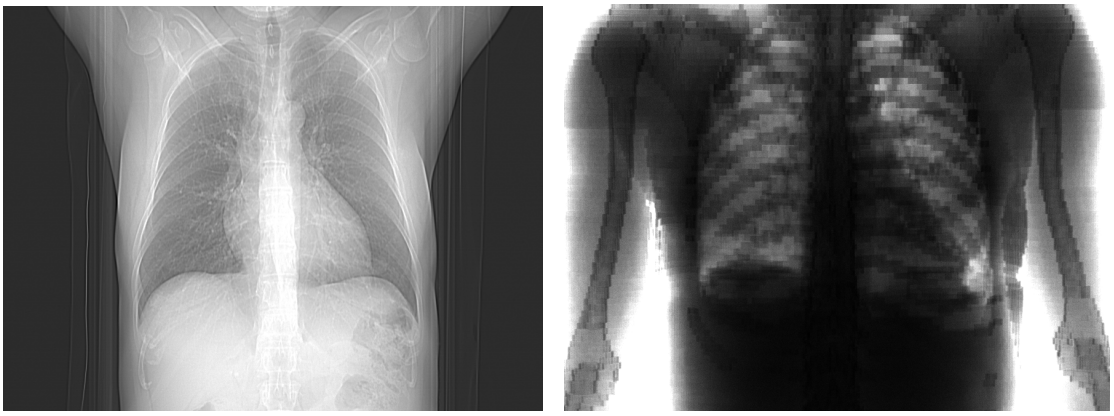

a) b)

Figure 6.11: **a)** CT image topogram for Patient 5. **b)** Image of AF5 obtained via the tally pixelated imaging detector. Statistical uncertainty: 2.6%.

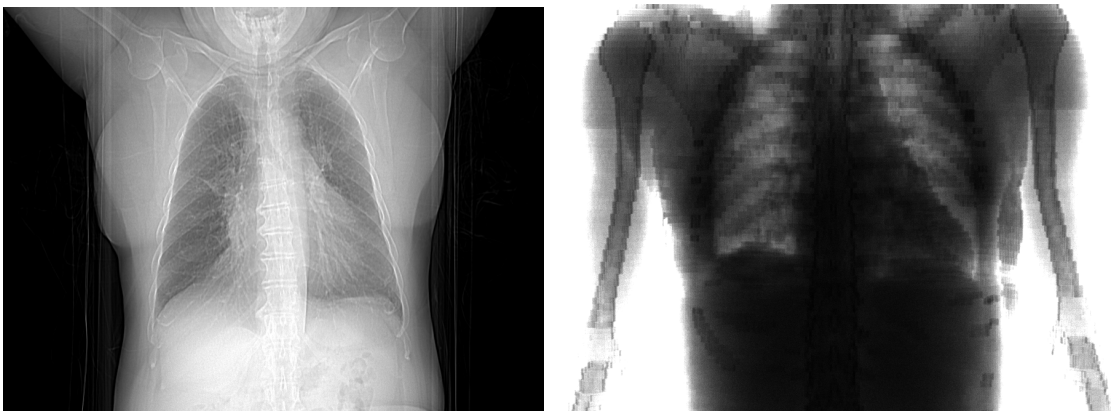

a) b)

Figure 6.12: **a)** CT image topogram for Patient 6. **b)** Image of AF6 obtained via the tally pixelated imaging detector. Statistical uncertainty: 2%.

Chapter 7

Conclusions and Future Work

The present study was carried out in the context of providing more accurate estimates of patient and organ dose for patients undergoing diagnostic radiology examinations. Actually, there are limitations mainly due to the great variation in patient size. The main aim of this study was to modify existing 3D voxel phantom models, by adapting the phantom's overall size and matching the lung's dimensions, trying to progress the concept of a more personalized patient dosimetry.

Firstly, using the PENELOPE code, the implemented MC model of a CT image acquisition system was considered successfully validated with a relative difference of approximately 1.6% between the measured and the simulated $CTDI_W$ values.

For the second part of this work, the female ICRP reference phantom was used for the study of various trends relating organ dose with the phantom's voxel volume. Generally, it was realized that organ dose tends to decrease as voxel volume grows. It was also shown that scaling the phantom in the y direction (direction of the irradiation) had a significant effect on organ dose. The inherent difficulty to working with a phantom that contains over 14 million voxels (which implies working with files containing over 14 million lines), as well as the effort necessary for implementing geometry files in PenEasy, represent a challenging part of this type of work.

The third part of this thesis was dedicated to the development of a FORTRAN-based program that adjusts the organs of a voxel phantom model to the anatomy of a specific patient. The FORTRAN program, named ReDimLungs, was developed with the objective of modifying the phantom's overall size, as well as modifying the lung dimensions of a voxel phantom without significantly altering the general shape of the lungs. Several versions of the program, through trial and error method, were created and tested. This was a challenging process, mainly due to the difficulty in working with organs inside a 3D model constituted by a high number of voxels.

Essentially, the program works by adding and subtracting layers of voxels in the x, y and z directions, in order to preserve the general shape of the lung during its execution. Although the program has been developed specifically for lung scaling, the code can be easily modified so it applies to other organs. Moreover, ReDimLungs was developed to work specifically with the female ICRP reference phantom but the code can be easily adapted to handle other voxel phantoms. However, though ReDimLungs works rather well with larger organs, such as the lungs and the liver, it does not work well with distributed organs, such as skin, bone and red bone marrow, which are also the most difficult organs to delineate using segmentation techniques [49]. It is essential to point out that precise and detailed segmentation of organ contours is a separate and not trivial issue that was not addressed in this thesis, although it can easily be integrated into the proposed concept when it becomes available. Looking at the calculations reported in this thesis, it is safe to state that ReDimLungs led to quite satisfactory results.

Finally, MC simulations were performed both on ICRP reference phantom and on the resolution and patient phantoms. The patient phantoms results mainly lead to the conclusion that matching the voxel phantom's size and lungs provides organ dose values significantly different from the ones measured in the AF phantom. Voxel models matched to patients' anatomy allow increased accuracy in organ dose estimation, which, as reported by this study, can suffer from up to 20% underestimation and 40% overestimation. The approach used in this work to provide a more personalized patient dosimetry can then be considered an interesting tool in order to take into account dose variations between different patients, in relation to the standard AF phantom.

Other concepts of calculating patient and/or organ specific dose estimates such as SSDE and POSDE are still work in progress. Similarly to POSDE, the method used in this thesis combines the advantages of using voxel phantoms, containing detailed organ descriptions, with individual patient CT data, which can provide accurate information on body size and shape in the scanned range. Although in POSDE organ doses can be estimated with high accuracy, the effort required by simulating with the patient's CT data is, according to Kalender et al., demanding and neither indicated nor necessary for routine purposes [49]. An approach derived from the work performed by Kalender et al., using a reference voxel model and modifying just the most important organs in it, was shown also to provide organ dose estimates with high accuracy and be quick enough for routine clinical procedures, which was one of the main concerns during the realization of this study.

Generally, before a CT examination, the acquisition system takes one or two low dose images, the topograms, in order to choose the desired FOV. Though the use of these images, this study managed to create voxel models closer to individual patient anatomy and, consequently, access organ dose values different from the ones obtained using the standard phantom. The procedure developed during this thesis is estimated to take approximately 15 to 20 minutes to modify a reference phantom to an individualized patient phantom, including performing MC simulations to obtain organ doses with low

statistical uncertainty (lower than 5%). Nevertheless, it is worth to mention that the MC images of voxel phantoms take several days in order to reach a satisfactory uncertainty.

The presented concept could be interesting also for radiotherapy planning and dose optimization and personalized dosimetry studies.

We consider the goals accomplished during this work as a step to further provide individual and personalized dosimetry, thus improving the accuracy of dose estimation and, consequently, the execution of computed tomography examinations. Since the radiologic scientific community has expressed concerns about the raising collective dose to the population due to diagnostic radiology, special and continued scrutiny with respect to patient and organ dose is necessary, particularly in pediatric examinations.

The perspectives of possible improvements and future work are mainly focused on the following aspects:

- An extensive validation of the program ReDimLungs regarding a bigger and more heterogeneous sample of patients, along with its update so it is able to handle most voxel phantoms and scale most organs. The process could be extended to the ICRP reference male phantom and other voxel phantoms. Special attention should be given to pediatric phantoms, since children are more sensitive to radiation than adults.

- The addition of an automated lung scaling process, described in section 4.6.3 to the ReDimLungs code (so the process to obtain a personalized phantom was automated), the duration of the process would greatly decrease by a factor of about four, which could represent the right direction towards the application of this method in a routinely way in hospitals.

- The measurement of patient CT images and assessment of lung sizes using imaging segmentation techniques, which could contribute to its automatization. This process would lead to a more accurate measurement of the patients' diameters and organ dimensions.

- The development of a guest user interface for ReDimLungs, so it could be easily used by radiology department professionals, such as radiologists and physicians.

- The development of a FORTRAN routine, which could be coupled with MC code packages, allowing the user to modify the dimensions of a phantom's organs, could be useful for investigation.

References

[1] United Nations Scientific Committee on the Effects of Atomic Radiation, "SOURCES AND EFFECTS OF IONIZING RADIATION – Volume I," UNSCEAR, New York, NY, Report to the General Assembly, 2008.

[2] S. Ma et al., "Biological effects of low-dose radiation from computed tomography scanning," *Int. J. Radiat. Biol.*, vol. 89, no. 5, pp. 326–333. Jan, 2013.

[3] K. Doi, "Computer-aided diagnosis in medical imaging: Historical review, current status and future potential," *Comput. Med. Imaging Graph.*, vol. 31, no. 4–5, pp. 198–211, Jun. 2007.

[4] J. Shiraishi et al., "Computer-Aided Diagnosis and Artificial Intelligence in Clinical Imaging," *Semin. Nucl. Med.*, vol. 41, no. 6, pp. 449–462, Nov. 2011.

[5] S. Katsuragawa and K. Doi, "Computer-aided diagnosis in chest radiography," *Comput. Med. Imaging Graph.*, vol. 31, no. 4–5, pp. 212–223, Jun. 2007.

[6] D. A. Schauer and O. W. Linton, "National Council on Radiation Protection and Measurements Report Shows Substantial Medical Exposure Increase," *Radiology*, vol. 253, no. 2, pp. 293–296, Nov. 2009.

[7] F. A. Mettler et al., "Radiologic and Nuclear Medicine Studies in the United States and Worldwide: Frequency, Radiation Dose, and Comparison with Other Radiation Sources—1950–2007," *Radiology*, vol. 253, no. 2, pp. 520–531, Nov. 2009.

[8] Eurostat, *Healthcare resource statistics - technical resources and medical technology*, 2016. [Online]. Available: http://ec.europa.eu/eurostat/statistics-explained. [Accessed: 22-Jun-2017].

[9] D. J. Brenner and C. D. Elliston, "Estimated Radiation Risks Potentially Associated with Full-Body CT Screening," *Radiology*, vol. 232, no. 3, pp. 735–738, Sep. 2004.

[10] M.O. Bernier et al., "Potential cancer risk associated with CT scans: Review of epidemiological studies and ongoing studies," *Prog. Nucl. Energy*, vol. 84, pp. 116–119, Sep. 2015.

[11] M. S. Pearce et al., "Radiation exposure from CT scans in childhood and subsequent risk of leukaemia and brain tumours: a retrospective cohort study," *The Lancet*, vol. 380, no. 9840, pp. 499–505, Aug. 2012.

[12] J. D. Mathews et al., "Cancer risk in 680 000 people exposed to computed tomography scans in childhood or adolescence: data linkage study of 11 million Australians," *BMJ*, vol. 346, pp. 346-f2360, May 2013.

[13] W.Y. Huang et al., "Paediatric head CT scan and subsequent risk of malignancy and benign brain tumour: a nation-wide population-based cohort study," *Br. J. Cancer*, vol. 110, no. 9, pp. 2354–2360, Apr. 2014.

[14] E. K. J. Pauwels and M. Bourguignon, "Cancer induction caused by radiation due to computed tomography: a critical note," *Acta radiol.*, vol. 52, no. 7, pp. 767–773, Sep. 2011.

[15] G. L. Russo et al., "Cellular adaptive response to chronic radiation exposure in interventional cardiologists," *Eur. Heart J.*, vol. 33, no. 3, pp. 408–414, Feb. 2012.

[16] D. J. Brenner, "Should We be Concerned About the Rapid Increase in CT Usage," *Rev. Environ. Health*, vol. 25, no. 1, Jan. 2010.

[17] A. B. Meer et al., "Exposure to Ionizing Radiation and Estimate of Secondary Cancers in the Era of High-Speed CT Scanning: Projections From the Medicare Population," *J. Am. Coll. Radiol.*, vol. 9, no. 4, pp. 245–250, Apr. 2012.

[18] T. Schweitzer et al., "Avoiding CT scans in children with single-suture craniosynostosis," *Child's Nerv. Syst.*, vol. 28, no. 7, pp. 1077–1082, Jul. 2012.

[19] C. I. Lee et al., "Diagnostic CT Scans: Assessment of Patient, Physician, and Radiologist Awareness of Radiation Dose and Possible Risks," *Radiology*, vol. 231, no. 2, pp. 393–398, May 2004.

[20] W. A. Kalender, "Dose in X-ray Computed Tomography," *Phys. Med. Biol.*, vol. 59, pp. 129–150, 2014.

[21] H. Yoriyaz, "Método de Monte Carlo: princípios e aplicações em Física Médica," *Rev. Bras. Física Médica*, vol. 3, no. 1, pp. 141–149, 2009.

[22] J. M. Boone et al., "Size-Specific Dose Estimates (SSDE) in Pediatric and Adult Body CT Examinations," AAPM, College Park, MD, Rep. No. 204, 2011.

[23] E. Podgorsak, *Radiation Physics for Medical Physicists*, 2nd ed. Berlin, Germany: Springer-Verlag, 2010.

[24] J. E. Turner, *Atoms, Radiation, and Radiation Protection*, 3rd ed. Weinheim, Germany: Wiley-VCH Verlag GmbH & Co. KGaA, 2007.

[25] J. J. P. de Lima, *Técnicas de Diagnóstico com Raios X: Aspectos Físicos e Biofísicos*, 2nd ed. Coimbra, Portugal: Imprensa da Universidade de Coimbra, 2009.

[26] R. Cierniak, *X-Ray Computed Tomography in Biomedical Engineering*. London, England: Springer-Verlag, 2011.

[27] Z. Ahmad et al., "How to interpret computed tomography of the lumbar spine," *Ann. R. Coll. Surg. Engl.*, vol. 96, no. 7, pp. 502–507, Nov. 2014.

[28] D. R. Dance et al., *Diagnostic Radiology Physics*, 1st ed. Vienna, Austria: IAEA, 2014.

[29] L. W. Goldman, "Principles of CT and CT Technology," *J. Nucl. Med. Technol.*, vol. 35, no. 3, pp. 115–128, Sep. 2007.

[30] *IAEA* [Online]. Available: https://www.iaea.org. [Accessed: 27-Jul-2017].

[31] *UNSCEAR* [Online]. Available: http://www.unscear.org [Accessed: 27-Jul-2017].

[32] ICRP, "ICRP Publication 120: Radiological Protection in Cardiology," *Ann. ICRP*, vol.42, no.1, 2013.

[33] S. M. Seltzer et al., "ICRU Report 85: Fundamental Quantities And Units For Ionizing Radiation," *J. ICRU*, vol. 11, no. 1, 2011.

[34] ICRP, "ICRP Publication 103: The 2007 Recommendations of the International Commission on Radiological Protection," *Ann. ICRP*, vol. 37, no. 2-4, 2007.

[35] L. W. Goldman, "Principles of CT and CT Technology," *J. Nucl. Med. Technol.*, vol. 35, no. 3, pp. 115–128, Sep. 2007.

[36] T. B. Shope et al., "A method for describing the doses delivered by transmission x-ray computed tomography," *Med. Phys.*, vol. 8, no. 4, pp. 488–495, Jul. 1981.

[37] J. M. Boone, "The trouble with CTDI100," *Med. Phys.*, vol. 34, no. 4, pp. 1364–1371, Mar. 2007.

[38] K. Perisinakis et al., "Determination of the Weighted CT Dose Index in Modern Multi-Detector CT Scanners.," *Phys. Med. Biol.*, vol. 52, pp. 6485–95, 2007.

[39] R. L. Dixon et al., "AAPM Report No. 111: Comprehensive Methodology for the Evaluation of Radiation Dose in X-Ray Computed Tomography," AAPM, College Park, MD, Rep. No. 111, 2010.

[40] X. G. Xu, "An exponential growth of computational phantom research in radiation protection, imaging, and radiotherapy: a review of the fifty-year history.," *Phys. Med. Biol.*, vol. 59, pp. 233–302, 2014.

[41] J. A. Seibert et al., "Dose Is Not Always What It Seems: Where Very Misleading Values Can Result From Volume CT Dose Index and Dose Length Product," *J. Am. Coll. Radiol.*, vol. 11, no. 3, pp. 233–237, Mar. 2014.

[42] J. Dabin et al., "Validation of calculation algorithms for organ doses in CT by measurements on a 5 year old paediatric phantom," *Phys. Med. Biol.*, vol. 61, no. 11, pp. 4168–4182, Jun. 2016.

[43] K. Z. Morgan et al., "Health Physics Division Annual Progress Report," ORNL, Oak Ridge, TN, ORNL-4168, 1967.

[44] ICRP, "ICRP Publication 23: Report of the Task Group on Reference Man," *Ann. ICRP*, vol. 4, no. 3-4, 1975.

[45] S. J. Gibbs et al., "Radiation Doses to Sensitive Organs from Intraoral Dental Radiography," *Dentomaxillofacial Radiol.*, vol. 16, no. 2, pp. 67–77, Jun. 1987.

[46] ICRP, "ICRP Publication 110: Adult Reference Computational Phantoms," *Ann. ICRP*, vol. 39, no. 2, 2009.

[47] C. Lee et al., "Whole-body voxel phantoms of paediatric patients—UF Series B," *Phys. Med. Biol.*, vol. 51, no. 18, pp. 4649–4661, Sep. 2006.

[48] X. G. Xu et al., "VIP-MAN: An Image-Based Whole-Body Adult Male Model Cconstructed From Color Photographs of the Visible Human Project For Multi-Particle Monte Carlo Calculations," *Health Phys.*, vol. 78, no. 5, pp. 476–486, May 2000.

[49] W. A. Kalender et al., "Generating and using patient-specific whole-body models for organ dose estimates in CT with increased accuracy: Feasibility and validation," *Phys. Medica*, vol. 30, no. 8, pp. 925–933, Dec. 2014.

[50] P. D. Deak et al., "Multisection CT Protocols: Sex- and Age-specific Conversion Factors Used to Determine Effective Dose from Dose-Length Product," *Radiology*, vol. 257, no. 1, pp. 158–166, Oct. 2010.

[51] H. K. Patni et al., "Selected organ dose conversion coefficients for external photons calculated using ICRP adult voxel phantoms and Monte Carlo code FLUKA," *Radiat. Prot. Dosimetry*, vol. 147, no. 3, pp. 406–416, Nov. 2011.

[52] ICRP, "ICRP Publication 116: Conversion Coefficients for Radiological Protection Quantities for External Radiation Exposures," *Ann. ICRP*, vol. 40, no. 2–5, 2010.

[53] R. Veit and M. Zankl, "Influence of Patient Size on Organ Doses in Diagnostic Radiology," *Radiat. Prot. Dosimetry*, vol. 43, no. 1–4, pp. 241–243, Oct. 1992.

[54] M. Caon et al., "Monte Carlo Calculated Effective Dose to Teenage Girls from Computed Tomography Examinations," *Radiat. Prot. Dosimetry*, vol. 90, no. 4, pp. 445–448, Sep. 2000.

[55] M. Caon, "Voxel-based computational models of real human anatomy: A review," *Radiat. Environ. Biophys.*, vol. 42, no. 4, pp. 229–235, Feb. 2004.

[56] W. P. Segars et al., "Patient specific computerized phantoms to estimate dose in pediatric CT," in *Proc. of SPIE - The International Society of Optical Engineering*, 2009, Feb. 2014, p. 72580H.

[57] D. J. Tward et al., "Patient Specific Dosimetry Phantoms Using Multichannel LDDMM of the Whole Body," *Int. J. Biomed. Imaging*, vol. 2011, pp. 1–9, 2011.

[58] D. Broggio et al., "Construction of an extended library of adult male 3D models: rationale and results," *Phys. Med. Biol.*, vol. 56, no. 23, pp. 7659–7692, Dec. 2011.

[59] G. Bueno et al., "Fast Monte Carlo simulation on a voxelized human phantom deformed to a patient," *Med. Phys.*, vol. 36, no. 11, pp. 5162–5174, Oct. 2009.

[60] R. Kramer et al., "All about MAX: a male adult voxel phantom for Monte Carlo calculations in radiation protection dosimetry," *Phys. Med. Biol.*, vol. 48, no. 10, pp. 1239–1262, May 2003.

[61] PTW, "Ionizing Radiation Detectors, Including Codes of Practice," PTW, 2017. [Online]. Available: http://www.ptw.de/online_ brochure.html

[62] A. F. Maia and L. V. E. Caldas, "Performance of a pencil ionization chamber in various radiation beams," *Appl. Radiat. Isot.*, vol. 58, no. 5, pp. 595–601, May 2003.

[63] RaySafe, "RaySafe Xi User Manual." RaySafe, 2015. [Online]. Available: http://www.raysafe.com/Products/Equipment/RaySafe%20Xi

[64] *Gammex* [Online]. Available: http://test.gammex.netphoria.com [Accessed: 31-Aug-2017].

[65] *Medical Expo* [Online]. Available: http://www.medicalexpo.com/prod/sun-nuclear/product-80076-664892.html [Accessed: 31-Aug-2017].

[66] M. Zankl, "Adult Male and Female Reference Computational Phantoms (ICRP Publication 110)," *Japanese J. Heal. Phys.*, vol. 45, no. 4, pp. 357–369, 2010.

[67] J. C. Adams et al., *The Fortran 2003 Handbook*, 1st ed. London, England: Springer-Verlag London, 2009.

[68] J. Sempau et al., "A PENELOPE -based system for the automated Monte Carlo simulation of clinacs and voxelized geometries-application to far-from-axis fields," *Med. Phys.*, vol. 38, no. 11, pp. 5887–5895, Oct. 2011.

[69] *Gnuplot* [Online]. Available: http://www.gnuplot.info [Accessed: 18-Sep-2017].

[70] *ImageJ* [Online]. Available: https://imagej.net/ [Accessed: 18-Sep-2017].

[71] F. Salvat et al., *PENELOPE-2008: A Code System for Monte Carlo Simulation of Electron and Photon Transport A Code System for Monte Carlo*. Barcelona, Spain: OECD/NEA, 2008.

[72] G. Battistoni et al., "The FLUKA code: description and benchmarking," in *AIP Conf. Proc.*, vol. 896, Mar. 2007, pp. 31–49.

[73] J. Allison et al., "Geant4 Developments and Applications," *IEEE Trans. Nucl. Sci.*, vol. 53, no. 1, pp. 270–278, 2006.

[74] J. F. Briesmeister, "MCNP – A General Monte Carlo N-Particle Transport Code -Version 4C," LANL, Los Alamos, NM, Report LA-13709-M, Mar. 2000.

[75] I. Kawrakow et al., "The EGSnrc Code System: Monte Carlo Simulation of Electron and Photon Transport," NRC Canada, Ottawa, Canada, Report PIRS-701, Jun. 2017.

[76] *Origin* [Online]. Available: http://www.originlab.com [Accessed: 18-Sep-2017].

[77] K. Cranley et al., "IPEM Report no. 78: Catalogue of Diagnostic X-ray Spectra and Other Data," IPEM, York, England, Report No. 78, Sep. 1997.

[78] C. Figueira et al., "Medical staff extremity dosimetry in CT fluoroscopy: an anthropomorphic hand voxel phantom study," *Phys. Med. Biol.*, vol. 58, no. 16, pp. 5433–5448, Aug. 2013.

[79] J. Simões, "Simulações Monte Carlo da radução da dose no cristalino e na tiróide em exames de Tomografia Computorizada utilizando protecções de bismuto," M.S. Thesis, DF, FCT-UNL, Almada, Portugal, Dec. 2013.

[80] C. Tomasetti et al., "Stem cell divisions, somatic mutations, cancer etiology, and cancer prevention," *Science*, vol. 355, no. 6331, pp. 1330–1334, Mar. 2017.

Appendix

Lists of Materials and Organs Used in Voxel Phantom Simulations

Appendix A lists the materials and organs considered when performing MC simulations on AF.

Table A.1: List of the organs present in the organ list of the AF phantom. The table was simplified, so it shows the materials that were modified or added to the original present in ICRP Publication nº 110. Adapted from [46].

Organ ID	Organ Name	Material ID
0	Air outside body	53
96	Lung, Left, Blood	58
97	Lung, Left, Tissue	50
98	Lung, Right, Blood	59
99	Lung, Right, Tissue	54
140	Air inside body	53
141	Air at top/bottom slices	53

Table A.2: List of the materials defined in the PENELOPE section of the PenEasy input file. The table was simplified, so it shows the materials that were modified or added to the original present in ICRP Publication nº 110. Adapted from [46].

Material ID	**Material Name**	**Density** ($g\,cm^{-3}$)
50	Lung, Tissue, Left	0.385
53	Air inside phantom box	0.001
54	Lung, Tissue, Right	0.385
55	Air from outer sphere	0.001
56	Air transparent	0.001
57	Selenium (detector)	4.500
58	Lung, Blood, Left	1.060
59	Lung, Blood, Right	1.060

Appendix B

Tally and 36-Point Interpolation Results from MC Model Validation

Appendix B contains the MC tally results for the IC in-air and at the center, 0º and 90º positions, as well as the total IC deposited energy, corresponding the sum of the deposited energies from all source positions after 36-point interpolation. An example of an interpolation graph (Figure B.1) is also present.

Table B.1: Tally and interpolation results for the IC in-air position.

Orifice	**Source Position** (º)	**Tally Value** (eV hist^{-1})	**Uncertainty** (%)
in-air	0	2.7116×10^{-2}	0.7
	90	2.7133×10^{-2}	0.7
	180	2.7119×10^{-2}	0.7
	270	2.7116×10^{-2}	0.7
	360	2.7116×10^{-2}	0.7
Average Unvertainty (%)			0.7
Sum of Tally Values for one rotation (eV hist^{-1})			0.9763

Table B.2: Tally and interpolation results for the IC at center position.

Orifice	**Source Position** (°)	**Tally Value** (eV hist^{-1})	**Uncertainty** (%)
center	0	3.7643×10^{-3}	3.5
	90	3.5426×10^{-3}	3.4
	180	3.6561×10^{-3}	3.3
	270	3.5574×10^{-3}	3.4
	360	3.7643×10^{-3}	3.5
Average Unvertainty (%)			3.4
Sum of Tally Values after Interpolation (eV hist^{-1})			0.1308

Table B.3: Tally and interpolation results for the IC at 0° position.

Orifice	**Source Position** (°)	**Tally Value** (eV hist^{-1})	**Uncertainty** (%)
0°	0	3.0610×10^{-2}	1.3
	90	1.0735×10^{-2}	1.9
	180	2.4107×10^{-4}	13.7
	270	1.0747×10^{-2}	1.9
	360	3.0610×10^{-2}	1.2
Average Unvertainty (%)			4.0
Sum of Tally Values after Interpolation (eV hist^{-1})			0.4890

Table B.4: Tally and interpolation results for the IC at 90° position.

Orifice	**Source Position** (°)	**Tally Value** (eV hist^{-1})	**Uncertainty** (%)
90°	0	1.0742×10^{-2}	1.9
	90	3.0592×10^{-2}	1.2
	180	1.0917×10^{-2}	1.9
	270	1.9470×10^{-4}	13.9
	360	1.0742×10^{-2}	1.9
Average Unvertainty (%)			4.2
Sum of Tally Values after Interpolation (eV hist^{-1})			0.4696

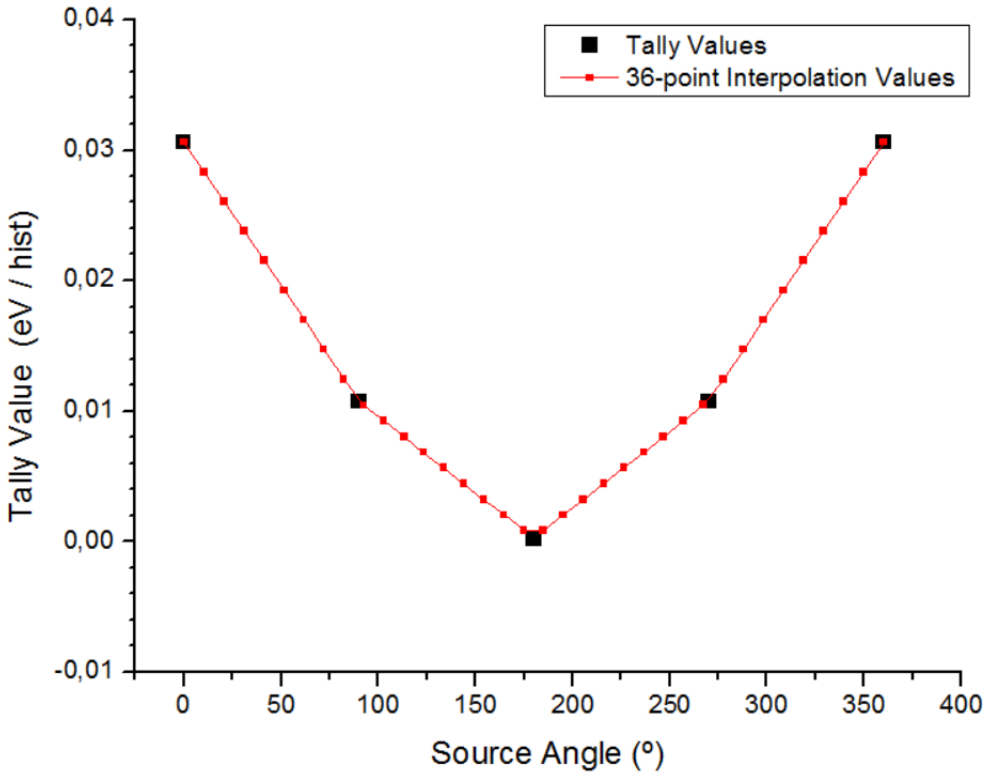

Figure B.1: Example of graph of 36-interpolation of the tally values, for the IC at 0º position, performed using the statistical analysis software Origin.

Appendix

Lung Size Values Before and After Patient/Phantom Matching Procedure

Appendix C contains tables C.1 and C.2, representing the lung size in x, y and z before and after the patient/phantom matching procedure for the left and right lung, respectively.

Table C.1: Left lung size in x, y and z measured in the patients' CT images and in the patient phantoms (after application of the patient/phantom matching procedure), as well as the relative difference between them. The average values were calculated using patient 1 through 6 values, not accounting for AF values.

Patient #	**CT Image Lung Size** (cm)			**Patient Phantoms Lung Size** (cm)			**Lung Size Relative Difference** (%)		
	x	y	z	x	y	z	x	y	z
AF	11.0050	13.8450	21.7800	-	-	-	-	-	-
1	9.490	16.175	23.019	9.9201	15.7638	22.7480	4.53	2.54	1.18
2	9.072	18.144	20.563	9.4304	17.7842	20.8120	3.95	1.98	1.21
3	11.102	16.533	19.090	10.8840	16.1365	19.3600	1.96	2.40	1.41
4	10.922	16.294	21.491	11.3760	15.8390	21.7800	4.16	2.79	1.34
5	12.474	20.591	24.655	12.5302	20.2740	24.2000	0.45	1.54	1.85
6	10.386	17.960	22.145	10.6164	18.2175	21.7800	2.22	1.43	1.65
Average	10.574	17.616	21.827	10.792	17.336	21.780	2.88	2.11	1.44

Table C.2: Right lung size in x, y and z measured in the patients' CT images and the patient phantoms (after application of the patient/phantom matching procedure), as well as the relative difference between them. The average values were calculated using patient 1 through 6 values, not accounting for AF values.

Patient #	**CT Image Lung Size** (cm)			**Patient Phantoms Lung Size** (cm)			**Lung Size Relative Difference** (%)		
	x	y	z	x	y	z	x	y	z
AF	20.0575	14.2000	20.3280	-	-	-	-	-	-
1	9.191	16.175	21.163	9.6000	15.7638	20.8120	4.45	2.54	1.66
2	10.445	18.502	20.291	10.9460	18.1632	20.3280	4.80	1.83	0.18
3	11.280	16.772	20.018	11.6096	16.3285	20.3280	2.92	2.64	1.55
4	11.758	16.831	23.619	12.1344	16.4410	23.2320	3.20	2.32	1.64
5	13.011	19.995	24.164	13.3386	19.6200	23.7160	2.52	1.88	1.85
6	11.031	18.204	21.709	11.2062	18.2175	20.3280	1.59	0.07	6.36
Average	11.119	17.747	21.8275	11.472	17.4223	21.4573	3.25	1.88	2.21

ANNEX I

Tutorial for the ReadPhantom Program

In Annex I a tutorial for the ReadPhantom program is presented. This tutorial, developed during this thesis, explains how to work with the program and describes the simulation and visualization files it creates.

Jorge Cebola Borbinha

Read Phantom Tutorial

ReadPhantom is a FORTRAN program developed to create the files necessary for simulation and visualisation of voxel phantoms. The use of this program will require two files to work properly and create six.

The terminal commands presented in this file are presented for Ubuntu Linux. If you have a different operating system, the commands may differ. The command *$ wc filename.txt* responds with three numbers: number of lines, number of words and number of characters of a file.

Contents:

1. Files Required
2. Files Created
3. Working with the Program
4. Script Limitations

(1) Files Required

In order to run this program, there are two files that need to be in the same folder in which the program is run. These two files are the phantom file (which usually comes in the *.dat format) and the organlist.dat file.

The phantom file may in be in either binary or ASCII format. There may or may not be a header present, that needs to be removed for the script to work properly.

The user should create the organlist.dat file by listing every organ, material and density that the phantom possesses, in the following order: Organ ID, Material ID and density, separated by spaces. A brief example of this file is described in the next image. The air outside body's Organ ID is usually 0 (first line of the file), and should be defined as the air that suits you most. Although it's important, the organ lists that come with the phantom files usually don't list this Organ ID. If, by chance, your density values all come with negative values for application in the MCNP code, don't worry. At a convenient time, the script will alert you to this issue and offer to change all of the densities to their absolute value.

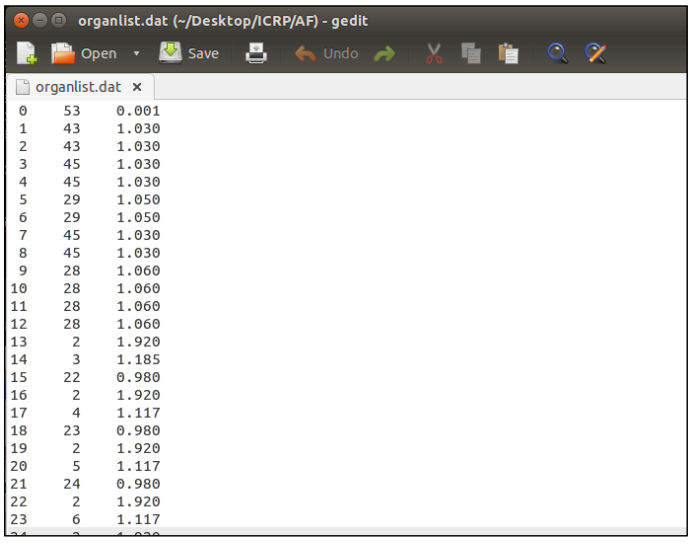

(2) Working with the Program

In order to run the program the readPhantom.f95 file needs to be compiled and executed by typing the following commands.

$ gfortran -Wall -Os readPhantom.f95 -o readPhantom.exe

$ ./readPhantom.exe

Then you only need to follow the questions and/or instructions in the terminal. An example, using the ICRP female reference phantom follows:

```
jorgeborbinha@ubuntu:~/Desktop/ICRP/AF$ ./readPhantom.exe
  Please insert the name of the phantom file (max 20 characters).
AF.dat
  Is your file in binary or in ASCCI? (type 0 for bin or 1 for ASCII)
1
  Type in the number of voxels of the phantom in x,y,z.
299 137 348
  Type in the voxel resolution in x,y,z /cm.
0.1775 0.1775 0.484
  Type in the number of different materials in the phantom.
53
  Type in the number of organ IDs - number of lines in organlist.dat.
142

 >>> Characteristics of your phantom file:
 > Number of voxels in x,y,z:  299  137  348
 > Voxel resolution in x,y,z /cm:  0.1775000   0.1775000   0.4840000
 > Phantom size (approximate value) in x,y,z /cm:    53.0724983    24.3174992   168.4319916
 > Total number of voxels:  14255124

  Please check if these values are correct. Do you wish to continue? (y/n)
  Please type y or n.
```

First, you should know if your phantom file is in binary or ASCII. Then you should type in the number of voxels and voxel resolution in x, y and z directions – pay attention to the units. After that type in the number of different materials in the phantom, which may or may not be the maximum Material ID number. Lastly, you should inform the program on the number of organs that your phantom is made of, which is the same as the number of lines in the organlist.dat file.

Then the program will give the values inserted back to you, plus some other values calculated. Verify if these values are correct. If yes, type 'y'. If not, something went wrong. The program will stop.

After this section the program will start running, giving you some information too keep you updated about several phantom's characteristics and the running progress.

(3) Files Created

This program will create 6 files: phantom.ct, phantom.vox, organlistAsRead.dat, ct-den-matXY.dat, ct-den-matXZ.dat and ct-den-matYZ.dat. To avoid the mixing of several files, it is advised to rename the files phantom.ct and phantom.vox to a name that indicates the phantom they represent. For example, given the case of the ICRP adult female reference phantom, the files can be named regina.ct and regina.vox.

The *.ct file: The *.ct file is an intermediate file that has a two line header:

	(example for ICRP adult female reference)
53.0725 24.3175 163	(phantom size in x,y,z /cm)
299 137 348	(number of voxels in x,y,z)

The regina.ct file should have 14 255 126 lines. This number corresponds the number of voxels in the phantom – 14 255 124 – plus the number of lines of header – 2.

The *.vox file: For simulation, a *.vox file is required. This file has a 7 line header:

[SECTION VOXELS HEADER V.2008-04-13]	(example for ICRP adult female reference)
299 137 348	(number of voxels in x,y,z)
0.1775 0.1775 0.484	(voxel resolution in x,y,z /cm)
1	(1st column for material)
2	(2nd column for density)
0	(no blank line after xy cycle)
[END OF VXH SECTION]	

It's possible to check if the file was correctly created by checking its number of lines. The regina.ct file should have 14 255 131 lines. This number matches the number of voxels in the phantom - 14 255 124 - plus the number of lines of header – 7.

The organlistAsRead.dat file: This is a verification file whose contents correspond those of organlist.dat file, as read by the program.

The ct-den-matXY/XZ/YZ.dat files: These are visualization files, which allow visualization of the phantom in the x, y and z planes. The ct-den-mat.dat files list, for each voxel, the x, y and z indices (column 1, 2 and 3), the density (column 4) and material (column 5). Using gnuplot, a command-line driven graphic utility, scripts, it's possible to visualize the phantom slice per slice. The corresponding gnuplot files are: visualizeVoxelsDensityXY/XZ/YZ.gpl. To visualize the phantom you will need to open gnuplot (just write *gnuplot* in the command line) and write the following command in the terminal:

>load "visualizeVoxelsDensityXY.gpl", or the name of the file corresponding the plane you wish to see.

(4) Script Limitations

This program has some limits that need to be respected in order to guarantee correct execution:

- The total number of voxels in the phantom can´t be bigger than 999 999 999;
- The number of voxels in any axis can't surpass 9 999;
- The number of materials in the phantom can't be bigger than 9 999;
- The maximum Material ID is 9 999;
- The maximum Organ ID is 9 999.